

# Correction Methods for Non-Stationary Noise Floor in Sentinel-1 Images Using Convex Optimization

by

Peter Qiu Jiun Lee

A thesis  
presented to the University of Waterloo  
in fulfillment of the  
thesis requirement for the degree of  
Master of Applied Science  
in  
Systems Design Engineering

Waterloo, Ontario, Canada, 2020

© Peter Qiu Jiun Lee 2020

### **Author's declaration**

I hereby declare that I am the sole author of this thesis. This is a true copy of the thesis, including any required final revisions, as accepted by my examiners.

I understand that my thesis may be made electronically available to the public.



## Abstract

Synthetic aperture radar (SAR) is a method of creating images of the surface of the Earth by emitting and receiving radar waves. Sentinel-1 is a SAR platform made by the European Space Agency (ESA) that provides a source of SAR images open to the public through the operation of two satellites. Due to the non-uniform radiation pattern projected from the satellite's antenna, there are significant non-stationary noise floor intensity patterns that distract from the desired measurements, which are particularly significant in certain types of image modes, namely Extra Wide and Interferometric Wide modes. While ESA provides a default noise floor estimate with each Sentinel-1 product, with the intention that it be subtracted from the original image so the result is homogeneous, there is clear evidence that it is miscalibrated. This Masters thesis presents two novel methods for estimating the noise floor patterns in the images that are demonstrated to be improvements over the default noise floor. The first method presents a way to dynamically construct and apply linear rescaling to the default noise floor estimate over different sections of the images, called subswaths, by use of least squares optimization. While the method is successful in improving image quality, it is not totally effective because the default noise floor is mis-fit in a non-linear manner. The second method constructs a new noise floor as a power function of the radiation pattern power by using linear programming and least squares optimization. This successfully compensates for the non-linear mis-fit, resulting in an overall increase in image quality, albeit with greater parametric complexity. These methods greatly improve the intrinsic value of Sentinel-1 images in scenarios where the noise floor dominates, such as in cross-polarized images and images where the physical materials result in lower backscatter intensity.

## Acknowledgements

I appreciate the supervision and advice from my supervisors David Clausi and Linlin Xu who have been valuable sources of aid during my Masters studies. I credit their encouragement to branch into different avenues of research, which ensured my studies were entertaining.

I would like to thank the members of the VIP lab, and especially the remote sensing group, including Mingzhe 'Major' Jiang, Mohsen Ghanbari, Yuan Fang, Saeid Taleghanidoozan, Keerthijan Radhakrishnan, Daniel Sola, Yifan Wu, and Anmol Nagi. They provided a platform to bounce ideas off of, even if those ideas did not manifest themselves in this thesis.

During my Masters degree I have been involved in several research projects. Even if they did not find their way into this thesis, I would be remissed to not mention my appreciation of discussions with Paul Fieguth, Andrea Scott, Monica Maly, Bryan Tripp, and André Carrington. Thanks are also extended to the readers of this thesis Andrea Scott and Wesley Van Wychen.

Finally, I would like to acknowledge the European Space Agency for not only making their synthetic aperture radar data available to the public, but also providing detailed parameter information in each of their products. Without this information, my research would not have been possible.

# Table of Contents

List of Figures	vii
List of Tables	ix
<b>1 Introduction</b>	<b>1</b>
1.1 Synthetic aperture radar and antenna theory . . . . .	2
1.2 Convex optimization . . . . .	4
1.3 Overview of work . . . . .	6
<b>2 Sentinel-1 Additive Noise Removal from Cross-Polarization Extra-Wide TOPSAR with Dynamic Least-Squares</b>	<b>8</b>
2.1 Introduction . . . . .	10
2.2 SAR noise background . . . . .	12
2.3 Methods . . . . .	17
2.3.1 Objective: Azimuth . . . . .	20
2.3.2 Objective: Range . . . . .	21
2.3.3 Regularization . . . . .	24
2.3.4 Implementation . . . . .	24
2.4 Experiments . . . . .	25
2.4.1 Parameter re-estimation simulation on RADARSAT . . . . .	25
2.4.2 Denoising Sentinel-1 SAR . . . . .	28
2.5 Discussion . . . . .	35
2.6 Conclusion . . . . .	39

<b>3</b>	<b>Estimating Noise Floor in Sentinel-1 Images with Linear Programming and Least Squares</b>	<b>41</b>
3.1	Introduction . . . . .	43
3.2	Background . . . . .	44
3.3	Methods . . . . .	48
3.3.1	Power function . . . . .	50
3.3.2	Subswath offsets . . . . .	56
3.4	Experiments . . . . .	57
3.4.1	RADARSAT-2: Simulation . . . . .	58
3.4.2	Sentinel-1: Appearance . . . . .	61
3.4.3	Sentinel-1: Intensity bias . . . . .	65
3.5	Discussion . . . . .	67
3.6	Conclusion . . . . .	71
<b>4</b>	<b>Conclusion</b>	<b>75</b>
4.1	Future work . . . . .	76
4.2	Final remarks . . . . .	77
	<b>References</b>	<b>83</b>
	<b>Glossary</b>	<b>84</b>

# List of Figures

2.1	Noise in range and azimuth . . . . .	14
2.2	Construction of noise field . . . . .	15
2.3	Undercompensated noise . . . . .	16
2.4	Evidence that the ideal linear scalar differs for each image . . . . .	17
2.5	Objective function . . . . .	19
2.6	Peaks and troughs of the estimated noise with respect to azimuth and range. . . . .	21
2.7	Open-water region . . . . .	23
2.8	Simulation experiment: visualization . . . . .	27
2.9	Regression in quantative experiment . . . . .	30
2.10	Gallery 1 . . . . .	32
2.11	Gallery 2 . . . . .	33
2.12	Static vs dynamic scaling . . . . .	34
2.13	Brief comparison with IPF version 3+ . . . . .	35
2.14	Non-linear misfit evidence . . . . .	38
3.1	Antenna pattern noise floor relation . . . . .	46
3.2	Non-linear mis-fit . . . . .	47
3.3	Division of images . . . . .	49
3.4	Range splits in presumed noise floor . . . . .	52
3.5	Example of parameter estimation . . . . .	55
3.6	Log-log to real domain transformation . . . . .	56

3.7	Simulation EW	60
3.8	Simulation IW	60
3.9	IW simulation with mis-estimation	60
3.10	Sentinel-1 EW gallery 1	62
3.11	Sentinel-1 EW gallery 2	63
3.12	Sentinel-1 IW gallery	64
3.13	Example of profiles along the range	66
3.14	Mis-calibration example of ESA	69
3.15	Parameter estimation for Sentinel-1	70
3.16	Parameter estimation for simulation	71
3.17	Signal dependent intensity bleeding	72

# List of Tables

2.1	Simulation results . . . . .	28
2.2	Sentinel-1 results . . . . .	31
3.1	Simulation quality . . . . .	59
3.2	Sentinel-1 quality . . . . .	65
3.3	Intensity bias change . . . . .	67

# Chapter 1

## Introduction

Synthetic aperture radar (SAR) is a remote sensing method that can be applied to generate images that represent the backscatter of radar waves from a remote surface. Along with the properties of the radar waves emitted by the platform, such as the angle of incidence, polarity, the wavelength, and the intensity, the manner in which radar waves scatter upon hitting a target is determined by the physical properties of the target [36]. Consequently, SAR images provide a way for geoscience and remote sensing practitioners to infer the characteristics of different surface targets. Relevant applications include studying ocean and ice properties [19, 29], oil-spill detection [34], mapping land features [20], and many others [36, 49].

Sentinel-1 is a SAR mission, created by the European Space Agency, that consists of two satellites in sun-synchronous orbit, called Sentinel-1A (launched 2014) and Sentinel-1B (launched 2016) whose orbits are offset by half a period, that produce SAR images of the surface of Earth. Sentinel-1 produces different types of SAR images that are designed for different applications based on two operational parameters called the *product type* and *sensor mode*, which determine the types of data recorded and the surface area and resolution of the images respectively. As will further be clarified below, the material in this thesis specifically targets the Ground Range Detected (GRD) *product type* and extra wide (EW) and interferometric wide (IW) *sensor modes*.

An issue that is particularly apparent from combining product types GRD and EW or IW sensor modes is the presence of noisy intensity patterns in the cross-polarized images. As will be described in further detail throughout this introduction, these patterns are caused by the varying noise floor within the images. The impact of these patterns is overt; the non-stationary noise floor distracts from the underlying backscatter measurements produced by the ground targets and causes difficulties in making consistent comparisons



throughout the images. This is especially detrimental to tasks like ice [22, 50] or wind speed [11, 35] analysis that rely on low backscatter cross-polarized images over maritime regions. **Therefore, this body of work is focused towards improving the quality of SAR images produced by the Sentinel-1 platform by developing methods to estimate and remove the noise floor in cross-polarized images.** To pursue this goal, two major works are presented that utilize convex optimization approaches in order to produce better enhanced noise floors for individual images.

This thesis is laid out as follows. Within the remainder of this introduction, Section 1.1 provides additional background information on SAR and concepts from antenna theory to give additional insight behind the noise floor in the images. In addition, Section 1.2 provides background on concepts of convex optimization that are used in the body of this thesis. Section 1.3 provides an overview and comparison of the two works that compose the main body of the thesis. Moving into the main body, Chapter 2 presents the first work that improves the quality of the noise floor estimations that come with Sentinel-1 products in EW mode by use of a linear model. The second work presented in Chapter 3 describes an approach that models the noise floor to be an affine power function of the antenna radiation pattern power to compensate for the non-linear errors that are unresolved from the first work. Finally, Chapter 4 summarizes the results of the works, avenues of future work, and closing remarks.

## 1.1 Synthetic aperture radar and antenna theory

Synthetic aperture radar (SAR) is an active remote sensing method that emits radar waves to irradiate targets on the surface of the Earth and subsequently measure the resulting backscattered radar waves. SAR utilizes antennas on a moving platform, typically either an airplane or a satellite, to emit and receive the radar measurements, after which a processor algorithm converts the measurements into a spatially mapped image. SAR is differentiated from conventional radar because it uses the Doppler effect to dynamically modify the effective size of its antenna by taking successive measurements over its flight path or orbit [36]. As the measured resolution is inversely proportional to the size of the antenna, this enables finer resolution to be possible without having to carry a large antenna [36].

The Sentinel-1 satellites, which operate in the C-band portion of the spectrum with a frequency of 5.405 GHz, specifically use an antenna array [3], which is a configuration that is made of many individual elements. These elements are individual antennas that are physically spaced apart whose aggregate signals are combined within the array. The array

configuration is useful because the electrical current through each antenna element can be individually controlled and allows the shape of the radiation pattern to be dynamically controlled [23, 52]. These capabilities allows Sentinel-1 to steer the antenna pattern to focus on different look angles during observation.

Next, several items of SAR terminology will be defined. In terms of direction, the range refers to the surface direction that is perpendicular to the satellite’s orbit and azimuth refers to the direction parallel to the satellite’s orbit. Elevation angle refers to the angle between the target and the satellite and the point directly below the satellite. Azimuth angle refers to the azimuth component of the angle between the target and the satellite. SAR platforms have to make considerations regarding the polarity of radiation. Sentinel-1 is designed to operate in dual-pol mode, where the satellite can emit or receive combinations of horizontally or vertically polarized radiation. Sentinel-1 can then produce either/both co-polarized images, called HH or VV, or cross-polarized images, called HV or VH. Co-polarized images result in much higher recorded intensity than cross-polarized images because generally most of the backscatter radiation will retain its original polarity [36]. As a result, the noise floor patterns that are the focus of this paper are much more prominent in cross-polarized images due to the lower backscatter intensity and lower signal to noise ratio.

Sentinel-1 has a total of four different *sensor modes* that are called stripmap (SM), interferometric wide (IW), extra wide (EW), and wave (WV). The two relevant modes to this thesis are IW mode, with three subswaths that altogether cover a range of 250 km with an average resolution of 5 m by 20 m [2], and EW mode, with five subswaths that altogether cover a range of 410 km with an average resolution of 20 m by 40 m [1]. Depending on application, the desired imaging mode determines a trade-off between resolution, and surface area. Sentinel-1 also has a selection of *product types*, that are called single look complex (SLC), ground range detected (GRD), and ocean (OCN) that determine the types of values that are returned in the image. The types of images this thesis focuses on are GRD product types, which discards phase information and only returns intensity information, and the sensor modes that are acquired with the Terrain Observation By Progressive Scans (TOPSAR) method [59], which are EW and IW modes. TOPSAR is a SAR acquisition method that breaks the image into different sections along the range called subswaths, which are acquired by steering the antenna array to different range angles. During orbit, TOPSAR concurrently switches focus between each subswath, while sweeping a radar burst along a section of the azimuth, by steering along the azimuth angle. After processing, the raw signals for each burst are transformed to intensity values over the surface area by the processing pipeline. The bursts are then concatenated within each subswath along the

azimuth, which are then concatenated together to form the entirety of the image [45, 59].<sup>1</sup>

The main issue this thesis aims to resolve are the noisy intensity patterns that occur in the Sentinel-1 images. The underlying cause of the patterns is the manner in which the radiation pattern varies with respect to the azimuth and elevation angles. By definition, the strength of a signal received by an antenna will scale based on the overall strength of the antenna pattern [52]. The noise floor is defined as the sum of noise sources present within a system that serves as a lower-bound of its measured signals [24]. In the SAR system, the origin of the noise floor arises from the thermal noise that is present within the circuitry [48]. Even if the total power of the noise floor did not change as a result of the changing radiation pattern, the ratio between the noise floor and the signal received by backscatter certainly will, since the strength of the measured backscattered signal will vary based on the radiation pattern [52]. Consequently, when the intensity measurements are normalized by the pipeline [3], regions that have lower antenna power will have its signal boosted more in order for the backscatter intensity measurements to be comparable throughout the image. A consequence of this is that the noise floor becomes amplified in a manner that is negatively related to the antenna pattern power, which is how the aforementioned noisy intensity patterns are imposed on the images. Therefore, if one wants to correct the SAR image to only represent backscatter information, this noise floor must be subtracted.

## 1.2 Convex optimization

Convex optimization is a field of optimization that pertains to choosing variables in order to either minimize or maximize convex objective functions. A convex function is any function where a local minimum or local maximum is also the global minimum or global maximum [9]. Convex functions are convenient to optimize because it is clear when the optimal solution has been reached and there are many available algorithms available for solving them with theoretical guarantees included.

The two works in this thesis incorporate two types of convex optimization problems. The first type of problem is the least squares problem. The least squares problem attempts to find parameters to a linear function,  $\sum_j^M c_{i,j}x_j$ , that estimates a series of reference values,  $m_i$ , through minimizing the sum of squared differences between the estimates and

---

<sup>1</sup>The author of this thesis has created two animations to help visualize the scanning process. 1. <https://youtu.be/10r1Ek6gJko> provides a 3D approximation of the scanning process over the ground. 2. <https://youtu.be/56iqka1wAQo> shows how the different sections of the image are generated over time.

the reference values. Generally, this is modelled as

$$\min_{x_1, x_2, \dots, x_M} \sum_i^N \left[ \left( \sum_j^M c_{i,j} x_j \right) - m_i \right]^2, \quad (1.1)$$

where  $x_1, x_2 \dots x_M$  are the optimization variables,  $c_{1,1}, \dots, c_{N,M}$  are the multiplicative coefficients to the linear function, and  $m_1, m_2, \dots, m_N$  are the reference values. The solution to this lies in solving a system of equations where each of the partial derivatives of the objective function with respect to the variables is equal to zero. Ultimately, this reduces to solving a system of linear equations [9]. For convenience, the problem (1.1) can be reformulated in matrix notation

$$\min_{\mathbf{x}} (C\mathbf{x} - \mathbf{m})^\top (C\mathbf{x} - \mathbf{m}), \quad (1.2)$$

where  $\mathbf{x} \in \mathbb{R}^M$  is the vector of optimization variables,  $C \in \mathbb{R}^{N \times M}$  is the matrix of multiplicative coefficients, and  $\mathbf{m} \in \mathbb{R}^N$  is the vector of reference values. The solution to (1.2) can then be aptly written as

$$\mathbf{x} = (C^\top C)^{-1} C^\top \mathbf{m}. \quad (1.3)$$

An important note for this is that the matrix  $C^\top C$  must be full rank else the problem is ill-posed. As a result, many of the least squared problems in this thesis will contain regularization terms that are designed to ensure that the matrix is full-rank.

The second type of optimization problem this thesis utilizes is linear programming. Linear programming is a form of constrained convex optimization that aims to choose variables that maximizes or minimizes a linear function subject to a set of linear constraints. Generally this takes the form of

$$\begin{aligned} \max_{\mathbf{x}} \mathbf{c}^\top \mathbf{x} \\ \text{such that } A\mathbf{x} \leq \mathbf{m}, \end{aligned} \quad (1.4)$$

where  $\mathbf{x} \in \mathbb{R}^M$  is the vector of optimization variables,  $\mathbf{c} \in \mathbb{R}^M$  is the cost vector, and matrix  $A \in \mathbb{R}^{N \times M}$  and vector  $m \in \mathbb{R}^N$  encapsulate the set of  $N$  linear constraints. A linear program can result in one of three outcomes: infeasible, unbounded, or feasible [9]. Infeasible linear programs occurs when the linear constraints interact in such a way that there exists no choice of  $\mathbf{x}$  that satisfies all of them. Unbounded linear programs occur when  $\mathbf{c}^\top \mathbf{x}$  can be maximized in such a way that none of the linear constraints are met to equality and therefore  $\mathbf{c}^\top \mathbf{x}$  would diverge to infinity. A feasible linear program is therefore a linear program that is neither infeasible nor unbounded and therefore there exists an optimal solution of  $\mathbf{x}$ . Being a well studied type of problem, there exists a plethora of existing algorithms for solving linear programs [4, 13]; often the most involved part of the optimization process is translating the desired task into the form of a linear program.

## 1.3 Overview of work

As previously mentioned, this thesis consists of two main works that aim to improve the noise floor estimation in Sentinel-1 images. As first described in Sections 2.2 and 3.2, default noise floors are provided in Sentinel-1 products that are designed to be subtracted from the original measurements to improve the appearance of the images. However, there are clear issues with the overall fit of the default noise floors that motivate the efforts of the two works. The method in Chapter 2 specifically proposes a linear scaling model using the default noise floor to compensate for the linear mis-fit for each of the subswaths in the images. This is robust in the sense that it optimizes a least squares objective function to estimate very few parameters for each image; only one for each subswath. However, as indicated in Section 2.5 it is apparent that the noise floor is mis-fit in a non-linear manner, which prevents complete compensation with a linear model. In contrast, the second method in Chapter 3 attempts to compensate for the non-linear mis-fit by disregarding the default noise floor and modelling a new noise floor as an affine power function of the antenna radiation power. The method makes use of linear programming to estimate parameters for power functions over different sections of the range, while also computing affine offsets for the different subswaths using least squares. Overall, this results in a solution that can directly compensate for the non-linear mis-fit issues. A caveat is the significant increase in parametric complexity over the linear model, thus making parameter estimation less robust (*cf.* Section 3.5) than in Chapter 2.

In this thesis, both methods adopt similar experiments for validation. The first pair of experiments (Section 2.4.1 and 3.4.1) simulate applying and removing the modelled noise floor on a set of RADARSAT-2 images that do not contain significant noise floor patterns in their original form. The advantage of this type of analysis is that it allows standard image quality metrics to be computed since the clean original image is known and is therefore a good way to determine the efficacy of the parameter estimation procedures. However, these simulations assume that the noise floor encountered in Sentinel-1 images follow the assumptions made by the two respective methods and cannot account for the unknown differences between the model and reality. The second pair of experiments (Section 2.4.2 and 3.4.2) determine the effectiveness of the noise floor estimation directly on Sentinel-1 images by exploiting the backscatter characteristics of open-water. Since open-water typically results in low measured backscatter, such regions are good for determining the remnants of unsubtracted noise floor left over by a correction method. This was quantified by examining the variation of the intensity values over open-water segments with respect to the range, where noise floor varies with the greatest strength. In terms of data used, Chapter 2 uses EW cross-polarized images from IPF version 2.9, while Chapter 3 uses EW and IW cross-polarized images from IPF version 3.1 or above. Source code

of the implemented algorithms can be found at [https://github.com/PeterQLee/https://github.com/PeterQLee/sentinel1\\_denoise\\_rs](https://github.com/PeterQLee/https://github.com/PeterQLee/sentinel1_denoise_rs).

## Chapter 2

# Sentinel-1 Additive Noise Removal from Cross-Polarization Extra-Wide TOPSAR with Dynamic Least-Squares

The following article has been published in the journal *Remote Sensing of Environment*, with the full reference being: P. Q. Lee, L. Xu, and D. A. Clausi. Sentinel-1 additive noise removal from cross-polarization extra-wide topsar with dynamic least-squares. *Remote Sensing of Environment*, 248:111982, October 2020. <https://doi.org/10.1016/j.rse.2020.111982>. Note that the text was reformatted to fit the thesis format. I completed this work by myself under supervision from my supervisors Linlin Xu and David Clausi. This article documents a method to improve the noise-floor estimation in Sentinel-1 EW images that were generated with versions of the Sentinel-1 Instrument Processing Facility Software (IPF) prior to version 3.1. This corresponds to Sentinel-1 images that were acquired prior to June 2019. The method poses a least squares problem to estimate linear scaling parameters for each of the subswaths. While effective in correcting for the majority of the mis-calibration of the noise-floor, there are still non-linear errors in the overall shape of the noise-floor where it is apparent it cannot be corrected by linear scaling parameters. Note that within this article the term “additive noise” is used and is synonymous with “noise-floor”.

# Sentinel-1 Additive Noise Removal from Cross-Polarization Extra-Wide TOPSAR with Dynamic Least-Squares

Peter Q. Lee, Linlin Xu, and David A. Clausi

## Abstract

Sentinel-1 is a synthetic aperture radar (SAR) platform with an operational mode called extra wide (EW) that offers large regions of ocean areas to be observed. A major issue with EW images is that the cross-polarized HV and VH channels have prominent additive noise patterns relative to low backscatter intensity, which disrupts tasks that require manual or automated interpretation. The European Space Agency (ESA) provides a method for removing the additive noise pattern by means of lookup tables, but applying them directly produces unsatisfactory results because characteristics of the noise still remain. Furthermore, evidence suggests that the magnitude of the additive noise dynamically depends on factors that are not considered by the ESA estimated noise field.

To address these issues we propose a quadratic objective function to model the mis-scale of the provided noise field on an image. We consider a linear denoising model that re-scales the noise field for each subswath, whose parameters are found from a least-squares solution over the objective function. This method greatly reduces the presence of additive noise while not requiring a set of training images, is robust to heterogeneity in images, dynamically estimates parameters for each image, and finds parameters using a closed-form solution.

Two experiments were performed to validate the proposed method. The first experiment simulated noise removal on a set of RADARSAT-2 images with noise fields artificially imposed on them. The second experiment conducted noise removal on a set of Sentinel-1 images taken over the five oceans. Afterwards, quality of the noise removal was evaluated based on the appearance of open-water. The two experiments indicate that the proposed method marks an improvement both visually and through numerical measures.



## 2.1 Introduction

Synthetic aperture radar (SAR) is a method of remote sensing that is useful for monitoring the surface of the planet while being insensitive to atmospheric conditions. Applications include topographical mapping through SAR interferometry [8, 42], sea ice mapping/classification [22, 50, 53, 56, 58], oil spill detection [51, 57], ship detection [31, 41], and others [15, 28]. Consequently, SAR imagery is an essential tool for global monitoring. The Sentinel-1 program, which was created and is administered by the European Space Agency (ESA), operates two SAR satellites, Sentinel-1A (launched 2014) and Sentinel-1B (launched 2016), and acquires and distributes SAR images taken over Earth. The diverse set of applications for SAR and the fact that the Sentinel program provides open-data solidifies the potential for research and commercial products.

Sentinel-1 operates in a number of acquisition modes. This paper focuses on the Sentinel-1 extra-wide (EW) mode, which is mainly used over ocean regions, with the images acquired using a method called TOPSAR [59]. Sentinel-1 satellites emit bursts of horizontally or vertically polarized radiation and receive polarized backscatter to form co-polarized images, where the polarization of the emission is the same as the polarization of the received signal, or cross-polarized images, where the polarization of the emission is orthogonal to the polarization of the received signal. A caveat of EW mode for Sentinel-1 is that there are prominent additive noise patterns present in the cross polarization channels with respect to lower backscatter intensity [39, 44, 50]. These are sometimes called banding or scalloping effects in the literature [53, 55]. These noise patterns can cause major issues for interpretation-based tasks because the added intensity corrupts the true backscattered signal of the target [44]. ESA currently provides lookup tables to estimate the additive noise in terms of azimuth and range components as detailed in their Instrument Processing Facility (IPF) product [44], and disseminated through noise calibration *eXtensible Markup Language* (XML) files that are distributed with each Sentinel-1 scene. By interpolating the lookup tables, an estimated additive noise field can be derived for the original image. This paper focuses specifically on data using IPF version 2.91, however as of writing IPF version 3.20 is the latest version that presents improvements in computing the additive noise field. Working with data from IPF versions less than or equal to 2.91 is problematic, however, as subtracting the noise field from the image directly is insufficient as shown by others [27, 39, 50] and ourselves in Section 2.3. The problem is severe enough that some practitioners prefer to discard the first subswath to make modeling easier [50, 22].

While there is a significant body of work aiming to reduce speckle noise [5, 17, 32, 33, 40, 46, 47], there are considerably fewer published methods on reducing the additive noise in SAR. Iqbal *et al.* [26] modeled the additive noise field of ScanSAR images with

gain and offset parameters and implemented a Kalman filter to estimate the parameters for the azimuth and range in a decoupled manner. However, it is not immediately clear how this could be extended to Sentinel-1 EW where the magnitude of the additive noise varies greatly between adjacent subswaths. Specific to Sentinel-1 EW, Karvonen [27] used an approach with a finite impulse response filter to reduce the scalloping in the azimuth direction selectively over ocean regions. However, this has the computationally expensive requirement of computing texture features, with the possibility of incorrectly modifying the intensity of the intended target within the image. Park *et al.* [39] created an approach for Sentinel-1 EW that modifies the estimated noise field with linear scaling and intercept parameters in an attempt to eliminate the additive noise in the image. The values of the parameters were estimated with an iterative grid search regression approach using a large sample of Sentinel-1 ocean scenes, with the mean-estimates of the parameters used for evaluation. A few drawbacks of this approach include the requirement of selecting samples of images across uniform ocean areas, a priori. The method also makes the assumption that the ideal scaling parameters are the same for every scene, an assumption that we found to not always be valid, with an example of this shown in Fig. 2.4. Finally, if one wanted to adapt the method to dynamically estimate the parameters for individual scenes, it would be limited because of the aforementioned uniform ocean requirement.

The method proposed in this paper builds upon the approach of scaling the noise field for each subswath as proposed by Park *et al.* [39]. Our contribution is based both on creating an objective function that incorporates the characteristics of the additive noise and simultaneously choosing scaling parameters for each subswath to minimize the objective function. Our method leads to four main aspects of improvement:

1. Parameters may be estimated on images with heterogeneous features (e.g. containing open-water and sea-ice, cyclones, etc.).
2. No training set of images is needed; the method can be applied for each individual image without prior knowledge of the scenes.
3. Parameters are dynamically estimated for each image. This is significant because the ideal scaling is different for each image, which makes using static parameter estimates suboptimal.
4. The method has a closed-form solution that can be solved exactly without iterative methods.

Ultimately our approach reduces to estimating the parameters of a linear function based on a quadratic objective function using a least-squares solution.

Two experiments were performed to evaluate the effectiveness of the proposed denoising method. The first experiment simulated denoising by applying randomly scaled noise fields to non-SAR Sentinel-2 images and then denoising them with the proposed method. The second experiment used a sample of HV and VH polarized Sentinel-1 EW images from all five oceans and evaluated the proposed method in terms of the flatness of the result over selected subregions that were expected to be flat. These experiments ultimately indicated that the proposed method was a significant improvement over the baseline method provided by ESA and also that estimating parameters for each image independently is beneficial compared to a static estimation approach. We also perform a small experiment on data processed with an IPF above 3 that resulted in some modest improvement. Therefore, this work is useful for any application that uses EW cross-polarized Sentinel-1, such as ice analysis, as the method provides significantly better denoising and does not require expensive computation or large amounts of prior information or training sets.

## 2.2 SAR noise background

Before details on the mechanics of the noise are provided, a brief background of TOPSAR will first be given. TOPSAR is a type of SAR acquisition that captures a wide swath area without the typical loss of resolution or scalloping [59]. The method works by simultaneously acquiring subswaths that cover different elevation angles (the angle between the ground target and the satellite) by steering the antenna aperture to focus at different elevation angles while continuously rotating along the azimuth angle. Sentinel-1 incorporates TOPSAR in two modes, interferometric wide (IW) swath mode, and extra wide (EW) swath mode. EW mode has subswaths enumerated as EW1, EW2, EW3, EW4, and EW5 that are ordered by increasing elevation angle along the range. During the observation period, the satellite sweeps a number of radar bursts along the azimuth and observes the backscattered radiation for each of the five subswaths. The received signals from each of the bursts are stitched along the azimuth direction (the direction of the satellite’s orbital velocity) to form the rows of the image, while the signal corresponding to the five subswaths along the range (the direction perpendicular to the satellite’s orbital velocity and tangent to the Earth’s surface) are stitched together to form the columns of the image. In the supplementary materials we provide an animation that approximates the TOPSAR process.

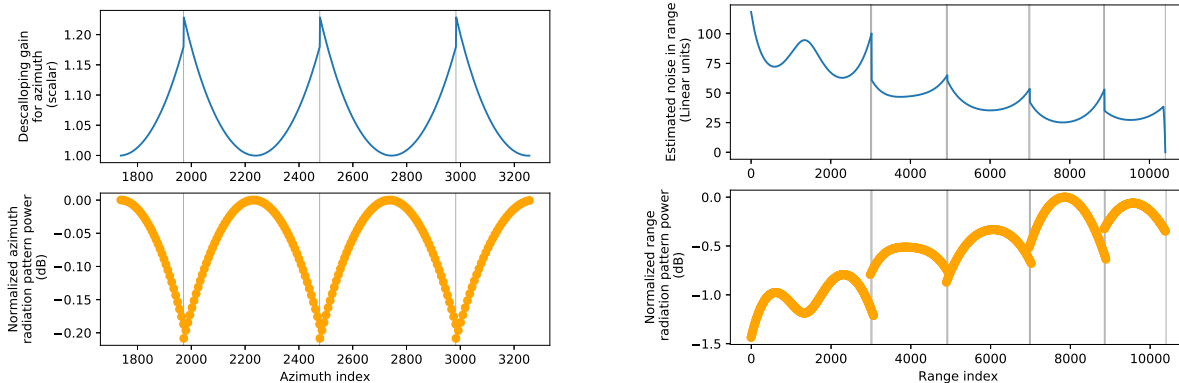
ESA provides a forward model for estimating the additive noise induced by TOPSAR as a function of a number of factors

$$y_a(i, j) = \frac{D(i)P(a, i)}{E(a, i, j)R(j)}f, \quad (2.1)$$

for azimuth index  $i$ , range index  $j$  that are within a subswath  $a$  [43].  $P(a, i)$  is the power gain term that is used for drift correction while orbiting.  $R(j)$  is the range spreading loss term used to correct errors from the range compression algorithm. Scalar  $f$  is calibration parameter determined by the noise and the processor. The remaining two terms are based on the radiation pattern of the antennas, with  $D(i)$ , the descalloping gain, being inversely proportional to the antenna array pattern with respect to the azimuth, and  $E(a, i, j)$ , the elevation antenna pattern gain, being proportional to the antenna pattern with respect to the range. The reader is referred to [43] for additional details. In antenna theory, the power of the radiation pattern for an antenna is directly related to the strength of the received signal at the corresponding angle from the receiving antenna [52]. Consequently, the radiation pattern is a fundamental variable for the shape of the additive noise.

As Sentinel-1 uses an array antenna, the observed signal in the azimuth direction will naturally be an aggregate function of the radiation patterns for each element in the array as they are rotated along the azimuth [43, 52]. Fig. 2.1a shows an example of the relationship between the average antenna element pattern for the burst along the azimuth, derived from the Sentinel-1 calibration XML file, and azimuth component of the estimated noise. As the bursts are stitched along the azimuth [59], the aggregate pattern appears as U-shaped and symmetric. The corresponding angles closer to the burst centre have higher gain, which reduces the magnitude of additive noise compensation needed. Angles further from the centre have less antenna-gain and require more noise compensation.

The negative relationship between the noise and radiation pattern is apparent in the range direction as well. Fig. 2.1b shows a comparison between the range noise and the radiation pattern for each subswath. When the antenna is steered to acquire a different elevation angle, and hence different subswath, the subsequent radiation pattern changes. This is most notable in the first subswath, where the radiation pattern has two main lobes (local maxima of the gain). The remaining subswaths only have one main lobe, but have different relative magnitudes of radiation power.



(a) Top: The estimated noise contribution in the azimuth direction (descalloping gain). Bottom: Average radiation pattern power gain with respect to azimuth. The vertical demarcations indicate the beginning and end of observations obtained from a burst. Only a portion of the azimuth is shown for brevity.

(b) Top: The estimated noise contribution in the range direction. Bottom: Radiation pattern power gain with respect to range. The vertical demarcations indicate the beginning and end of subswaths.

Figure 2.1: Comparison between the estimated noise contributed by the azimuth and range with respect to radiation pattern for EW TOPSAR. The measurements for the antenna pattern were initially given in angles and were converted to the corresponding range and azimuth indices in order to show the negative relationship between noise and radiation pattern. The measurements correspond to the noise field as shown in Fig. 2.2.

Within the noise calibration XML files in every Sentinel-1 EW product, as of IPF 2.9, the information to compute the noise field  $y_a(i, j)$  is provided within two different lookup tables labelled as the *noiseRangeVector*, which models  $y_a(i, j)/D(i)$ , and the *noiseAzimuthVector*, which models  $D(i)$ . By performing linear interpolation between entries in the lookup tables and multiplying the two results together, the estimated noise field  $y_a(i, j)$  can be constructed. Given  $x$  as the square of the digital pixel values in the original image, ESA recommends denoising the measurements by subtracting the noise field from the image

$$\phi_a(i, j) = x_a(i, j) - y_a(i, j), \tag{2.2}$$

where the square root of  $\phi$  returns the result to the original linear units / digital values [44]. As this step is performed prior to any other calibration procedures, which differ based on application, we will continue to operate in terms of linear units throughout this paper.

Further, for a given subswath  $a \in \mathcal{A} = \{\text{EW1}, \text{EW2}, \text{EW3}, \text{EW4}, \text{EW5}\}$ , let the azimuth row and range column be  $(i, j) \in a$ . Then 2.2 is represented more succinctly as

$$\phi_a = x_a - y_a. \quad (2.3)$$

However, applying (2.3) directly is insufficient. Fig. 2.2 provides a visualization of the process of constructing the noise field and the result of subtracting it from the original image. The subtraction results in subswaths being under or over compensated. For example, Fig. 2.3 shows the values along the azimuth and range directions of an open-water area, where the result has noise patterns still present. This implies that the strength of the noise field needs to be scaled differently for each subswath. Park *et al.* [39] proposed a method that chooses vectors for scaling coefficients  $\bar{\mathbf{k}} = [\bar{k}_{\text{EW1}}, \bar{k}_{\text{EW2}}, \bar{k}_{\text{EW3}}, \bar{k}_{\text{EW4}}, \bar{k}_{\text{EW5}}]$  and intercepts  $\bar{\mathbf{o}} = [\bar{o}_{\text{EW1}}, \bar{o}_{\text{EW2}}, \bar{o}_{\text{EW3}}, \bar{o}_{\text{EW4}}, \bar{o}_{\text{EW5}}]$  such that

$$\bar{\phi}_a = x_a - \bar{k}_a y_a + \bar{o}_a \quad (2.4)$$

where  $\bar{\mathbf{k}}$  and  $\bar{\mathbf{o}}$  were statically estimated using a training set of several hundred images.

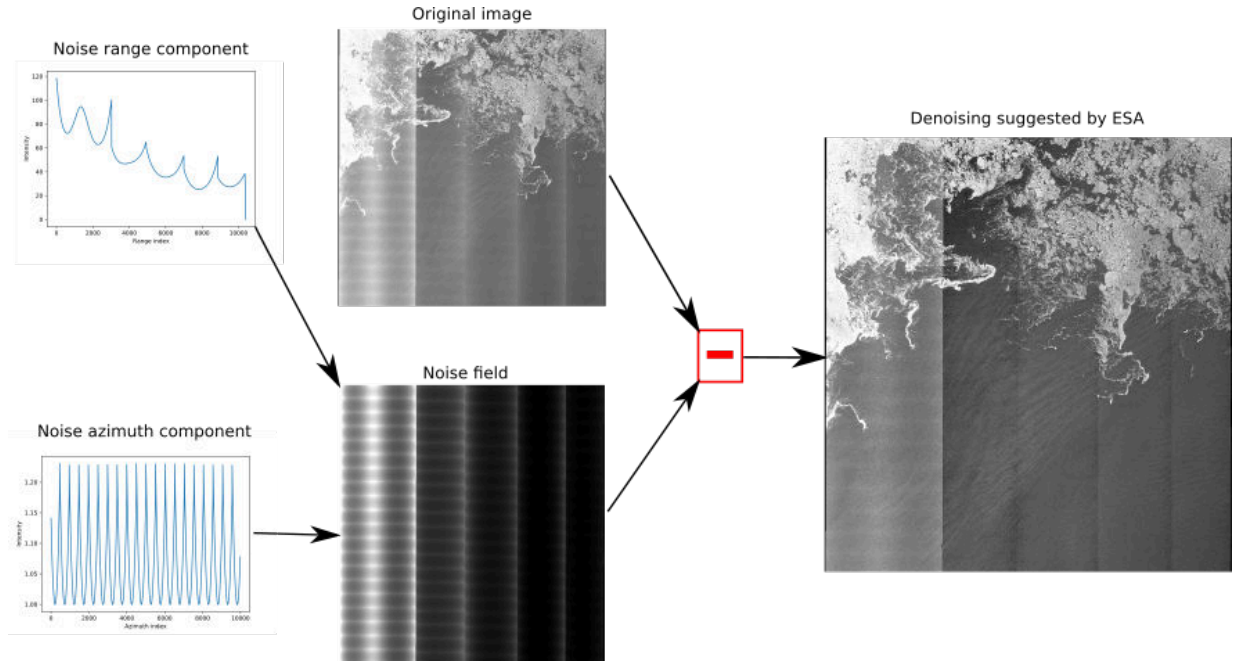
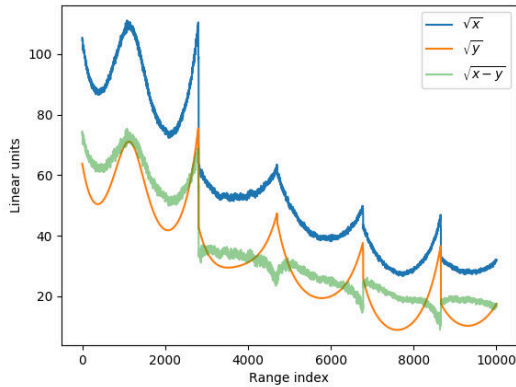
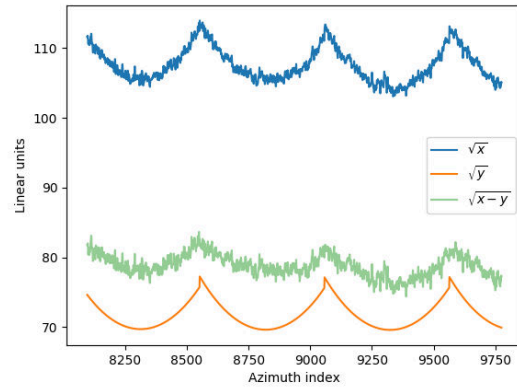


Figure 2.2: Visualization of the construction and application of the noise field using the noise vectors. Overall, the final denoising is unsatisfactory, most prominently in EW1 where patterns of the noise field are blatant in the result image.



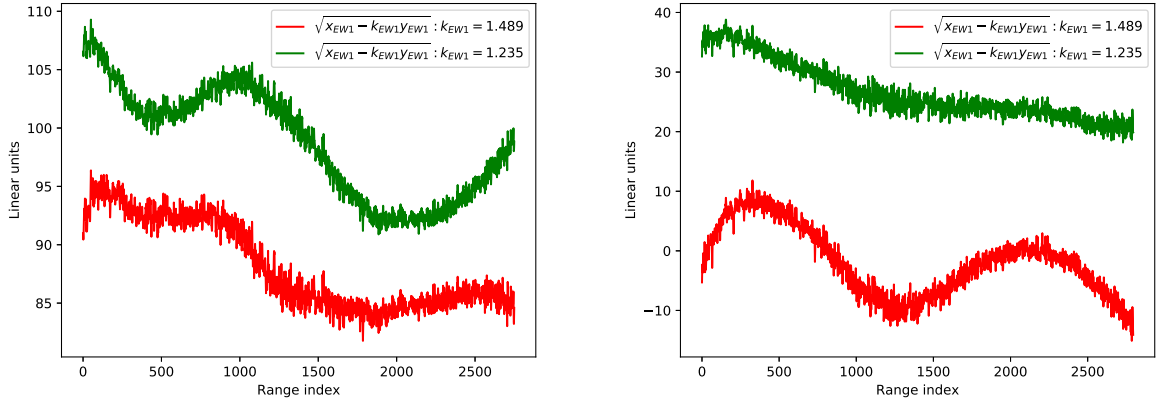
(a) Mean intensity of measurement, noise, and their difference over ocean area with respect to **Range**.



(b) Mean intensity of measurement, noise, and their difference over ocean area with respect to **Azimuth** for EW1.

Figure 2.3: Plots of mean intensities of measurements in sections of ocean with respect to each direction. Ideally the subtraction would produce a flat profile, but aspects of the noise are still present in both directions.

Another element to consider is whether the ideal scaling parameters are dependent on factors other than the sensor. Fig. 2.4 shows that single values of  $k$  do not universally fit between different images. Therefore, it would be ideal for scaling factors to be estimated dynamically for each image.



(a) Scene with a higher magnitude of additive noise. (b) Scene with a lower magnitude of additive noise.

Figure 2.4: A comparison of the mean measurement of EW1 over ocean regions of two different scenes after noise removal with two different scaling factors ( $k$ ). At  $k = 1.2350$  the left scene has noise patterns present while the right scene has a flat profile. However, at  $k = 1.4886$  the left scene as the noise patterns better compensated, but results in the right scene being overcompensated. This indicates that no single scaling factor will fit every scene.

## 2.3 Methods

The goal of this work is to estimate appropriate scaling parameters for each image individually. We make a similar assumption to Park *et al.* [39] that the estimated noise in each subswath needs to be linearly re-scaled. Our dynamic model uses a set of dynamically estimated scaling parameters  $\hat{\mathbf{k}} = [\hat{k}_{EW1}, \hat{k}_{EW2}, \hat{k}_{EW3}, \hat{k}_{EW4}, \hat{k}_{EW5}]$  such that

$$\hat{\phi}_a = x_a - \hat{k}_a y_a \quad (2.5)$$

Our model is distinct from (2.4) because the scaling parameters,  $\hat{\mathbf{k}}$ , are estimated for each image independently. We also considered using a set of intercepts  $\hat{\mathbf{o}}$  but found that including these did not make a significant impact on the end results. To estimate parameters for each image independently, an objective function,  $L$ , is defined based on the characteristics of the estimated additive noise present within each image. The values of  $\hat{\mathbf{k}}$  are thereby chosen to minimize  $L$  such that  $\hat{\mathbf{k}} = \underset{\hat{\mathbf{k}}}{\operatorname{argmin}} L$ .



Throughout the remainder of this section we describe the main components of the objective function ( $L$ ) based on the noise characteristics in both the azimuth and range directions. Thus,  $L$  is defined as the sum of terms based on the noise-characteristics in the azimuth direction ( $L^A$ ), the range direction ( $L^R$  and  $L^B$  that correspond to effects within and between subswaths respectively), and a term for regularization ( $L^r$ ). Each of these terms involve summing the square difference between different pairs of samples within the images. These terms are defined with more detail in the remainder of this section, but [Fig. 2.5](#) provides a high-level visual overview of how  $L$  is computed.

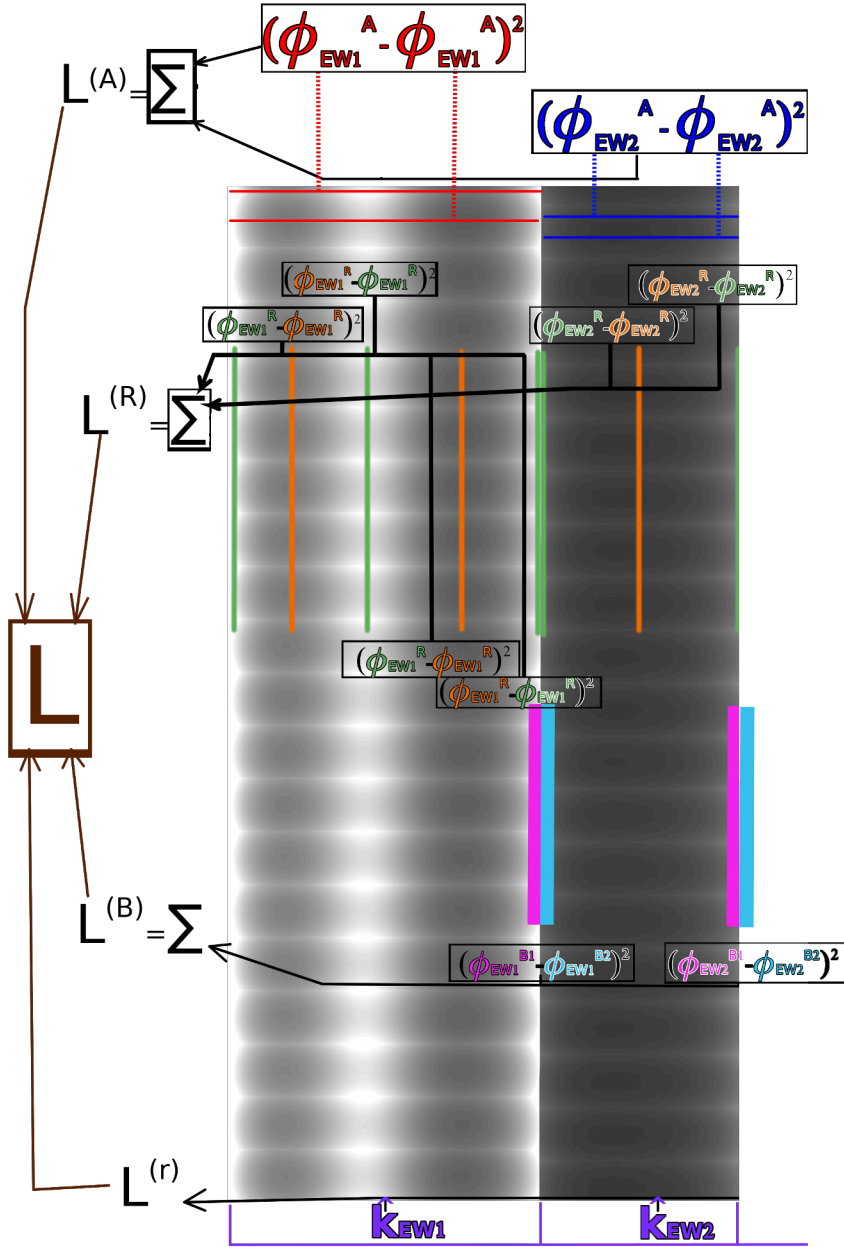


Figure 2.5: High level overview of the objective function for the first two subswaths, for simplicity. The noise field is overlaid with abridged annotations relating to the azimuth noise loss ( $L^A$ ), range noise loss ( $L^R$  and  $L^B$ ), and regularization loss ( $L^r$ ). While the annotations are overlaid on the noise field to convey the indices of the points used in the terms, note that the loss is a function of the measured SAR image, the estimated noise field, and the scaling parameters. Best viewed in colour.

### 2.3.1 Objective: Azimuth

A prominent attribute of the azimuth component of the noise is its periodic pattern. As explained previously, the pattern is caused by the U-shaped antenna pattern gain and the concatenation of bursts along the azimuth. Thus, the period of the azimuth noise is equivalent to the number of azimuth lines between the bursts, such that the troughs (local minima) of the azimuth noise correspond to centre of bursts (azimuth angle is 0) and are each one period apart. Also, since the gain is U-shaped, each peak (local maxima) of the azimuth noise is located half a period away from a trough. Therefore, we assert that if the amplitude of the noise is high, then the difference between the adjacent peaks and troughs will be high.

More generally, since the estimated noise within each burst is U-shaped and symmetric, we assume that the squared difference in the image between any pair of points along the azimuth will be proportional to the amplitude of the noise. Therefore, the pairs are selected as all possible points along the azimuth within each subswath paired with the points offset by half a period. Fig. 2.6a graphically shows this layout with respect to the azimuth.

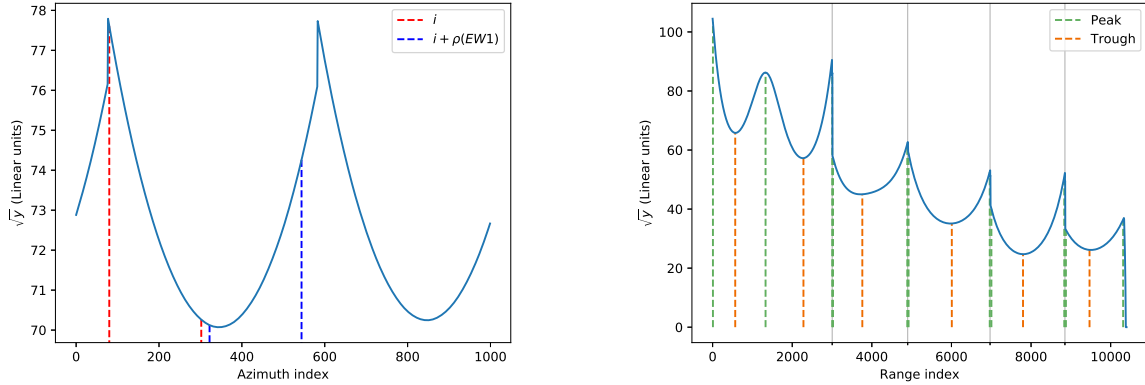
Given the denoising model for subswath  $a$  as  $\hat{\phi}_a$ , let  $\hat{\phi}_a^A(i)$  be the average value of all pixels for azimuth line  $i$  in  $\hat{\phi}_a$ . Then the azimuth component of the loss function is composed as

$$L^A = \sum_{a \in \mathcal{A}} \sum_i^{N_{az}(a)} [w_a^A(i) [\hat{\phi}_a^A(i) - \hat{\phi}_a^A(i + \rho(a))]]^2, \quad (2.6)$$

where  $\rho(a)$  is the number of azimuth lines per half a burst period, computed as

$$\rho(a) = \frac{N_{burst}(a)}{2N_{az}(a)} \quad (2.7)$$

and  $N_{burst}(a)$  is the number of bursts used to construct subswath  $a$  and  $N_{az}(a)$  is the total number of azimuth lines in the subswath. Unfortunately, information containing  $N_{burst}(a)$  is not explicitly included in the current IPF version (2.9). However, it can be derived as  $N_{burst}(a) = N_{ap}(a) + 1$ , where  $N_{ap}$  is the number of *antennaPattern* items for subswath  $a$  within the annotation XML file. The term  $w_a^A(i)$  is a weighting term introduced for subswath  $a$  and azimuth line  $i$  based on the realization that the change in intensity between pairs of lines separated by half a burst is influenced by the backscatter of the ground targets. If the two targets have fundamentally different backscattering properties, for example where one line is dominated by ice and the other is dominated by water, then their squared difference will not be representative of the scale of the noise field in the measurement. Given  $x_a^A$  and  $y_a^A$  as the average values on an azimuth line that are



(a) Noise with respect to azimuth in EW1. The dashed lines show pairs of points that are offset by half a burst period that are used by the objective function.

(b) Range noise with peaks and troughs over all five subswaths. The solid lines divide the subswaths, with the troughs and peaks marked by the dashed lines.

Figure 2.6: Peaks and troughs of the estimated noise with respect to azimuth and range.

used in  $\hat{\phi}_a^A$ , the term  $\frac{x_a^A(i) - x_a^A(i + \rho(a))}{y_a^A(i) - y_a^A(i + \rho(a))}$  is used to determine whether a sample's difference is dominated by the change in intensity from the backscattering of the targets. We determined an acceptable range as 0 to 2.5. The lower bound was zero because a negative ratio cannot be created from the additive noise, assuming the noise model is correct. A liberal upper bound was chosen as 2.5 based on experimentation. Thus, the weighting term is defined as

$$w_a^A(i) = \begin{cases} 1 & \text{if } 0 < \frac{x_a^A(i) - x_a^A(i + \rho(a))}{y_a^A(i) - y_a^A(i + \rho(a))} < 2.5 \\ 0 & \text{otherwise} \end{cases} \quad (2.8)$$

to remove the outlying pairs from the loss function.

As proven in the appendix, (2.6) can be represented using an inner product formulation

$$L^A = [\mathbf{v}^A - \mathbf{C}^A \hat{\mathbf{k}}]^\top [\mathbf{v}^A - \mathbf{C}^A \hat{\mathbf{k}}]. \quad (2.9)$$

### 2.3.2 Objective: Range

As noted previously, the noise pattern in the range direction is unique for each subswath. Thus, two objective function terms,  $L^R$  and  $L^B$ , are proposed to compensate the noise within the subswaths (intra-subswath) and between the subswaths (inter-subswath).

## Intra-subswath

First we examine the intra-subswath loss term that describes the noise pattern *within* each subswath. Like the azimuth loss term, the intra-subswath loss term is constructed by taking the squared difference between peaks and troughs but within the range component. The range noise pattern is neither periodic nor symmetric; instead the true scale of the noise is indirectly measured from taking the squared difference between peaks and troughs exclusively. Fig. 2.6b shows the samples used with respect to the range direction. The samples used in the intra-subswath term are based on the rectangular subregions divided along the azimuth of a subswath that are dictated by the *swathBoundList* field in the noise calibration XML file, as depicted in Fig. 2.7. The intra-subswath loss is based on the difference between adjacent peaks and troughs over each of the subregions. Let  $p_b(z)$  and  $t_b(z)$  be the  $z^{\text{th}}$  peak and trough respectively within rectangular subregion  $b$  in subswath  $a$ . Now let  $\hat{\phi}_b^R(s)$  be the mean average of values predicted by the denoising model  $\hat{\phi}$  within rectangular subregion  $b$  in subswath  $a$  that have a range index within  $s - \epsilon$  to  $s + \epsilon$ , with a padding constant  $\epsilon$  and  $s$  being either  $p_b(z)$  or  $t_b(z)$ . Since the range noise pattern is unimodal in EW2, EW3, EW4, and EW5 (loss term  $M$ ), while multi-modal in EW1 (loss term  $N$ ), the intra-subswath loss is composed as the sum of two terms

$$L^R = M + N, \quad (2.10)$$

where

$$\begin{aligned} M = \sum_{a \in \mathcal{M}} \sum_{b \in a} & [[w_b^R(1)[\hat{\phi}_b^R(p_b(1)) - \hat{\phi}_b^R(t_b(1))]]^2 \\ & + [w_b^R(2)[\hat{\phi}_b^R(t_b(1)) - \hat{\phi}_b^R(p_b(2))]]^2] \\ & \text{such that } \mathcal{M} = \{\text{EW2, EW3, EW4, EW5}\} \end{aligned} \quad (2.11)$$

and

$$\begin{aligned} N = \sum_{b \in \text{EW1}} & [[w_b^R(1)[\hat{\phi}_b^R(p_b(1)) - \hat{\phi}_b^R(t_b(1))]]^2 \\ & + [w_b^R(2)[\hat{\phi}_b^R(t_b(1)) - \hat{\phi}_b^R(p_b(2))]]^2 \\ & + [w_b^R(3)[\hat{\phi}_b^R(p_b(2)) - \hat{\phi}_b^R(t_b(2))]]^2 \\ & + [w_b^R(4)[\hat{\phi}_b^R(t_b(2)) - \hat{\phi}_b^R(p_b(3))]]^2] \end{aligned} \quad (2.12)$$

As in the azimuth noise component, weighting terms  $w^R$  were introduced to account for instances where the difference is dominated by the difference in land targets (e.g. land vs ice). In this case the weighting term is defined as

$$w_b^R(o) = \begin{cases} \mu & \text{if } 0 < \frac{x_b^{R1} - x_b^{R2}}{y_b^{R1} - y_b^{R2}} < 2.5 \\ 0 & \text{otherwise} \end{cases}, \quad (2.13)$$

where  $\hat{\phi}_b^R(p_b(o+q)) - \hat{\phi}_b^{R2}(t_b(o)) = [x_b^{R1} - k_a y_b^{R1}] - [x_b^{R2} - k_a y_b^{R2}]$  with  $o \in \{1, 2\}$  and  $q \in \{0, 1\}$  such that they correspond with the difference terms in (2.11) and (2.12). The value  $\mu$  balances the trade-off between  $L^A$ , which is summed over a larger number of terms. From experimentation we chose  $\mu = 1.79$ .

Finally, the proposed error for the intra-subswath range noise can be rewritten as an inner product

$$L^R = [\mathbf{v}^R - \mathbf{C}^R \hat{\mathbf{k}}]^\top [\mathbf{v}^R - \mathbf{C}^R \hat{\mathbf{k}}], \quad (2.14)$$

as shown in the appendix.

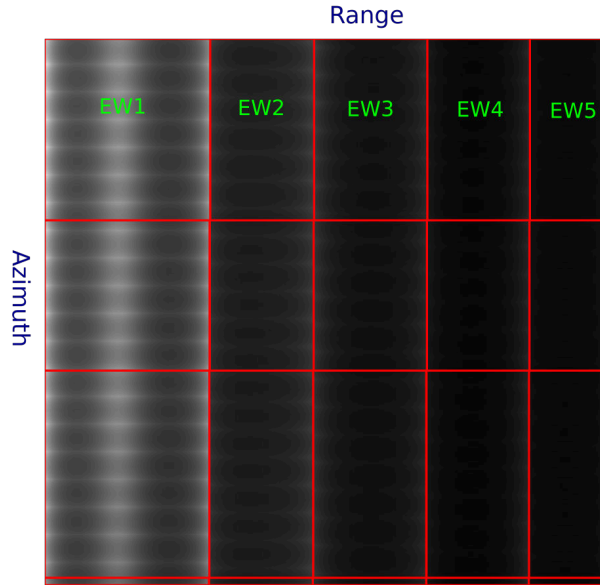


Figure 2.7: Layout of the rectangular subregions  $b$  in red overlaid with the estimated noise pattern for reference.

### Inter-subswath

As the radiation pattern changes when the antenna switches between subswaths, we must consider that this will cause discontinuities between adjacent subswaths. Intuitively, the range columns of adjacent subswaths are spatially correlated and should have similar values in an ideal denoised image. We introduce another loss term to represent the difference of intensity between the columns of adjacent subswaths to handle these considerations.

Let  $\hat{\phi}_b^{B1}$  be the average predicted value of the last  $\epsilon$  range columns that are within subrectangle  $b$  in subswath  $a$  and let  $\hat{\phi}_b^{B2}$  be the average of the  $\epsilon$  range columns after the last column in subrectangle  $b$ . Then the inter-subswath loss term is determined by

$$\begin{aligned} L^B &= \sum_{a \in \mathcal{B}} \sum_{b \in a} [\hat{\phi}_b^{B1} - \hat{\phi}_b^{B2}]^2 \\ &= [\mathbf{v}^B - \mathbf{C}^B \hat{\mathbf{k}}]^\top [\mathbf{v}^B - \mathbf{C}^B \hat{\mathbf{k}}] \\ &\text{such that } \mathcal{B} = \{\text{EW1, EW2, EW3, EW4}\} \end{aligned} \tag{2.15}$$

### 2.3.3 Regularization

Even with weight terms in the loss function, using each of the aforementioned loss terms can result in unstable estimates  $\hat{\mathbf{k}}$ . To resolve this, a prior assumption is made that each value of  $\hat{\mathbf{k}}$  should be close to 1. Thus a regularization term is introduced to penalize estimates of  $\hat{\mathbf{k}}$  that diverge from 1

$$\begin{aligned} L^r &= \sum_a [\lambda_a [1 - \hat{k}_a]]^2 \\ &= [\mathbf{1} - \mathbf{C}^r \hat{\mathbf{k}}]^\top [\mathbf{1} - \mathbf{C}^r \hat{\mathbf{k}}], \end{aligned} \tag{2.16}$$

where  $\mathbf{C}^r$  is the diagonal matrix containing the hyper-parameter vector  $\boldsymbol{\lambda}$ . By applying the Golden section search algorithm in a block-wise manner, we found appropriate values of  $\boldsymbol{\lambda} = [0.1, 0.1, 6.75124, 2.78253, 10]$ , used for all images. Now that we have introduced the loss terms, we now detail the implementation for estimating the scaling parameters for each subswath.

### 2.3.4 Implementation

Recall that the standard denoising method proposed by ESA recommends denoising as

$$\phi_a = x_a - y_a. \tag{2.17}$$

As it is apparent that this is not sufficient in some scenarios, the desired model scales the noise factor according to each subswath  $a$  with  $\hat{k}_a$

$$\hat{\phi}_a = x_a - \hat{k}_a y_a \tag{2.18}$$

Through matrix and vector concatenation the final loss term is defined as the sum of all the previously derived terms in a single inner product

$$\begin{aligned} L &= L^A + L^R + L^B + L^r \\ &= [\mathbf{v} - \mathbf{C}\hat{\mathbf{k}}]^\top [\mathbf{v} - \mathbf{C}\hat{\mathbf{k}}] \end{aligned} \tag{2.19}$$

and the solution for  $\underset{\hat{\mathbf{k}}}{\operatorname{argmin}} L$  is well known [9, 16] to be the least-squares solution

$$\hat{\mathbf{k}} = [\mathbf{C}^\top \mathbf{C}]^{-1} \mathbf{C}^\top \mathbf{v}. \tag{2.20}$$

## 2.4 Experiments

To evaluate the effectiveness of our method, two experiments were considered. The first experiment is a simulation where a set of RADARSAT SAR images without significant additive noise patterns are selected to demonstrate the abilities of the proposed method in a setting where the characteristics of the noise are directly controlled. The second experiment considers denoising Sentinel-1 EW images in both HV and VH polarization and evaluates the effectiveness by examining sub-regions of open-water.

### 2.4.1 Parameter re-estimation simulation on RADARSAT

The simulation experiment can be summarized by the following: first RADARSAT images were selected, a scaled noise field was added to the images, scaling parameters were re-estimated on the noisy image, followed by denoising the noisy image with the model and comparing the result with original ground truth images. The RADARSAT images were selected to ensure that a ground truth reference image was available and independent of the additive noise patterns specific to Sentinel-1 EW. The goal of this experiment is to test if the proposed method can accurately estimate the optimal scaling parameters and verify the quality of the denoised image compared to a true original.

The set of images used for the experiments were 20 RADARSAT HV images taken in the Beaufort Sea during 2010. A template SAR noise field was selected from a sample Sentinel-1 scene<sup>1</sup>. To ensure comparability, the values of the RADARSAT scene prior to adding noise were re-scaled to have a comparable signal to noise ratio as the original Sentinel-1 scene after denoising with the proposed method. The RADARSAT scene was

---

<sup>1</sup>The sample scene was from S1A\_EW\_GRDM\_1SDH\_20180902T164932\_20180902T165032\_023522\_028FAA\_5A8B



also spatially re-scaled with linear interpolation to have the same number of rows and columns as the Sentinel-1 scene.

For each image, 10 different noisy versions were constructed with scaling factors randomly selected from uniform distributions within the ranges  $k_{EW1} : [1.2, 1.6]$ ,  $k_{EW2} : [0.8, 1.0]$ ,  $k_{EW3} : [0.92, 1.02]$ ,  $k_{EW4} : [0.95, 1.05]$ ,  $k_{EW5} : [0.98, 1.02]$ , resulting in a total of 110 noisy images. These ranges for  $\mathbf{k}$  were selected as they were representative of the range of estimated parameters encountered in the sample of true SAR images discussed in the following subsection. The noisy images were created by multiplying the noise field with the scaling parameters and adding it with the original image. Then, using (2.20), the parameters were estimated, with the scaled subtraction labelled as the **proposed** denoising. As a *baseline*, we perform the aforementioned procedure using scaling estimates as  $\bar{\mathbf{k}} = [1.4, 0.925, 0.985, 1.0, 1.0]$ , which are the central values of the distributions. In addition, a visual comparison is shown in Fig. 2.8.

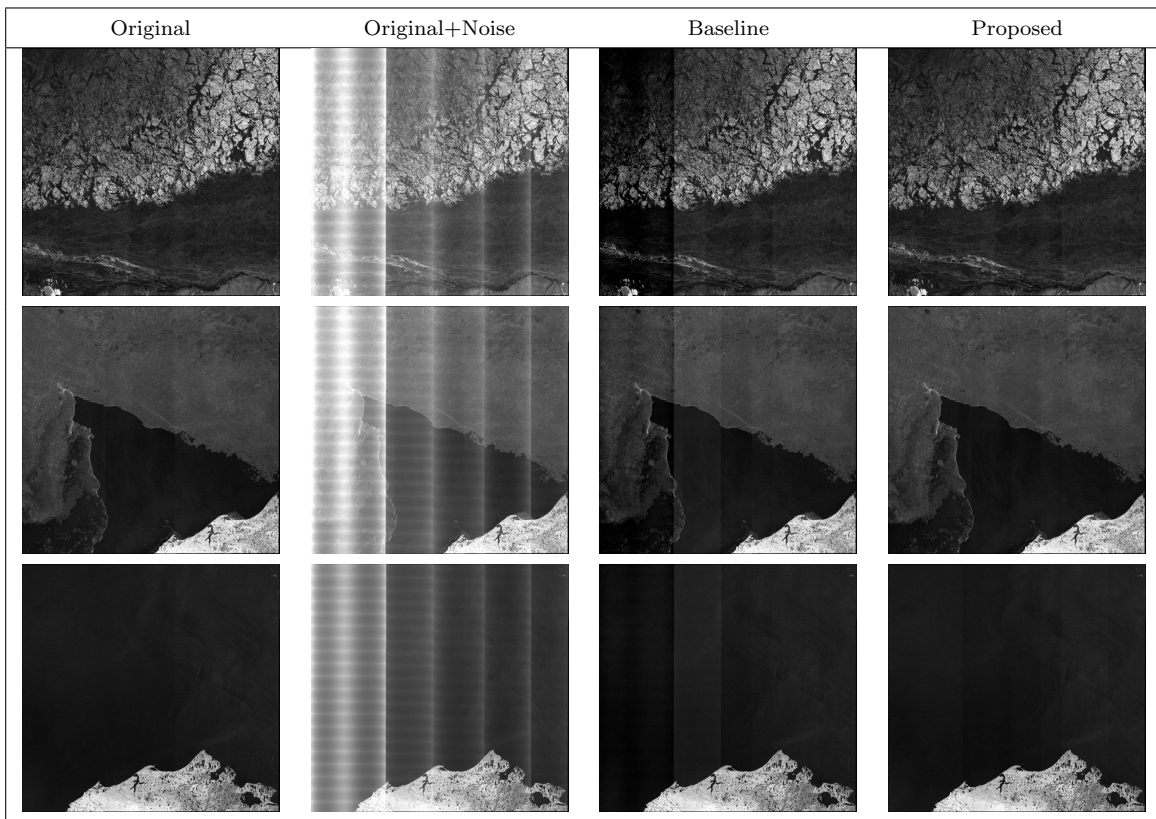


Figure 2.8: Comparison of images within the simulation experiment with  $\hat{k} = [1.55, 0.833, 1.01, 1.01, 1.01]$ . The proposed method is almost identical to the original image, while the image from the baseline method is scaled improperly between the simulated first and second subswaths.

Three metrics, the normalized root mean squared error (NRMSE), peak signal to noise ratio (PSNR), and structural similarity index (SSIM) [54], were computed with respect to the original image to determine the effectiveness of denoising. NRMSE computes the square root of the aggregate sum of pixel-wise squared differences, with a lower-bound of 0 indicating a perfect comparison. In contrast to root mean squared error, NRMSE is normalized by dividing the root sum of squares by the range of input values for each image, which helps ground the metric against a comparison that vary in scale [6]. We use a common variant of NRMSE as

$$NRMSE(\mathbf{d}, \mathbf{l}) = \frac{\sqrt{MSE(\mathbf{d}, \mathbf{l})}}{\max(\mathbf{l}) - \min(\mathbf{l})}, \quad (2.21)$$

where  $MSE(\mathbf{s}, \mathbf{l})$  is the mean squared error between prediction vector  $\mathbf{d}$  and baseline vector  $\mathbf{l}$ . PSNR computes the logarithmic ratio of power of the original image to the power of the noise within the modified image. PSNR is commonly used in applications that result in distortion of the original image in denoising or compression applications [21, 25]. Finally, SSIM is a metric bounded between 0 and 1, with 1 indicating the two images are identical, and is commonly used for evaluating denoising and reconstruction methods by quantifying the similarity of structural features within an image [54]. Each of these metrics make use of the available ground truth reference image. The summary of the metrics with respect to the denoising procedures over the distribution of images are shown in Table 2.1, with the metrics for the applying no denoising (*noisy*) included for context.

To compare the generated distributions between the proposed and baseline methods for each of the metrics, we employed a one-tailed paired t-tests using a critical value  $\alpha = 0.05$ . We found our method had significantly higher SSIM and PSNR and lower NRMSE than the baseline method ( $p < \alpha$ ), indicating it is significantly better in terms of all three metrics.

Table 2.1: Mean  $\pm$  standard deviation for the normalized root mean squared error (NRMSE), peak signal to noise ratio (PSNR), and structural similarity index (SSIM) over all the images with 10 iterations of sampling values for  $k$ . P-values from the one-tailed t-test comparing the **proposed** method to the other methods are also shown.

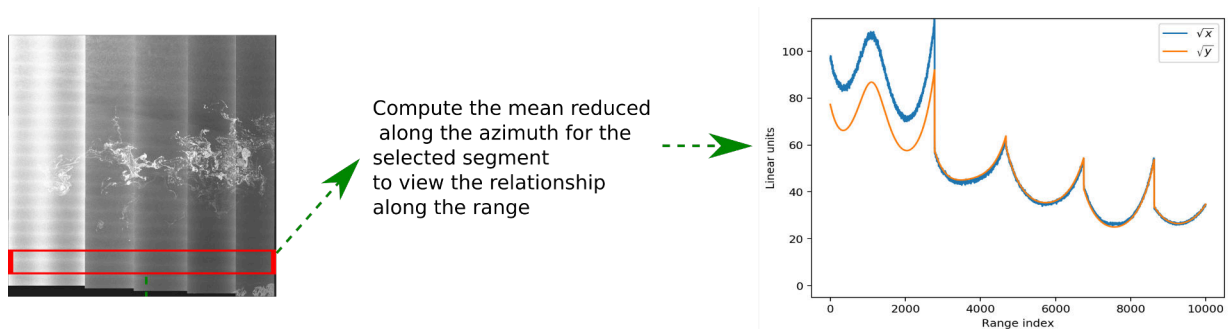
Method	NRMSE	p-value	PSNR	p-value	SSIM	p-value
<i>Noisy</i>	$0.514 \pm 0.028$	$\approx 0.0$	$20.9 \pm 2.0$	$\approx 0.0$	$0.913 \pm 0.009$	$\approx 0.0$
<i>Baseline <math>\bar{\mathbf{k}}</math></i>	$0.061 \pm 0.031$	$1.5 \times 10^{-47}$	$41.4 \pm 5.6$	$3.8 \times 10^{-57}$	$0.993 \pm 0.005$	$9.8 \times 10^{-23}$
<b>Proposed</b>	<b><math>0.017 \pm 0.008</math></b>	N/A	<b><math>51.4 \pm 3.8</math></b>	N/A	<b><math>0.997 \pm 0.001</math></b>	N/A

## 2.4.2 Denoising Sentinel-1 SAR

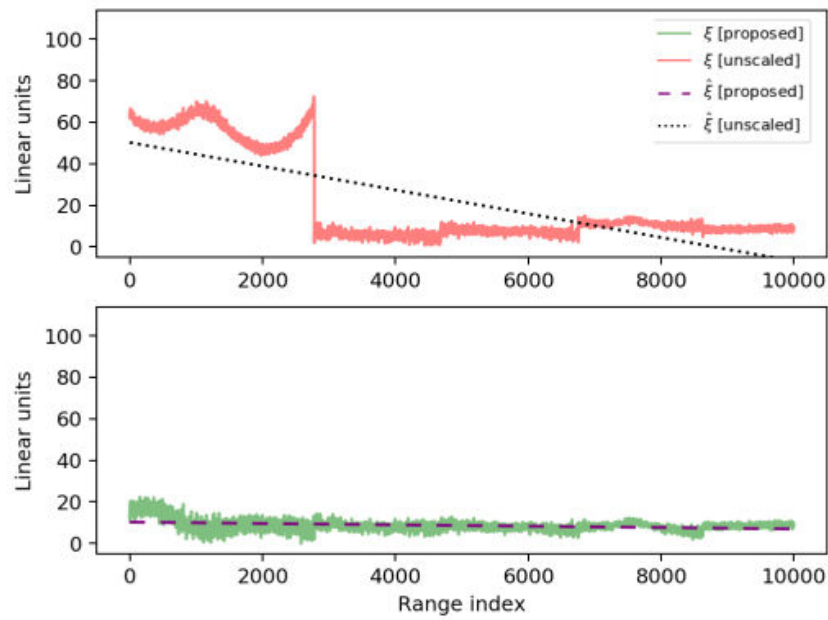
For the second experiment, a set of 41 Sentinel-1 GRDM SAR images was selected to include 13 images from the Arctic Ocean, 6 from the Antarctic Ocean, 8 from the Atlantic Ocean, 6 from the Pacific Ocean, and 8 from the Indian Onnncean. The images were selected from all five oceans to ensure our evaluation would not be biased towards a single environment. The images from the Arctic and Antarctic oceans have HV polarization while the images from the Atlantic, Pacific, and Indian oceans have VH polarization. The polarization of the images is determined by the Sentinel-1 observational scenario [12]. In the remainder of this section we provide both a visual and a quantitative comparison of the proposed and baseline denoising procedures.

Fig. 2.10 and Fig. 2.11 visually present a subset of co-polarized images from all five major ocean divisions. Three types of images are shown: the original image, the scene with ESA denoising, and the scene with a scaled noise field scaled and subtracted via the proposed method. For display purposes only, the images were linearly scaled from 0 to 255 for each scene based on the 2.5 to 97.5 percentile of the distribution of intensities for all versions of the scene in order to maximize the contrast in each image. Visually, the proposed method greatly reduces the noise characteristics from each of the images, although there are still some discontinuities in some of the images. This is not an error in the parameter estimation, but rather in the assumption that the noise field is linearly mis-scaled. More detail regarding this is provided in Section 2.5.

For the quantitative comparison of the experiment, we selected rectangular sub-regions in the image that spanned the entire range (all five subswaths) and were over open-water without major textural features. We make the assumption that the intensity over such sub-regions will not vary significantly with respect to range when the image is ideally denoised. A similar method of evaluation was also used in Park *et al.* [39]. Consequently, we assume that the mean intensity of these sub-regions should follow a linear relationship, with deviation from a linear relationship implying the presence of noise. Let  $\xi(j)$  be the mean value along the azimuth on range index  $j$  for a denoised image. Let  $\hat{\xi}(j)$  be the linear fit for  $\xi(j)$ , which as previously mentioned, should be a reasonable estimate for  $\xi(j)$ . Fig. 2.9 shows an example of this process. The NRMSE between  $\xi(j)$  and  $\hat{\xi}(j)$  was then compared for the ESA denoising method and our proposed denoising method. The mean and standard deviation of NRMSE over all images are shown in Table 2.2. Using a one-tailed paired t-test, we found that our method had significantly lower NRMSE than the ESA method ( $p = 9.8 \times 10^{-11} < 0.05$ ).



(a) Ocean value selection process



(b) Corresponding linear regression for the ESA method (top) and our method (bottom) using the mean values selected from Fig. 2.9a.

Figure 2.9: Visualization of the quantitative experiment detailed in section 2.4.2

Table 2.2: Normalized root mean squared error for each image over selected ocean sub-images along with p-values generated from a one-tailed T-test comparing the proposed method to the others. The table is divided into comparing data from IPF 2.91 specific to sections 2.4.2 and 2.4.2, and 3+ that is specific to section 2.4.2

Method	IPF 2.91		IPF 3+	
	NRMSE	p-value	NRMSE	p-value
<i>ESA</i>	$1.85 \pm 0.941$	$9.8 \times 10^{-11}$	$0.685 \pm 0.278$	0.017
<i>Static <math>\bar{k}</math></i>	$0.814 \pm 0.674$	0.0058	N/A	N/A
<b>Proposed</b>	<b><math>0.568 \pm 0.274</math></b>	N/A	<b><math>0.592 \pm 0.295</math></b>	N/A

Ocean div.	Original	Unscaled (ESA)	Proposed
Arctic (73.5°N, 141.2°W)			
Arctic (73.6°N, 136.9°W)			
Antarctic (65.4°S, 138.7°W)			
Antarctic (71.8°S, 128.7°W)			
Atlantic (41.4°N, 28.5°W)			

Figure 2.10: Part 1 gallery of SAR images showing the effect of the baseline and the proposed noise removal methods in reference to the original image. Given coordinates correspond to the center of the image.



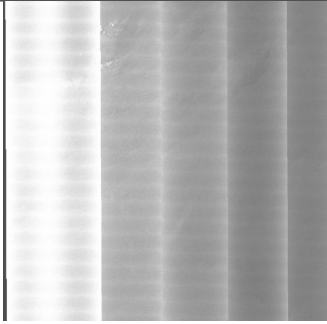
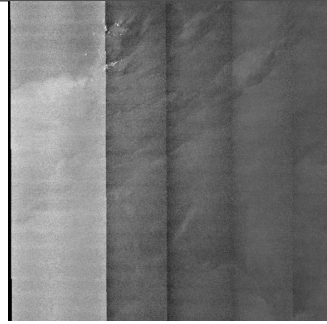
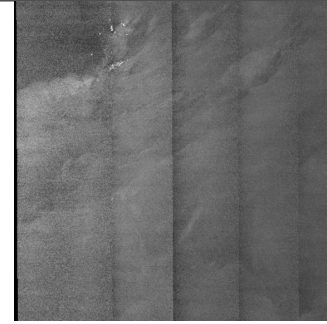
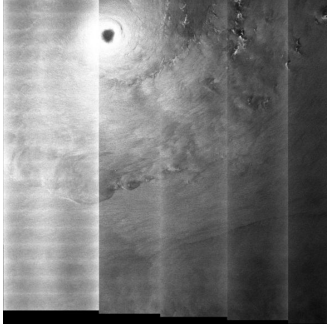
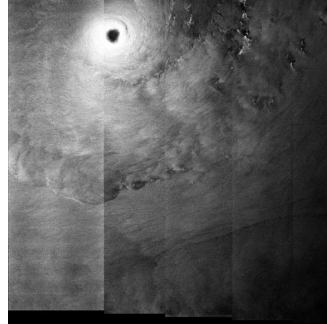
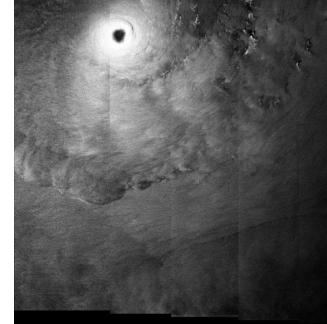
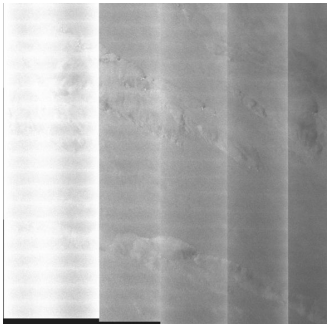
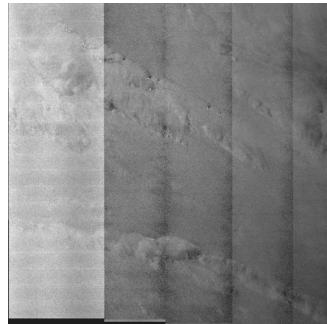
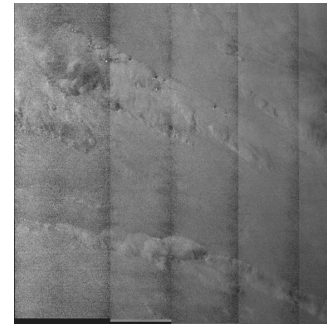
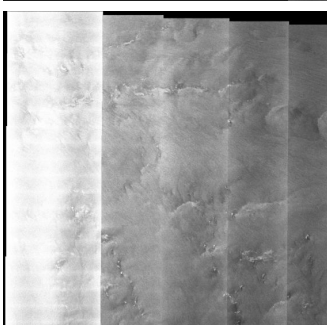
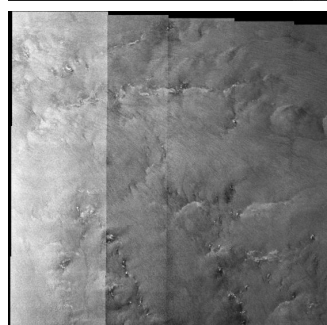
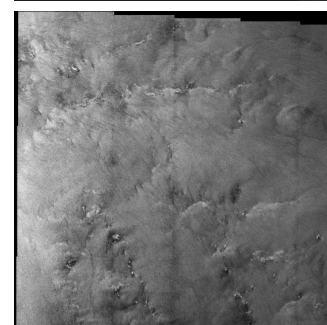
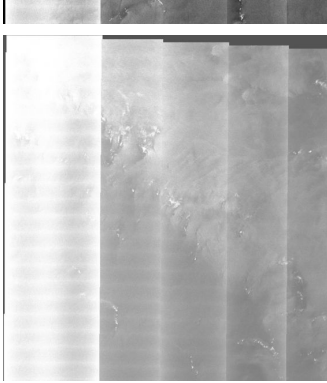
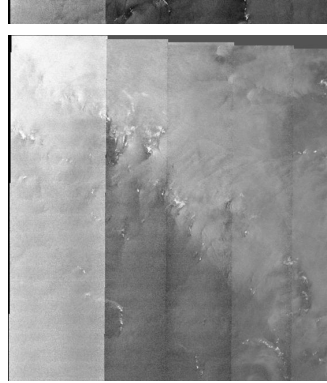
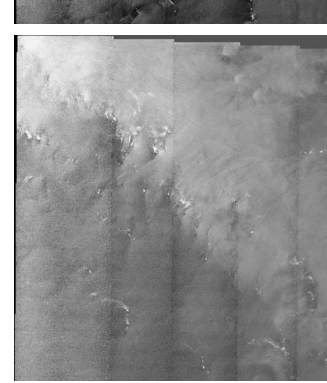
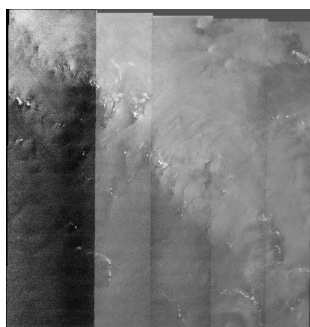
Ocean div.	Original	Unscaled (ESA)	Proposed
Atlantic (37.8°N, 26.8°W)			
Pacific (16.5°N, 150.9°E)			
Pacific (19.7°N, 174.7°W)			
Indian (21.1°S, 74.8°E)			
Indian (21.3°S, 76.9°E)			

Figure 2.11: Part 2 gallery of SAR images showing the effect of the baseline and the proposed noise removal methods in reference to the original image. Given coordinates correspond to the center of the image.

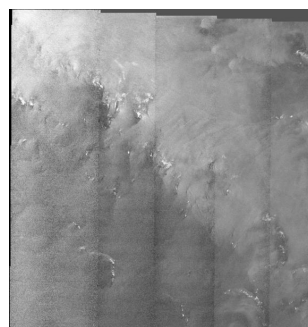


## Static versus dynamic analysis

While the overall effectiveness of the proposed method for denoising the SAR images has been demonstrated, there still remains the hypothesis that the ideal scaling parameters are different for each image. This hypothesis was tested by computing the aggregate mean values of  $\hat{\mathbf{k}}$  with the proposed method for HV ( $\bar{\mathbf{k}} = [1.438, 0.942, 0.980, 1.010, 0.999]$ ) and VH ( $\bar{\mathbf{k}} = [1.37, 0.932, 0.969, 0.993, 1.000]$ ) and comparing the effect of scaling the noise field with  $\bar{\mathbf{k}}$  versus scaling the noise field by dynamically estimating  $\hat{\mathbf{k}}$  for each image. Fig. 2.12 shows an example of how using a static estimate ( $\bar{\mathbf{k}}$ ) can provide sub-optimal denoising compared to using a dynamic estimate ( $\hat{\mathbf{k}}$ ).



(a) Static scaling



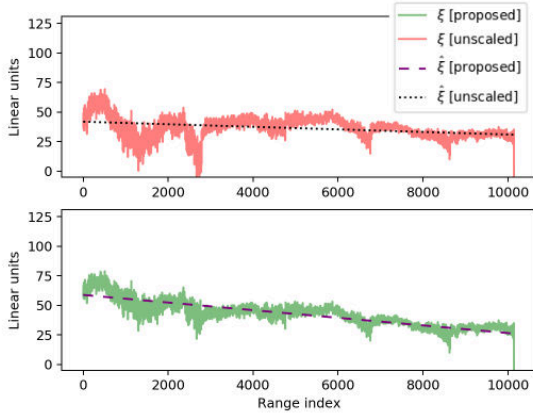
(b) Proposed dynamic scaling

Figure 2.12: An example of the importance of dynamically estimating scaling parameters for each image. In this case, the static scaling in this case overcompensates the true noise present in the image within the first swath.

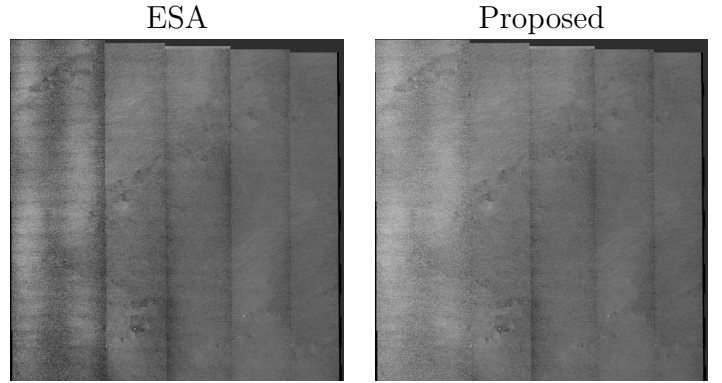
To test the significance of this effect, the same quantitative experiment in section 2.4.2, which compared the NRMSE of the linear regression with respect to the denoised measurement over ocean regions between two different methods, was applied. Namely, the mean estimates for  $\bar{\mathbf{k}}$  were applied to scale the noise field as the *static* method versus scaling with  $\hat{\mathbf{k}}$  using the **proposed** method. Overall, the **proposed** method had significantly lower NRMSE than the *static* ( $p = 5.8 \times 10^{-3} < 0.05$ ) from a one-tailed t-test, thus supporting our hypothesis that the ideal scaling factors are scene independent. Once again, these results are summarized in Table 2.2.

## IPF 3+

With the changes from IPF version 3+, the generation of noise fields changed significantly. A new normalization scheme was added to help account for situations where the signal to noise ratio is low [45]. To evaluate the effect of the proposed method on these new noise fields, we collected 13, 12, 8, 14, and 9 images from the Arctic, Antarctic, Atlantic, Pacific, and Indian oceans with sensing dates after July 2019. We repeated the quantitative experiment with this data, while skipping the *static* comparison for brevity. Table 2.2 indicate that the proposed method (NRMSE = 0.592) had significantly lower NRMSE than the ESA method (NRMSE = 0.685), with  $p = 0.017 < 0.05$ . As shown in Figure 2.13, the improvement between the proposed method and the ESA method is milder than with IPF 2.91.



(a) Range plot and linear regression for ESA method (top) and the proposed method(bottom)



(b) HV image results.

Figure 2.13: Brief comparison with IPF version 3+

## 2.5 Discussion

As mentioned in the introduction, the merit of the proposed method is based on achieving four objectives. The first three objectives are directly tied to the results of the two experiments, while the last objective is achieved from the formulation of the method itself.

The simulation experiment is based on the ideal scenario where our assumptions of actual additive noise are true; in other words, the noise field is linearly mis-scaled between

subswaths and the scaling is variable among different scenes. Under these circumstances, the proposed method provides an almost perfect denoising of the selection of Sentinel-2 scenes over coastal regions. In this scenario, the proposed method produced significantly better denoising than the scaling from using the static expected scaling parameters. This indicates that the proposed method can effectively adapt to the dynamic-scaling of the noise field in an ideal environment.

While the simulation experiment was a good demonstration that the proposed method works well in a controlled setting where the ground truth is known, obviously the characteristics of SAR and optical images are inherently different and the experiment on SAR images is required even if a ground truth reference is not known. Overall, the proposed method made dramatic improvements on the visual quality of the SAR images. The method was able to estimate parameters in a wide variety of backgrounds including those with heterogeneous textures, such as sea-ice or cyclones. Compared to subtracting an unscaled noise field, the proposed method suppresses the characteristics of the noise field to a much greater degree. Analytically, the evidence that the proposed method produces significantly lower NRMSE over the range of ocean regions concurs to the effectiveness of the proposed noise removal and the accomplishment of the first two objectives.

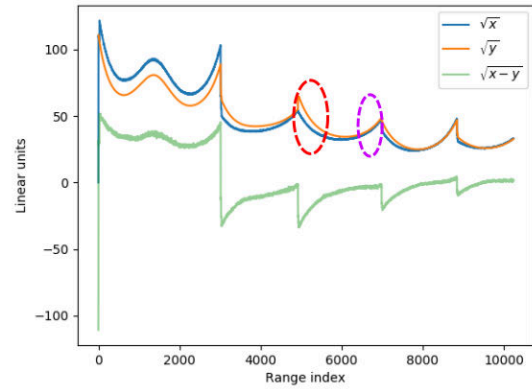
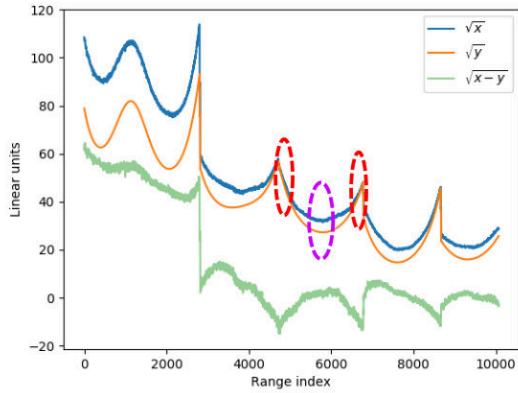
The experiment on the SAR images also revealed the impact of dynamically estimating scaling parameters. By using the mean parameters generated by the proposed method as the static scaling parameters, there are instances where the static parameters are unsuitable for the subswaths. This effect was significant in terms of NRMSE over range of ocean regions, indicating that there is a clear benefit for dynamic estimation.

Also of note is that the proposed method requires little computational overhead relative to the size of the noise field and image. The computational complexity of constructing the linear system is of the same order as a reduction along the azimuth, while solving the  $5 \times 5$  linear system of least-squares is trivial. The small size of the system is also beneficial because a closed form solution can be used and no expensive iterative algorithms like the conjugate gradient method, gradient descent, or grid search are required to estimate scaling parameters. The low overhead is another advantage of the dynamic parameter estimation aspect of the proposed method because the parameters can be quickly estimated for each image and, unlike a static estimation approach, requires no preparation in the sense of collecting a training set.

The introduction of IPF 3+ greatly improved the quality of the noise field. In section 2.4.2, it was demonstrated that the proposed method still provided some modest improvement, but the visual differences can be subtle. However, archived Sentinel-1 data is not updated with the newest IPF and are still susceptible to the mis-scale from IPF 2.91 and below. Therefore, our method provides a way for improving quality that can be

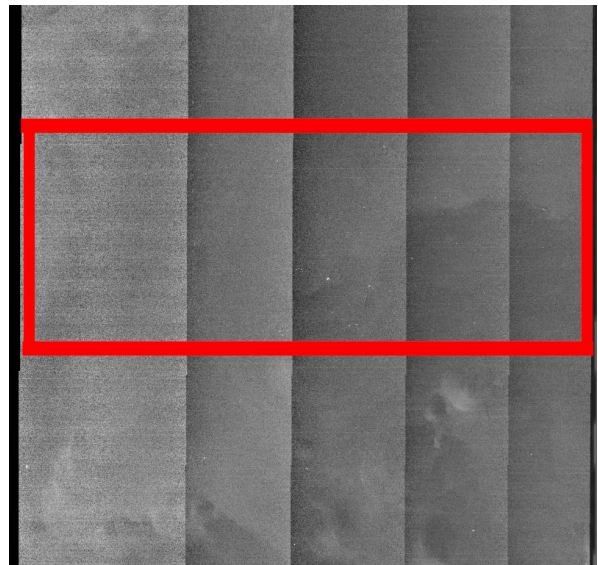
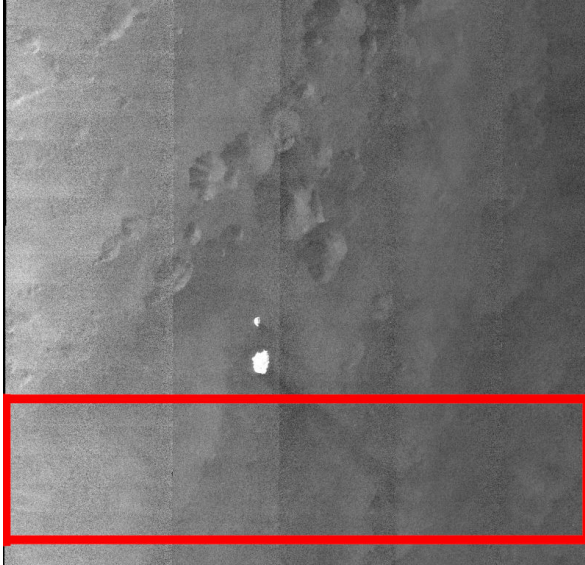
applied to both older and current Sentinel-1 data.

Despite the aforementioned success, some issues still exist in the SAR-images. As mentioned in [Section 2.4.2](#), some images have discontinuities between adjacent subswaths even after denoising. These issues do not seem to be from an incorrect estimation of scaling parameters. Rather, they seem to be caused from the shape of the ESA noise field not always fitting to the actual shape of noise imposed on the image, particularly in the range direction. An extreme example of this is shown in [Fig. 2.14a](#), where the left and right extremities of subswaths EW2, EW3, EW4, EW5 have a higher relative compensation than the centre of the swath. Another example in [Fig. 2.14b](#) shows a different style of misfit, where the left extremities of the subswaths have higher relative compensation compared to the right extremity. This shows that for some images, the provided noise fields are calibrated incorrectly in a more complex manner than linear scale. Consequently, this misfit accounts for errors in the noise removal that cannot be compensated by scaling individual subswaths alone. Correcting this will require correcting the shape of the noise curves either through enhanced calibration or by creating a more flexible empirical model to account for the shape of the curves. This is consequently an area of study for future work. While it would be interesting to adapt these methods to co-polarized images or images from Sentinel-1 modes such as IW, we suspect that the higher signal-to-noise ratios from these methods would make application of our methods to these types of images less necessary.



(a) ID: 20180930T081301\_20180930T081401\_023925\_029CB0  
The relative difference between the measurements and the noise is greater in the centre of subswaths (purple) than the right and left extremities (red) within the same subswath.

(b) ID: 20190322T212224\_20190322T212324\_015472\_01CFB5:  
The relative difference between the noise and signal is different for the right (red) and left extremities (purple) within the same subswath.



(c) ID: 20180930T081301\_20180930T081401\_023925\_029CB0:  
Input image with evaluation range highlighted in red.

(d) ID: 20190322T212224\_20190322T212324\_015472\_01CFB5:  
Input image with evaluation range highlighted in red.

Figure 2.14: Mean signal and noise with respect to range over an ocean sub-region. In both examples the noise is not fit properly for subswaths EW2, EW3, EW4, and EW5.

## 2.6 Conclusion

We created a quadratic objective function to model the characteristics of the estimated noise field in TOPSAR cross-polarized images. Our method uses this objective function to estimate scaling parameters for each of the subswaths in a scene. The method compared favourably to unscaled noise removal in both a simulation experiment on non-SAR images on an experiment selection of Sentinel-1 cross polarized TOPSAR images over major ocean-divisions around the world. These experiments showed that the algorithm works on a variety of backgrounds, has no requirements of acquiring a training data set, provides dynamic scaling parameter estimation for each image, and has low computational requirements. These merits are beneficial for any practitioner who uses cross-polarized Sentinel-1 EW images, as the algorithm can be conveniently applied with little preparation required.

## Conflict of Interest

Declarations of Interest: None

## Acknowledgments

We acknowledge the support of the Natural Sciences and Engineering Research Council of Canada (NSERC). We also acknowledge funding from the University of Waterloo.

Thanks are also extended to Prof. K. Andrea Scott, Mohsen Ghanbari, and Mingzhe Jiang for their feedback on the manuscript.

## Appendix: Inner Product Formulations

**Claim.**  $L^\sim \in \{L^A, L^B, L^R\}$  can be represented with an arbitrary inner product formulation  $[\mathbf{v}^\sim - \mathbf{C}^\sim \hat{\mathbf{k}}]^\top [\mathbf{v}^\sim - \mathbf{C}^\sim \hat{\mathbf{k}}]$ , using some vector  $\mathbf{v}^\sim$  and matrix  $\mathbf{C}^\sim$ .

*Proof.* First, discard the connotations associated with the variables  $i$ ,  $j$ , and  $n$  in the main text. Without loss of generality, let  $L^\sim = \sum_{i=1}^N [w(i) [\hat{\phi}_{a(2i-1)}^{2i-1} - \hat{\phi}_{a(2i)}^{2i}]]^2$  given the linear denoising model  $\hat{\phi}_{a(j)}^j = x_{a(j)}^j - \hat{k}_{a(j)} y_{a(j)}^j$ , with  $x_{a(j)}^j$  representing a selection of the measurement,

$y_{a(j)}^j$  representing a selection of the estimated noise, and a subswath  $a(j) \in \mathcal{A}$ . Then for any  $i$ ,

$$\begin{aligned} w(i)[\hat{\phi}_{a(2i-1)}^{2i-1} - \hat{\phi}_{a(2i)}^{2i}] &= w(i)[x_{a(2i-1)}^{2i-1} - \hat{k}_{a(2i-1)}y_{a(2i-1)}^{2i-1}] - [y_{a(2i)}^{2i} - \hat{k}_{a(2i)}y_{a(2i)}^{2i}] \\ &= w(i)[x_{a(2i-1)}^{2i-1} - x_{a(2i)}^{2i} - [\hat{k}_{a(2i-1)}y_{a(2i-1)}^{2i-1} - \hat{k}_{a(2i)}y_{a(2i)}^{2i}]]. \end{aligned} \quad (2.22)$$

We can encode (2.22) for all  $i$  into a vector  $\mathbf{v}^\sim - \mathbf{C}^\sim \hat{\mathbf{k}}$  where  $\mathbf{v}^\sim$  contains the terms with  $x$  and  $\mathbf{C}^\sim$  contains the terms with  $y$ . More precisely,

$$\mathbf{v}^\sim \in \mathbb{R}^N = \begin{bmatrix} w(1)[x_{a(1)}^1 - x_{a(2)}^2] \\ \vdots \\ w(i)[x_{a(2i-1)}^{2i-1} - x_{a(2i)}^{2i}] \\ \vdots \\ w(N)[x_{a(2N-1)}^{2N-1} - x_{a(2N)}^{2N}] \end{bmatrix} \quad (2.23)$$

and

$$\mathbf{C}^\sim(i, n) = \begin{cases} w(i)[y_{a(2i-1)}^{2i-1} - y_{a(2i)}^{2i}] & \text{if } a(2i-1) = a(2i) = n \\ w(i)y_{a(2i-1)}^{2i-1} & \text{if } a(2i-1) = n \text{ and } a(2i) \neq n \\ -w(i)y_{a(2i)}^{2i} & \text{if } a(2i) = n \text{ and } a(2i-1) \neq n \\ 0 & \text{otherwise} \end{cases}, \quad (2.24)$$

with the index  $n$  representing the different subswaths  $\in \mathcal{A}$  and  $\mathbf{C}^\sim \in \mathbb{R}^{N \times 5}$ . Then by the rules of matrix multiplication

$$\sum_{i=1}^N [w(i)[\hat{\phi}_{a(2i-1)}^{2i-1} - \hat{\phi}_{a(2i)}^{2i}]]^2 = [\mathbf{v}^\sim - \mathbf{C}^\sim \hat{\mathbf{k}}]^\top [\mathbf{v}^\sim - \mathbf{C}^\sim \hat{\mathbf{k}}] \quad (2.25)$$

□

## Chapter 3

# Estimating Noise Floor in Sentinel-1 Images with Linear Programming and Least Squares

The following article is slated to be submitted to IEEE Transactions in Geoscience and Remote Sensing and modifications may be made after submission of this thesis. I completed this work by myself under supervision from my supervisors Linlin Xu and David Clausi. This article documents a method of estimating a best fitting noise floor for EW and IW Sentinel-1 images with the goal of compensating for an issue presented in Chapter 2, where the standard noise floor was mis-fit in manner that could not be compensated through linear scaling. The method models the noise floor to be a power function of the antenna radiation pattern power plus a correction offset for each subswath. The power function parameters are estimated by solving linear programming problems while the offsets are estimated by solving a least squares problem. Overall, the method matched the characteristics of the true noise floor better than both the default noise floor estimates provided by the ESA and linear transformations of the estimates.



# Estimating Noise Floor in Sentinel-1 Images with Linear Programming and Least Squares

Peter Q. Lee, Linlin Xu, and David A. Clausi

## Abstract

Sentinel-1 is a synthetic aperture radar platform that provides free and open source images of the Earth. A product type of Sentinel-1 is Ground Range Detected (GRD), which records intensity while discarding phase information from the radar backscatter. Especially in cross-polarized GRD images, there are noticeable intensity changes throughout the image that are caused by amplifying the noise floor of the signal, which varies due to non-uniform radiation pattern of the satellite’s antenna. While Sentinel-1 has Instrument Processing Facility (IPF) software to estimate the noise floor, even in the newer versions (3.1 or above) of the IPF software there are still instances where the estimates provided do not fit to the actual noise floor in the image, which is particularly noticeable in transitions between adjacent subswaths.

In this work we propose a method that reduces the impact of the varying noise-floor throughout the image. The method models the intensity of the noise floor to be a power function of the radiation pattern power. The method divides the swath into several sections depending on the location of the local minimum and maximum of the radiation pattern power with respect to the range. The parameter estimation is portrayed as a geometric programming problem that is transformed into a linear programming problem by logarithmic transformation. Affine offsets are computed for each subswath by a weighted least squares approach.

We evaluate our method on extra wide (EW) and interferometric wide (IW) Sentinel-1 modes with a series of three experiments. The first experiment simulates adding and removing the proposed noise floor model on a sample of RADARSAT-2 images, which is quantitatively evaluated with standard image quality metrics. The second experiment evaluates the effect on relevant Sentinel-1 images, which is quantitatively gauged by the appearance of open-water regions. The third experiment evaluates the change in radiometric bias compared to the baseline noise floor estimates. The first two experiments show that the proposed method is successful in fitting to the shape of the true noise floor in the images. The third experiment indicates that there is a significant change in radiometric bias

compared to the baseline estimates, indicating that one must be mindful for applications that are calibrated to the baseline estimates.

## 3.1 Introduction

Synthetic aperture radar (SAR) is a method of remote sensing that uses backscatter from emitted radar pulses to infer physical characteristics about the surface. Sentinel-1 is a mission by the European Space Agency (ESA) that uses two satellites (Sentinel-1A and Sentinel-1B) to provide a free and open source of SAR images of the planet. Consequently, Sentinel-1 remains an important resource for remote sensing practitioners.

One issue that is apparent in unprocessed images are the noisy intensity patterns that disrupt the appearance of the desired backscatter intensity, which are sometimes described as additive noise, noise equivalent sigma zero, or as scalloping and banding patterns. Throughout this paper these noise patterns will be described as the noise floor of the image, which is the total sum of noise sources within a signal measurement. Throughout its lifespan, Sentinel-1 has had multiple iterations of its Instrument Processing Facility (IPF) software, which provides a method of estimating and subtracting the noise floor from the image in order to normalize the intensity within the image. In IPF 2.9, azimuth vectors were added to compensate for the scalloping patterns that occur along the azimuth [10]. In IPF 3.1 further improvements were made to improve the consistency of the noise floor among different subswaths [10]. In early versions of the IPF, remote sensing practitioners had difficulty compensating for the varying noise floor, particularly in cross-polarized images [22, 27, 39, 50]. While more recent versions have improved this, issues still remain. The recent article by [48] evaluated the calibration of Sentinel-1 images finding that calibration can suffer particularly in scenarios with lower backscatter. In addition to radiometric differences between the two satellites, it was also found that the look angle was a factor for discrepancies in intensity.

The types of images most affected by the noise floor issue are cross-polarized images over maritime regions, due to the low backscatter of ice and water. Consequently, noise floor removal is critical for applications that require uniform and consistent measurements throughout the image. One such application is sea ice analysis, where the backscatter is used to determine the physical qualities of the ice [22, 50]. Wind speed analysis also rely on cross-polarized images, with the literature showing that wind speed algorithms are adversely affected by the noise floor patterns in Sentinel-1 images [18, 35]. Therefore, ensuring homogeneous intensity throughout cross-polarized images could greatly improve visual interpretation and the performance of the models applied for these tasks.

There are a limited number of methods in the literature that attempt to compensate for the noise floor in Sentinel-1 images. In the work by [39], a methodology was proposed that rescales the default ESA noise floor in an affine manner for each subswath. Previous work [30] built onto this method by formulating a way to dynamically estimate parameters of the noise floor specific to each image. Specifically, a least-squares approach was used to estimate linear scaling parameters for each of the different subswaths such that applying this re-scaled noise floor results in a more consistent intensity profile throughout the image. However, as noted [30], the noise floor is sometimes mis-fit in a non-linear manner that makes it impossible to choose a linear scaling parameter that satisfies all sections within a subswath.

In this work, we attempt to compensate for this non-linear mis-fit of the noise floor in the subswaths. We observe that the radiation pattern of the platform matches the scale of the true noise floor much better than the ESA noise floor. We propose a novel model of the noise floor to be a power function of the platform’s radiation pattern, whose parameters are estimated by solving a geometric program, that is converted to a linear program in the log transformed domain. To ensure compatibility between adjacent subswaths, offsets for each subswath are computed using a weighted least squares formula to compensate for the gamma distribution of backscatter.

We evaluate our method with three experiments. The first experiment evaluates the performance of the proposed method within a simulated experiment on a selection of RADARSAT-2 images. The second experiment evaluates the method on a selection of Sentinel-1 images in both EW and IW mode, whose quantitative performance is determined based on the characteristics of open-water in the images. The third experiment determines the difference in radiometric bias compared to the default ESA method. Overall, the first two experiments showed that the proposed method is able to substantially improve the image quality under different conditions, particularly in its ability to correct for the non-linear misfit in the images. The third experiment indicated that the proposed method results in a different radiometric bias than the baseline ESA method. However, it is unclear whether the radiometric bias change is an error, as there are some examples where the ESA method loses significant features in images. Therefore, we recommend further studies comparing known materials to the backscatter for calibration purposes.

## 3.2 Background

To understand the problem of estimating the noise floor, we first provide an abridged overview of how the Sentinel-1 SAR platform operates in GRD mode, which records

backscatter intensity and discards phase information. For a complete description, see [43]. The satellites emit radar pulses towards the surface of the planet and measure the varying intensity of backscatter to construct images. The backscatter intensity depends on factors such as surface composition, incidence angle, and antenna radiation power. Ideally, if an isotropic antenna were used, the antenna’s radiation power ( $P$ ) would be identical in all relevant directions and thus would eliminate this variable for backscatter intensity. However, due to the limits of manufacturing, the radiation pattern of Sentinel-1 antennas are non-isotropic and vary depending on the look angle. To compensate for the varying radiation pattern, the measured signals must be amplified differently according to the look angle to ensure that the backscatter measurements are comparable throughout the image. An impact of this amplification is that the thermal noise floor, which is the lowest possible measured signal caused by the sum of noise sources (e.g. within the circuitry of the satellite) [24], is amplified differently according to look angle as well. This results in non-stationary noise floor patterns throughout the images because regions that are acquired with lower radiation power have an amplified noise floor with higher intensity and regions that are acquired with higher radiation power have an amplified noise floor with lower intensity. In Sentinel-1 this has been called additive noise or noise equivalent sigma zero (NESZ) and is commonly associated with banding and scalloping patterns [53, 55].

The two Sentinel-1 modes this paper considers are extra wide (EW) and interferometric wide (IW) modes, which have the option to produce GRD types of images. These sensor modes use Terrain Observation with Progressive Scans SAR (TOPSAR) to scan surface area in a compromise between resolution and surface area covered [59]. TOPSAR works by breaking an area into different so called subswaths along the range. During orbit, it measures all subswaths concurrently by sequentially emitting bursts rotated towards different elevation angles that correspond to the different subswaths. Due to the design of the antenna, the radiation pattern is unique for each subswath. EW mode has five subswaths and is typically applied to ocean regions with its first subswath, EW1, having a very high magnitude noise floor with a multimodal pattern, while the remaining 4 subswaths, EW2, EW3, EW4, and EW5 have U-shaped patterns. IW mode has three subswaths, IW1, IW2, and IW3, all of which have U-shaped patterns. For both of these sensor modes, the later subswaths will typically be created with higher radiation power than the earlier subswaths. The unprocessed images have significant changes of intensity due to the varying noise floor. The changes are particularly abrupt at boundaries between subswaths, since the radiation patterns used are discontinuous due to the subswath merging. Fig. 3.1 shows examples and the relationship between the estimated noise floor and the antenna radiation power.

The ESA provides noise-calibration XML files that estimate the noise floor, so that subtracting the original image and the noise floor will result in a more consistent intensity

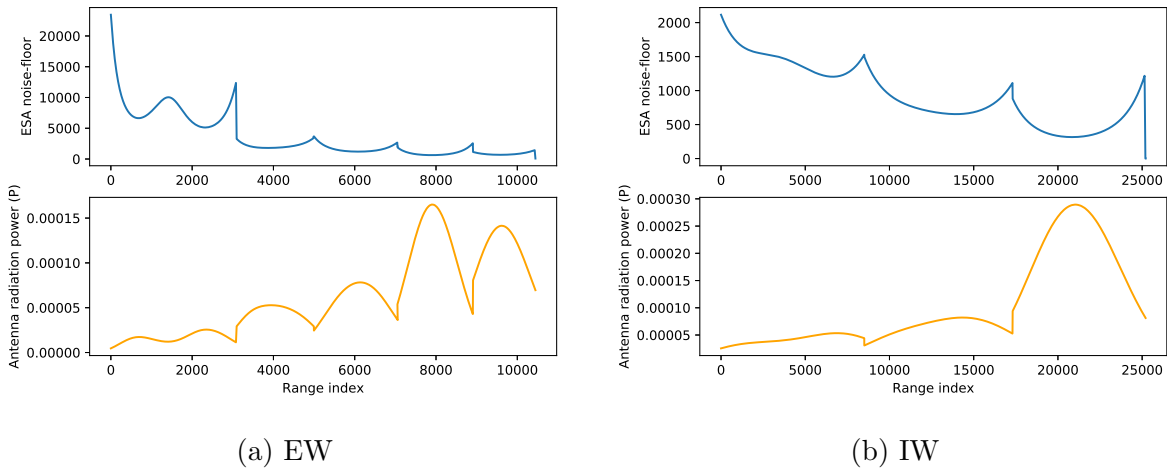
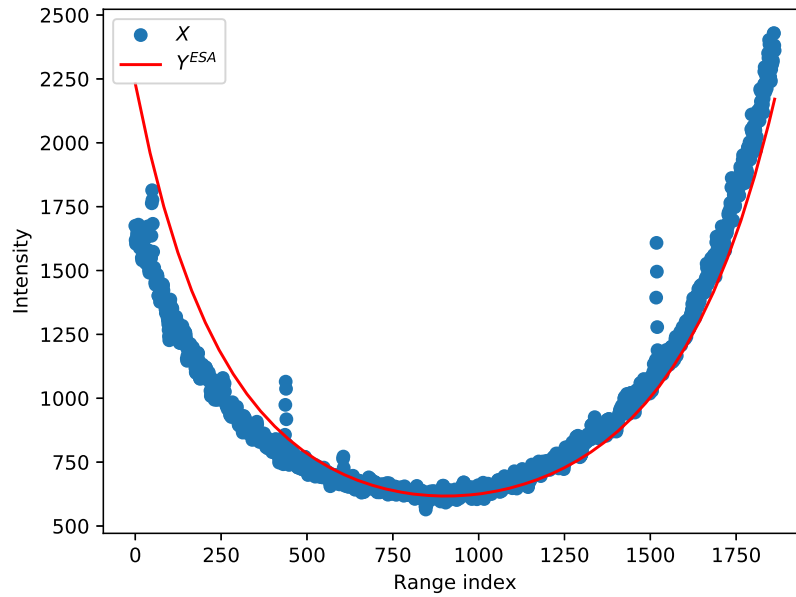


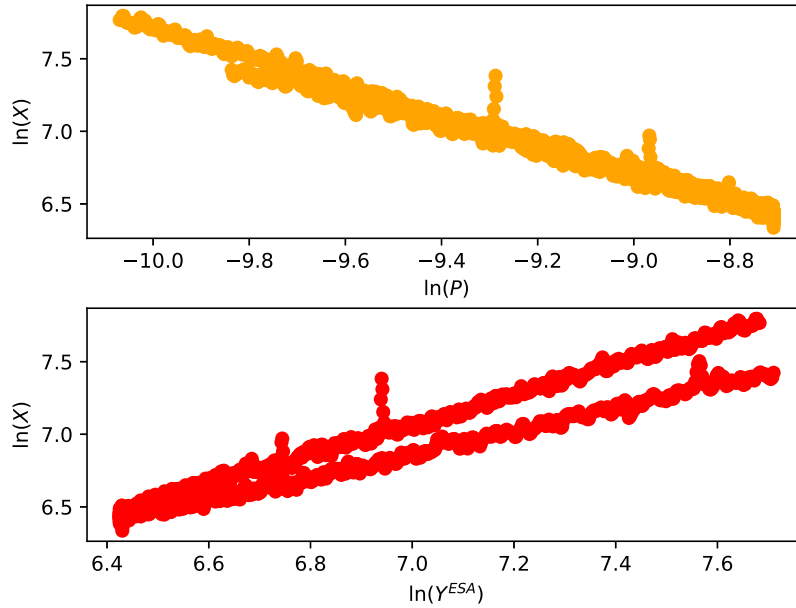
Figure 3.1: Plots of the estimated noise floor (top) and the antenna radiation pattern power (bottom) along the range direction for both EW and IW images (unit-less). Their values show an inverse relationship. Both the ESA noise floor and antenna radiation power values were derived from XML files from the Sentinel-1 products.

profile throughout the image. However, as shown in previous work [30], these estimations have issues fitting to the images. While linear rescaling methods improve on this [30, 39], a critical issue that remains is that there is non-linear mis-scaling within each subswath [30]. For instance, Fig. 3.2a shows an example where the ESA noise floor is clearly mis-fit in a subswath. Linear rescaling will not fix this because one side of the subswath is under-compensated, while the other is over-compensated.

The main observation that motivates our work is that the antenna pattern fits the actual noise floor better than that provided by the ESA. In Fig. 3.2b, it can be seen that on a log-log plot the antenna pattern matches the intensity measured over open-water more consistently. The linear trend motivates the modelling of the noise floor as a power function of the antenna radiation power.



(a) Figure shows clear mis-fit between the estimated noise floor and the measurement over open water, a material that has low backscatter in cross-pol and therefore a good estimate of the true noise floor. Note that the left side of the subswath is over-compensated, while the right side is not. This implies that there is no choice of linear scale will rescale the noise floor correctly because one side of the subswath will always remain over- or under-compensated.



(b) Figure showing a log-log plot comparing measurement intensity ( $\ln(X)$ ) to the antenna pattern power ( $\ln(P)$ ) and the ESA noise floor ( $\ln(Y^{ESA})$ ) respectively. Notice that non-linear mis-fit of the ESA noise floor shown in 3.2a is reflected by the radically different slopes in the log domain. While the antenna pattern power graph also has two different slopes, their difference is less severe and therefore better fit.

Figure 3.2: Non-linear mis-fit in a homogeneous section of EW4.

### 3.3 Methods

Given our observations above, we wish to model noise floor as a power function of the antenna radiation pattern

$$Y = e^b P^m + o, \tag{3.1}$$

where  $Y$  is the estimated noise floor,  $P$  is the power of the antenna radiation pattern, and  $m$ ,  $b$ , and  $o$  are parameters that need to be estimated using the available data, from  $P$  and measurements  $X$ , in each scene. These parameters serve different purposes. The power function parameters,  $m$  and  $b$ , are used to adapt to the overall shape of the noise-floor within different sections of the subswath. The offset parameter,  $o$ , is used to correct for affine bias that may occur between the subswaths. Values for  $P$  are derived from the *antennaPattern* fields in the XML files that come with Sentinel-1 products, using the *geoLocationGrid* lookup tables to convert elevation angles to range coordinates. Critically, the unit-less values from *antennaPattern* were divided by an arbitrarily large number that was greater than all pattern measurements (we chose  $e^{43.3}$ ) for numerical stability purposes. The measurements,  $X$ , are taken from the image files in the product, with pixel values squared to convert to intensity. [The model (3.1) differs significantly from other works because it generates the shape of the noise floor from the antenna pattern itself and it is a non-linear model.

As will be described in further detail below, the power function parameters,  $m$  and  $b$ , and the offset parameter,  $o$ , are estimated in two different steps. Parameters  $m$  and  $b$  are estimated in context of a geometric programming problem that is converted to a linear program. The parameters  $m$  and  $b$  are estimated differently depending on the subswath,  $a$ , and the division of the subswath along the range,  $s$ , that is based on where the local minimum or maximum lies in  $P$ . The parameter  $o$  is estimated through a weighted least-squares approach, with its objective being the reduction of intensity between adjacent subswaths. This offset  $o$  is estimated on a per subswath basis. The parameters of each power function are estimated by aggregating the values of measurements ( $X$ ) and the radiation power ( $P$ ) over all bursts ( $g \in a$ ) within each range split ( $s \in a$ ). The bursts in TOPSAR correspond to sections along the azimuth that are captured within a radar pulse. In the unprocessed images the bursts are demarcated by a scalloping pattern along the azimuth because the satellite's antenna pattern also varies along the azimuth, albeit with less magnitude than the range. A visual layout of the location of the subswaths ( $a$ ), range splits ( $s$ ), and bursts ( $g$ ), along with the location of relevant parameters can be found in Fig. 3.3. A summary of the entire algorithm is given in Algorithm 1.

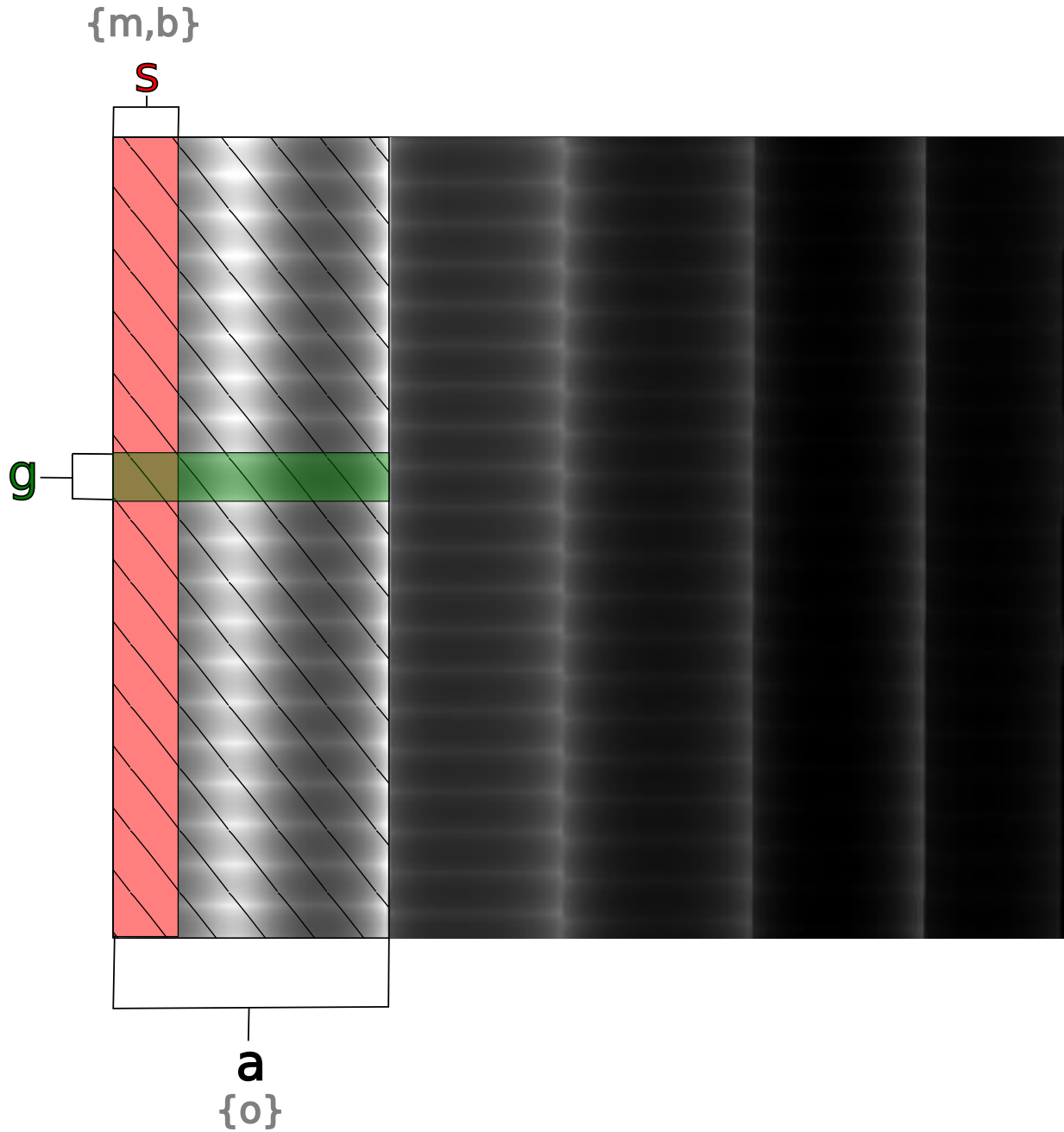


Figure 3.3: Sections of an EW image divided by subswath,  $a$  (hatched), bursts,  $g$  (green), and range divisions,  $s$  (light red). The parameter  $o$  is different for each subswath and the parameters  $m$  and  $b$  are different for each range split, as labelled in gray braces.



---

**Algorithm 1:** Main procedure for noise floor estimation and subtraction in SAR image.

---

```

1 for each subswath  $a \in \mathcal{A}$  do
2   for each split  $s \in a$  do
3     Construct  $\mathcal{G}_{a,s}$  by Algorithm 2 // Get data points for lin. prog.
4     Compute parameters  $m, b$  by solving (3.4) // Solve lin. prog.
    /* With the base parameters solved, smooth out the function between
    /* range splits with linear interpolation for each subswath.
5   for each split  $s \in a$  do
6     Determine parameter values between the adjacent range split using
    Algorithm 3;
7     Compute  $\tilde{X}$  within  $a$  and  $s$  by computing (3.5) // Compute the partial
    denoised result
8 Compute  $\mathbf{o}$  by solving (3.6);
9 Compute noise floor (3.1) and denoise by computing  $X - Y$ ;

```

---

### 3.3.1 Power function

The idea behind estimating the parameters of the power function is that the model should act as a tight lower bound on the measurements ( $X$ ). To this end, the problem is shaped into the following geometric program

$$\begin{aligned} & \max_{m,b} e^b \Gamma^m(P, X) \\ & \text{such that } e^b P_i^m \leq X_i, \end{aligned} \tag{3.2}$$

with the assumption that  $P$  and  $X$  vary along the range, with  $P_i$  and  $X_i$  being observed pairs of radiation power and measurement points from the data. The intuition behind using constrained optimization to estimate the parameters is that the noise floor has the fundamental property of being the minimum measurable signal. Constrained optimization offers a way to find a lower bound of the noise floor function based on the observed measurements. To this end, the inequality constraints ensure that the parameters  $m, b$  that are estimated result in (3.1) being a lower bound of the measurements ( $X$ ). From a typical optimization perspective, the objective function may seem unusual, as one would typically attempt to choose  $m, b$  to minimize the distance between measured points and the power function. However, in our case we want to specify tightness to the lower bound

of points; minimizing the difference between points would be counter productive because the backscatter intensity interfere with this estimation. Therefore, the objective function  $e^b \Gamma^m(P, X)$  is used to maximize the position along a moment of the curve, and allowing the inequality constraints to bound it underneath the measurements. The scalar  $\Gamma(P, X)$  is chosen to utilize all available pairs of points ( $P$  and  $X$ ) to arrive at an appropriate moment, which we abstain from defining until we convert (3.2) into a linear program.

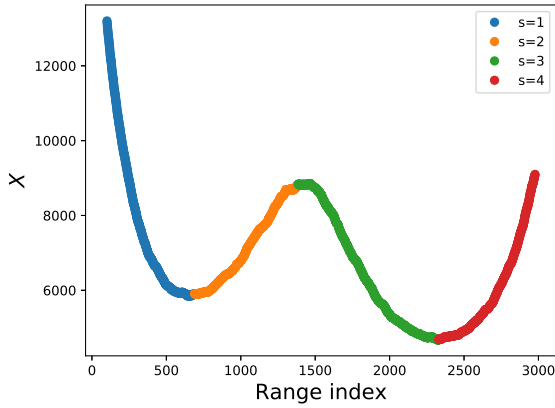
The approach of applying log transformations to geometric programs is a prominent strategy in geometric programming in order to make original problem easier to solve [14]. The special case of the power function is convenient as it transforms directly to a linear function

$$\ln(e^b P^m) \equiv m \ln(P) + b \equiv mp + b. \quad (3.3)$$

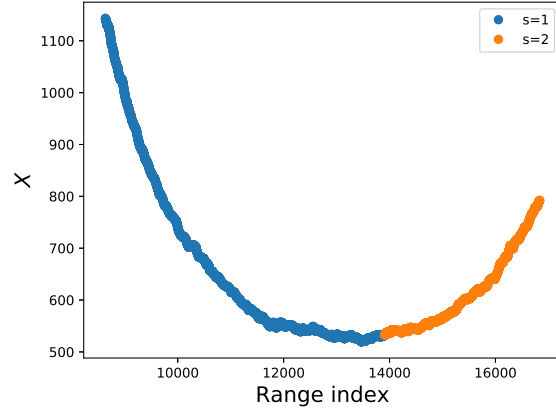
Given our observations in Section 3.2 pertaining to the linearity of the true noise floor in the log-log domain, it is logical to transform the objective function to be a linear function. Optimizing parameters of a linear objective function with respect to a set of linear inequalities is the definition of a linear program [9]. This is convenient as linear programs are a well known class of problems with many applicable algorithms available for use.

Returning the topic of the linearity of true log noise floor, one may wonder why the typical least squares regression for computing lines of best fit is not used. As we expect the noise floor to be the lower bound of intensity values, we require a line that fits to the lower extremity of the points, rather than where the points lay on average. Therefore least squares regression would not estimate a lower bound that is required in order to be an estimated noise floor.

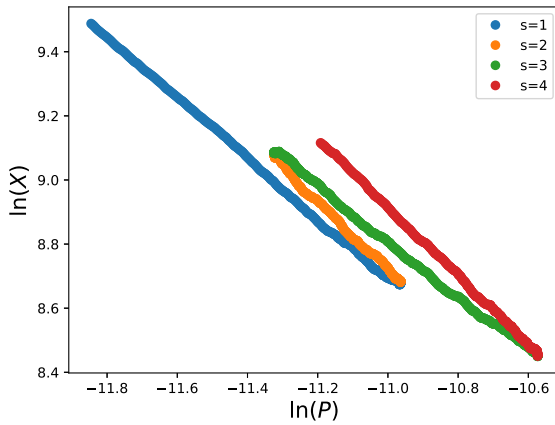
We aim to model several different functions contingent to the different subswaths ( $a$ ) and range splits ( $s$ ) discussed above. We observe that on open-water regions the linear trend changes slope at different range sections of the subswath, which we call range splits. These changes appear at local minimum and maximum of the radiation pattern power. An example of this is shown in Fig. 3.4. Therefore, separate power functions are modelled for every range split  $s$  in each subswath  $a$ .



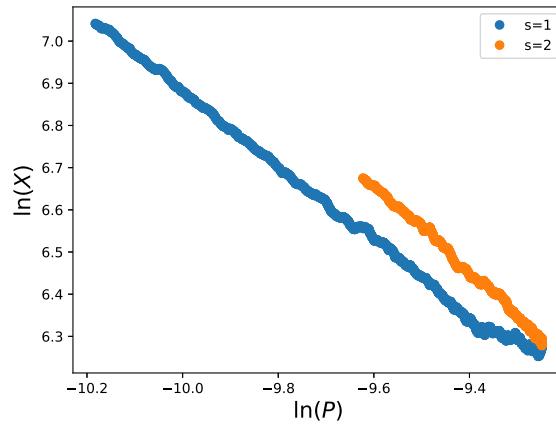
(a) Real domain: Subswath EW1



(b) Real domain: Subswath IW2



(c) Log domain: Subswath EW1



(d) Log domain: Subswath IW2

Figure 3.4: Top figures show the range splits, based on the local-minima and local-maxima of the antenna pattern, corresponding to measurements in the real domain. Bottom plots show log-log graphs of the antenna pattern versus the measured intensity. The range splits are divided in terms of colour, clearly showing that there is a linear trend that changes each time a local min/local max is passed.

The aim for the parameter estimation problem is to tightly fit the power function to the true noise floor as it varies along the range. To use the measurements for parameter estimation, several preprocessing steps are needed. As we aim to model separate power functions for every range split  $s$ , we require a method to obtain potential points of the true

noise floor throughout  $s$  from which to estimate the power function parameters. We denote this set of points as  $G_{a,s}$ , by extracting pairs of log transformed antenna pattern values and measurements  $(p_i, x_i)$  over all bursts within  $a$  and  $s$ . The overall process of constructing  $G_{a,s}$  is given in Algorithm 2. The method involves extracting indices that cover the overlap between burst  $g$  and slice  $s \in a$ , and gathering the average measurements along the range. Further processing is done in the form of convolution with a boxcar filter of size 51 (to remove outliers). The minimum value produced by the ESA noise floor removal method within each burst is subtracted so that bursts with higher backscatter can still contribute to the lower bound that is used to shape the parameter estimation.

---

**Algorithm 2:** Construct  $G_{a,s}$

---

```

1 Let  $G_{a,s} = \{\}$ ;
2 Let  $B$  be the baseline noise floor from the ESA method;
3 for each burst  $g \in a$  do
4   Let  $z$  be the range and azimuth indices in  $g \cap s$ ;
5   Let  $\kappa$  be the range indices in  $g \cap s$ ;
6   Let  $\bar{\mathbf{X}} = \text{mean reduction of } X(z) \text{ along azimuth axis; // reduce to 1D array}$ 
   along range
7   Let  $\mathbf{ESA} = \text{mean reduction of } X(z) - B(z) \text{ along azimuth axis; // Get}$ 
   equivalent signal computed by the ESA method
8   Let  $\mathbf{T} = \bar{\mathbf{X}} * \text{boxcar}(51)$ ; // Smooth array with low pass filter
9   Let  $\mathbf{Q} = \mathbf{T} - \min(\mathbf{ESA})$ ; // Subtract the minimum ESA value, so that Q
   is closer to the true noise floor
10  Update  $G_{a,s} \implies G_{a,s} \cup (\ln(\mathbf{Q}), \mathbf{P}(\kappa))$ ; // Concatenate points

```

---

The linear program takes the form of

$$\begin{aligned}
& \max_{m,b} \gamma m + b \\
& \text{such that } mp_i + b \leq x_i \quad \forall (x_i, p_i) \in \mathcal{G}_{a,s}, \\
& m \leq -0.75, \text{ and } m \geq -1.25,
\end{aligned} \tag{3.4}$$

where  $m$  and  $b$  are optimization parameters,  $(x_i, p_i)$  are pairs of points obtained by Algorithm 2, and  $\gamma$  is the objective variable. Again, note that different versions of  $m$ ,  $b$ , and  $\gamma$  are created for every pair of subswath  $a$  and split  $s$ , but are not annotated differently in the formulas for visual clarity. As mentioned previously, by estimating parameters  $m$  and  $b$  in a linear function  $mp + b$  in log space is equivalent to  $e^b P^m$ , which is part of the proposed model of the noise floor.

Because the noise floor is the lower bound signal, linear constraints  $mp_i + b \leq x_i$  are set, indicating that the noise floor estimate cannot exceed the signal measurements. We also found it beneficial to add additional inequalities  $m \leq -0.75$  and  $m \geq -1.25$ , since occasionally the program would result in extreme slope values that were inappropriate.

The objective  $\gamma m + b$  is designed to promote a line that is close to the constraining points as possible. If one ignores the  $m \leq -0.75$  and  $m \geq -1.25$  constraints, mathematically the choice of  $\gamma$  must be between  $\min(\mathbf{p})$  and  $\max(\mathbf{p})$  or else the linear program would be unbounded and no feasible solution exists (see proof in appendix). More intuitively,  $\gamma$  could be thought of the factor controlling where the line should be most tight to the constraining points. For example, if  $\gamma$  is chosen as  $\max(\mathbf{p})$  then the resulting line will be tight for points close to  $\max(\mathbf{p})$ , but looser for points close to  $\min(\mathbf{p})$ , and vice versa. Thus, a choice of  $\gamma$  should be chosen so that the resulting line is suitable for as many points as possible. While a naïve choice of  $\gamma$  would be the mid point of  $\{p_i \in \mathcal{G}_{a,s}\}$ , this would cause a bias towards lower values due to the logarithmic transformation. To account for this, an unbiased value of  $\gamma$  is determined by selecting the associated points  $\{(x_{\min(p)}, \min(p)), (x_{\max(p)}, \max(p))\} \in G_{a,s}$  in order to compute the midpoint  $v = \ln\left(\frac{\exp(x_{\min(p)}) + \exp(x_{\max(p)})}{2}\right)$ . The percentage scaling is put back into the log scale as  $\alpha = \frac{v - x_{\min(p)}}{x_{\max(p)} - x_{\min(p)}}$ . Finally,  $\gamma = \max(p) - \alpha(\max(p) - \min(p))$ .

Since (3.4) and all its requisite terms have been determined, there are no further major steps for estimation, as the desired parameters  $m$  and  $b$  can be easily determined by using off-the-shelf solvers. We implemented the problem by using the cvxpy library[4, 13] with the splitting conic solver [37, 38] to solve for the parameters. This process is repeated for each division of subswaths independently. For reference, Fig. 3.5 shows an example of the bounding line estimated from (3.4) aggregated over a series of non-homogeneous series of bursts.

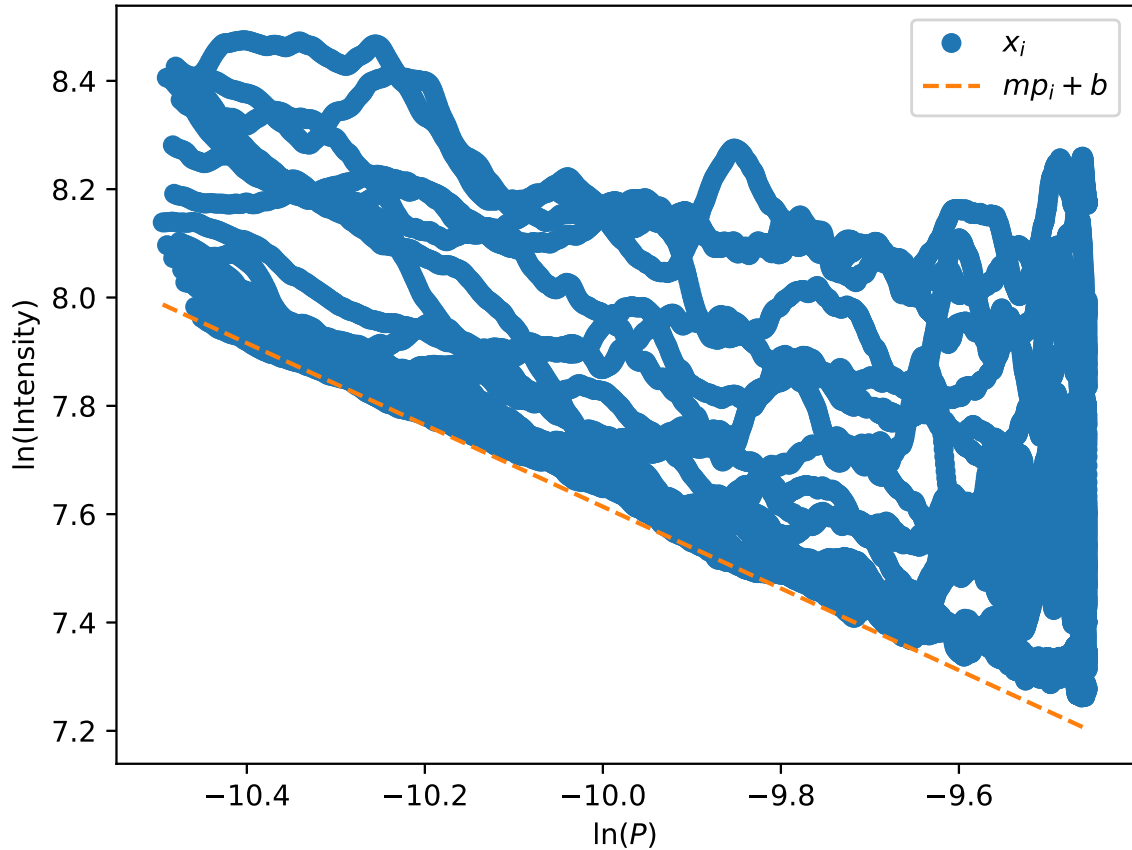


Figure 3.5: Example of the bounding line estimated from the linear program using data points from aggregated non-homogeneous bursts in a range split. The processed log measurements,  $x_i$ , in blue are bounded by the dashed orange line,  $mp_i + b$ , so that all  $x_i$  are above this line.

One final consideration is the transition between different range splits. Due to the simplicity of the parameter estimation model, there is no guarantee that the linear functions estimated at range splits will intercept close to the measured points. If uncompensated, this can result in discontinuities in the estimated noise-floor between adjacent range splits. To compensate for this,  $m$  and  $b$  are transitioned between range splits by means of linear interpolation between a boundary gap. This process is detailed in Algorithm 3. At this

stage, we denote the partial corrected result as

$$\tilde{X} = X - e^b P^m Y_{azimuth}, \quad (3.5)$$

with  $Y_{azimuth}$  being the azimuth noise vector taken from the ESA noise-calibration XML files. Fig. 3.6 provides a visual example of how the parameters estimated in the log domain of each range split are mapped to the real domain.

---

**Algorithm 3:** Smoothness interpolation of  $m$  and  $b$  between different range splits.

---

- 1 Let  $s_0$  and  $s_1$  be range splits in subswath  $a$ ;
  - 2 Let parameters  $m_0, m_1$  and  $b_0, b_1$  be associated with  $s_0$  and  $s_1$ ;
  - 3 Let  $\mathbf{u} = [u_0, u_1] \in \mathbb{Z}$  be the discrete range indices dividing  $s_0$  and  $s_1$ ;
  - 4  $m(i) = (1 - \frac{i}{u_1 - u_0})m_0 + \frac{i}{u_1 - u_0}(m_1 - m_0)$  for  $i \in \mathbf{u}$ ;
  - 5  $b(i) = (1 - \frac{i}{u_1 - u_0})b_0 + \frac{i}{u_1 - u_0}(b_1 - b_0)$  for  $i \in \mathbf{u}$ ;
- 

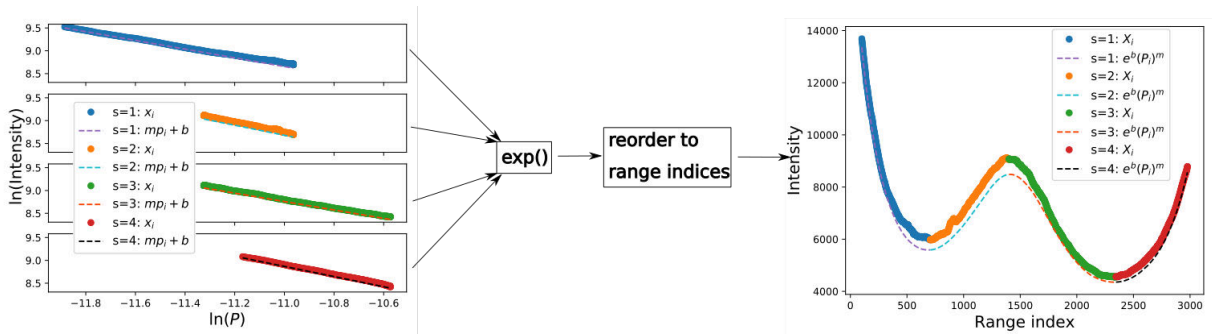


Figure 3.6: Association of how the log parameters are mapped to the real domain as the partial estimated noise floor. The figure shows the four range splits in subswath EW1 over a region of open-water. The left graph shows the measurements (solid) and estimated linear function (dashed) in the log domain. After exponentiation and reordering to range indices, the right graph shows

### 3.3.2 Subswath offsets

While we found that the power function would be effective at estimating the noise floor within subswaths, an issue remains in that the overall intensity between subswaths remains imbalanced from applying (3.5). To compensate, offsets are computed for each subswath using a weighted least-squares approach. The core of the problem is to choose a vector of

offset values  $\mathbf{o}$  so that the difference between values in adjacent subswaths is minimized. Specifically, this takes the form

$$\min_{\mathbf{o}} \left( \left[ \sum_{a \in \mathcal{A} - \max(\mathcal{A})} \sum_{g \in a} w_g (l(\tilde{X}, a, g) + o_a - (r(\tilde{X}, a, g) + o_{a+1}))^2 \right] + \sum_{a \in \mathcal{A}} \lambda(o_a)^2 \right), \quad (3.6)$$

where we take  $l(\tilde{X}, a, g)$  as the average of the 30 rightmost pixels of subswath  $a$  along the azimuth lines in  $g$ ,  $r(\tilde{X}, a, g)$  as the average of the 30 leftmost pixels of subswath  $a + 1$  along the azimuth lines in  $g$ ,  $w_g$  is a burst specific weight, and  $\mathcal{A}$  is the set of subswaths in the image. In the first summation the last subswath is skipped, since there are only  $N-1$  borders among  $N$  subswaths.

The selection of weights is based off of the statistical distribution of SAR backscatter. SAR backscatter is distributed by the gamma distribution [7], whose variance scales with the mean of the random variables. This means that regions with higher backscatter are less reliable for estimating  $\mathbf{o}$  than regions of lower backscatter and will cause poor estimations. The variance of a gamma random variable is  $E^2(X)/L$  [60], where  $E(X)$  and  $L$  are the expectation of  $X$  and the shape parameter respectively (i.e. the number of looks). We incorporate this knowledge by selecting the weights to be the inverse of the variance of the subtraction of two gamma random variables

$$w_g = \frac{L}{l^2(X, a, g) + r^2(X, a, g)}. \quad (3.7)$$

The regularization term  $\sum_a \lambda(o_a)^2$  is added to ensure that the system remains well-posed. Solving (3.6) is determined by solving a linear system [9].

### 3.4 Experiments

We implement three experiments to evaluate the impact of Algorithm 1, which we call the Proposed method. The first two experiments are adapted from previous work [30] that aim to evaluate and compare the quality of the different correctional methods. The first experiment is a simulation experiment that takes 21 RADARSAT-2 images and adds an artificial noise floor by adding (3.1). The second evaluates the appearance on Sentinel-1



images, measuring improvement quantitatively by the calculating the error of the measurements with respect to a linear regression over open-water regions, assuming that the ideal intensity over these regions is flat. The third experiment aims to analyze the change in radiometric bias that is incurred by the Proposed method on Sentinel-1 images. Where possible, we make comparisons of the Proposed method to the unmodified images, the noise floor provided by ESA, which we call the ESA method, and the method from [30], which we refer to as the Previous method. However, the method from [30] was only implemented for EW images, so it was excluded for analysis concerning IW images. Note for display purposes the amplitude, the square root of intensity, is used to display the images.

### 3.4.1 RADARSAT-2: Simulation

The goal of the simulation experiment is to investigate the ability to re-estimate parameters of an artificially applied noise floor, where the ground truth clean image is known. We follow the approach from our previous work [30], where we selected 21 RADARSAT-2 images over the Beaufort sea and subsequently generate and synthesize a noise floor through the power function model (3.1). We selected a template EW image <sup>1</sup> and a template IW image<sup>2</sup> with similar characteristics of the RADARSAT-2 images for which to model the noise floors and intensity values.

There are several key differences in this simulation experiment compared to our previous work. First, we ran this set of experiments using both EW and IW noise floor profiles. Second, the noise floor was simulated using the power function model, rather than the noise floor originally provided by the ESA. Third, instead of selecting scaling parameters by sampling random distributions as we did in [30], we took a more conservative approach. While the previous model only had one parameter to estimate per subswath, the power function model has many more parameters. Randomly selecting parameters in the power function model can generate unrealistic noise floors. Instead, we found it necessary to reuse parameters that were estimated by from the experiment in Section 3.4.2.

Before simulating the noise on the RADARSAT-2 images, several image transformation steps were carried out to ensure that the intensity values for the RADARSAT-2 image and the Sentinel-1 image were similar. First, the pixels in the RADARSAT-2 image were squared to convert to intensity and spatially linearly interpolated to be the same size as the template. A lookup table was created to map the percentiles of the recorded intensities over all of the RADARSAT-2 images in 0.1% increments. A second lookup table was created to map the percentiles of the intensities for the template Sentinel-1 image after it

---

<sup>1</sup>S1B\_EW\_GRDM\_1SDH\_20200112T051555\_20200112T051655\_019779\_02565A\_2451

<sup>2</sup>S1B\_IW\_GRDH\_1SDV\_20200111T232801\_20200111T232836\_019776\_025644\_396F

was corrected by the Proposed method. These two mappings were then applied to map the RADARSAT-2 intensities to the template Sentinel-1 image.

After the image transformation steps, the simulated noise floor was added onto the image using the selected parameters. As in previous work [30], we used the metrics of Structural Similarity Index (SSIM) [54], Normalized mean squared error (NRMSE), and Peak Signal to Noise Ratio (PSNR) to compare the freshly denoised images to the ground truth results. There were up to four different methods that would be compared, the unprocessed noisy image, the default ESA method, the Proposed method, and optionally the method from [30] for the EW template image.

A sample of the visual results of the simulation are shown in Fig. 3.7 (EW), Fig. 3.8 (IW), and Fig. 3.9. Many of the images, such as Figs. 3.7 and 3.8 show positive results, however there were a few instances, like in Fig. 3.9 where the end result was less successful. The overall metrics are shown in Table 3.1 for both EW and IW cases. In terms of statistics, one-tailed Wilcoxon tests with a threshold of 0.05 were applied for each metric to determine if the Proposed method was significantly better than the other methods, due to the non-normal distribution of residuals. Overall, the Proposed method had better image quality than the original unprocessed image, the ESA method, and the Previous method in terms of the metrics. The improvement was within significant levels except for the Previous method in terms of SSIM for the EW case and PSNR for the ESA method for the IW case.

Table 3.1: Quality metric comparisons for simulation experiment. P-values are taken from a one-tailed Wilcoxon test, comparing the metrics to the Proposed method. Bold p-values indicate significance and non-bold indicates non-significance at a threshold of 0.05.

Method	NRMSE	P-value	PSNR	P-value	SSIM	P-value
EW						
Original	$3.49 \times 10^{-1}$	<b><math>2.98 \times 10^{-5}</math></b>	19.92	<b><math>2.98 \times 10^{-5}</math></b>	0.43	<b><math>2.98 \times 10^{-5}</math></b>
ESA	$6.73 \times 10^{-2}$	<b><math>2.98 \times 10^{-5}</math></b>	28.68	<b><math>2.98 \times 10^{-5}</math></b>	0.79	<b><math>1.85 \times 10^{-3}</math></b>
Previous [30]	$1.88 \times 10^{-2}$	<b><math>4.51 \times 10^{-4}</math></b>	37.82	<b><math>3.09 \times 10^{-4}</math></b>	0.91	$3.58 \times 10^{-1}$
Proposed	$5.52 \times 10^{-3}$	N/A	45.21	N/A	0.94	N/A
IW						
Original	$4.61 \times 10^{-1}$	<b><math>2.98 \times 10^{-5}</math></b>	13.15	<b><math>2.98 \times 10^{-5}</math></b>	0.32	<b><math>2.98 \times 10^{-5}</math></b>
ESA	$3.63 \times 10^{-2}$	<b><math>1.49 \times 10^{-2}</math></b>	29.51	$1.29 \times 10^{-1}$	0.87	<b><math>3.18 \times 10^{-3}</math></b>
Proposed	$3.11 \times 10^{-2}$	N/A	30.50	N/A	0.90	N/A

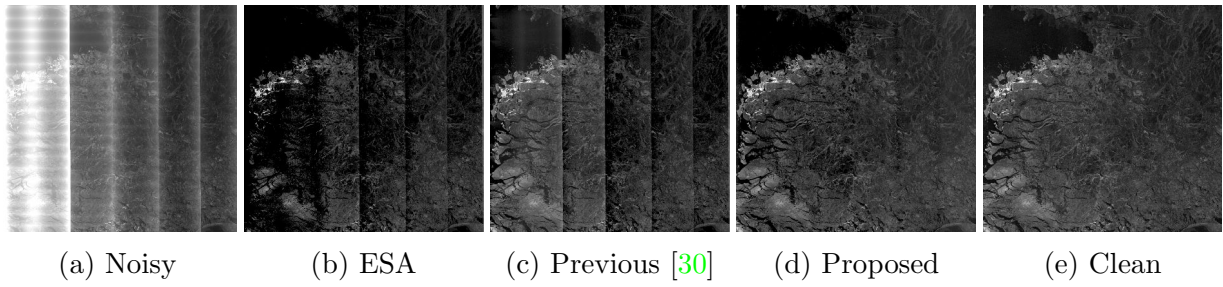


Figure 3.7: Simulated EW correction comparison. Visually the Proposed method is able to remove the sharp discontinuities between subswaths.

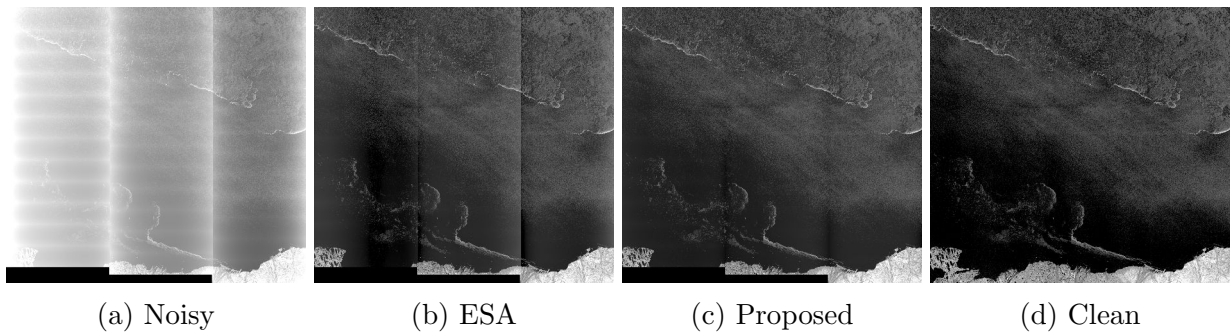


Figure 3.8: Simulated IW correction comparison. The Proposed method produces cleaner results, albeit still with some distortion at the subswath boundaries. Again, note that no comparison was made to the Previous method due to it not being implemented for IW images.

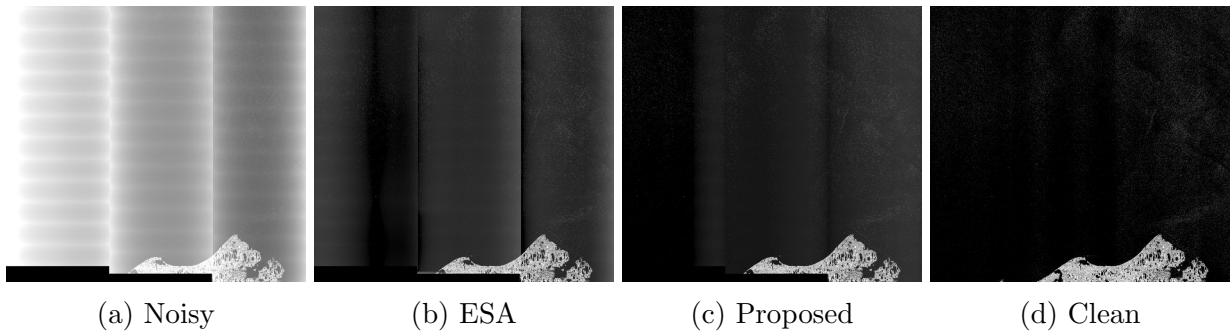


Figure 3.9: Example of scene where the Proposed method is less successful. Although the transitions between subswaths are continuous, the first range split in IW1 is not estimated correctly.

### 3.4.2 Sentinel-1: Appearance

To evaluate our method, samples of 40 EW and 18 IW Sentinel-1 images, with IPF version 3.1 or above, were selected to compare the Proposed method to the baseline methods. For EW images, we attempted to select a sample from all five oceans. The selection of IW images was less diverse, as IW mode is not specialized towards ocean regions. Thus, the IW images were selected from a select few coastal regions in the Pacific Ocean and Hudson Bay. Some examples of these EW and IW images are shown in Figs. 3.10, 3.11, and 3.12, which show the visual difference between the Proposed method and the baseline methods.

Due to the unavailability of a ground truth image without noise, we could not evaluate the effectiveness of the method using conventional pixel difference measures. A characteristic we exploited for our analysis is the appearance of open-water. Due to the low backscatter coefficient of calm water [48], one should expect that a region of calm water would have a relatively flat intensity profile. We then expected that significant variation along the range is a result of the changing noise floor. So if a noise floor removal method has significant variance along a region of open-water, we assume that this is the result of uncompensated noise-floor.

To accommodate this strategy, we selected rectangular regions from the 40 EW and 18 IW images spanning the range of the image that we deemed to be open-water through visual inspection. The mean was computed along the azimuth of each rectangular regions so that points of measurements along the range were generated for each rectangle. This vector was also convolved with boxcar filter of size 151 for the values in each subswath, using valid padding, in order to remove the outliers and isolate the overall intensity changes.

The quantitative measure was derived by computing the normalized root mean squared error (NRMSE) of the processed points, as mentioned above, with respect to a best fit linear regression, for each method. These results are summarized in Table 3.2. Due to the non-normal distribution of the residuals, one-tailed Wilcoxon non-parametric tests were used to test the significance of the NRMSE difference between the Proposed method and the other baseline methods. For EW, the Proposed method had statistically lower NRMSE than the unmodified image, the images produced using the default ESA noise floor, and those modified by using the Previous method. The Proposed method also had a significantly lower median for IW images, albeit the magnitude of improvement was less. While we saw an overall improvement, the magnitude of improvement varied for each image.



Origin	Original	ESA	Previous	Proposed
Arctic 81.7°N, 83.0°E 2019-09-11				
Arctic 83.9°N, 70.9°E 2019-08-23				
Arctic 82.7°N, 96.8°E 2019-07-17				
Antarctic 63.5°S, 51.1°E 2020-01-05				
Antarctic 64.2°S, 15.7°W 2020-01-12				
Antarctic 66.7°S, 6.1°E 2019-12-24				

Figure 3.10: Comparison of Sentinel-1 EW images part 1. Coordinates coorespond to the center.

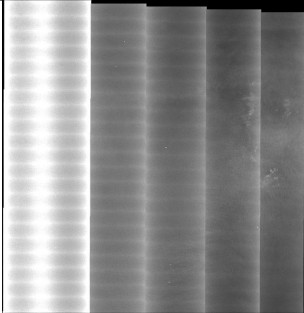
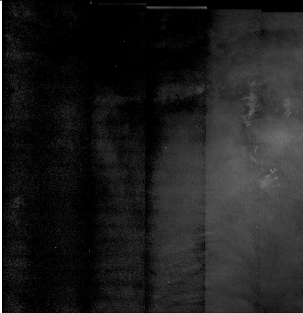


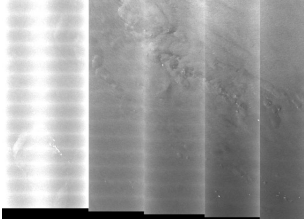
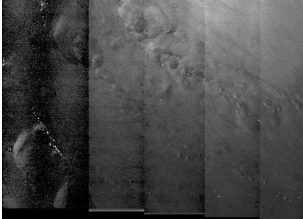
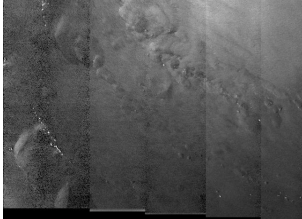
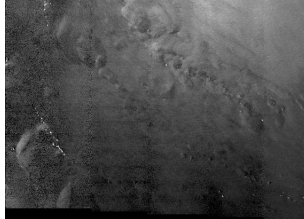
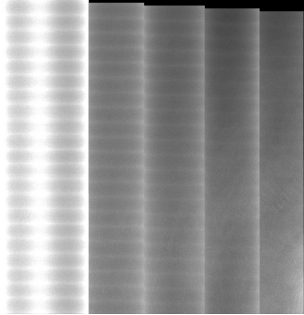
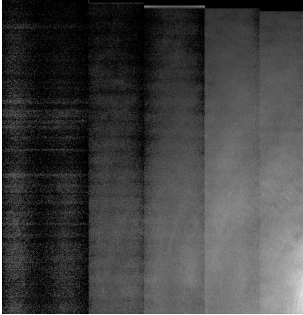
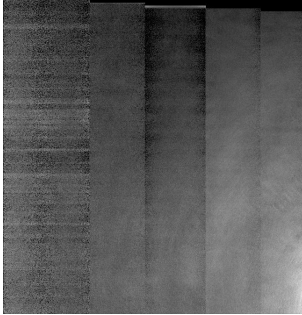
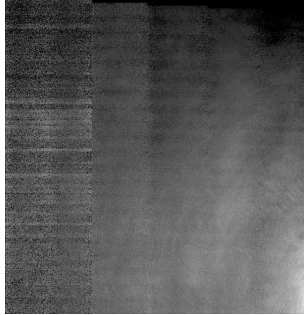
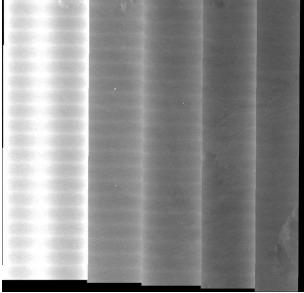
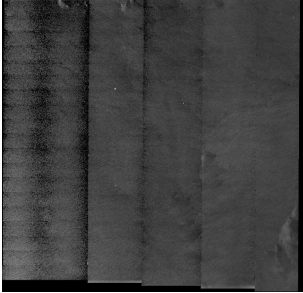
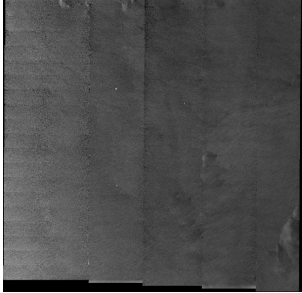
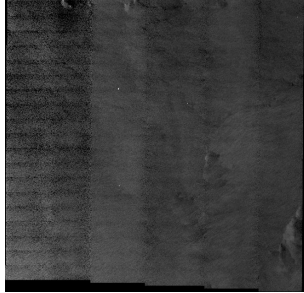
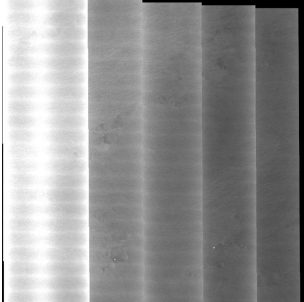
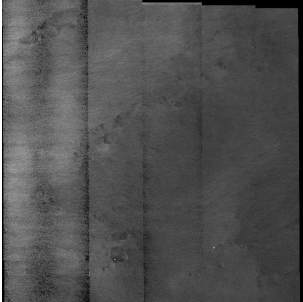

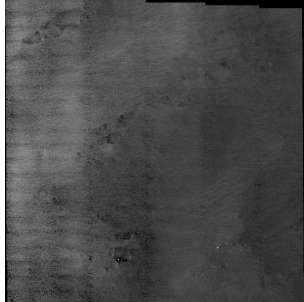
Origin	Original	ESA	Previous	Proposed
Atlantic 42.3°N, 34.9°W 2019-10-17				
Pacific 16.6°N, 116.6°W 2019-09-04				
Pacific 17.4°N, 120.8°W 2019-09-05				
Indian 15.0°S, 54.8°E 2019-10-08				
Indian 14.9°S, 55.6°E 2019-10-07				

Figure 3.11: Comparison of Sentinel-1 EW images part 2.

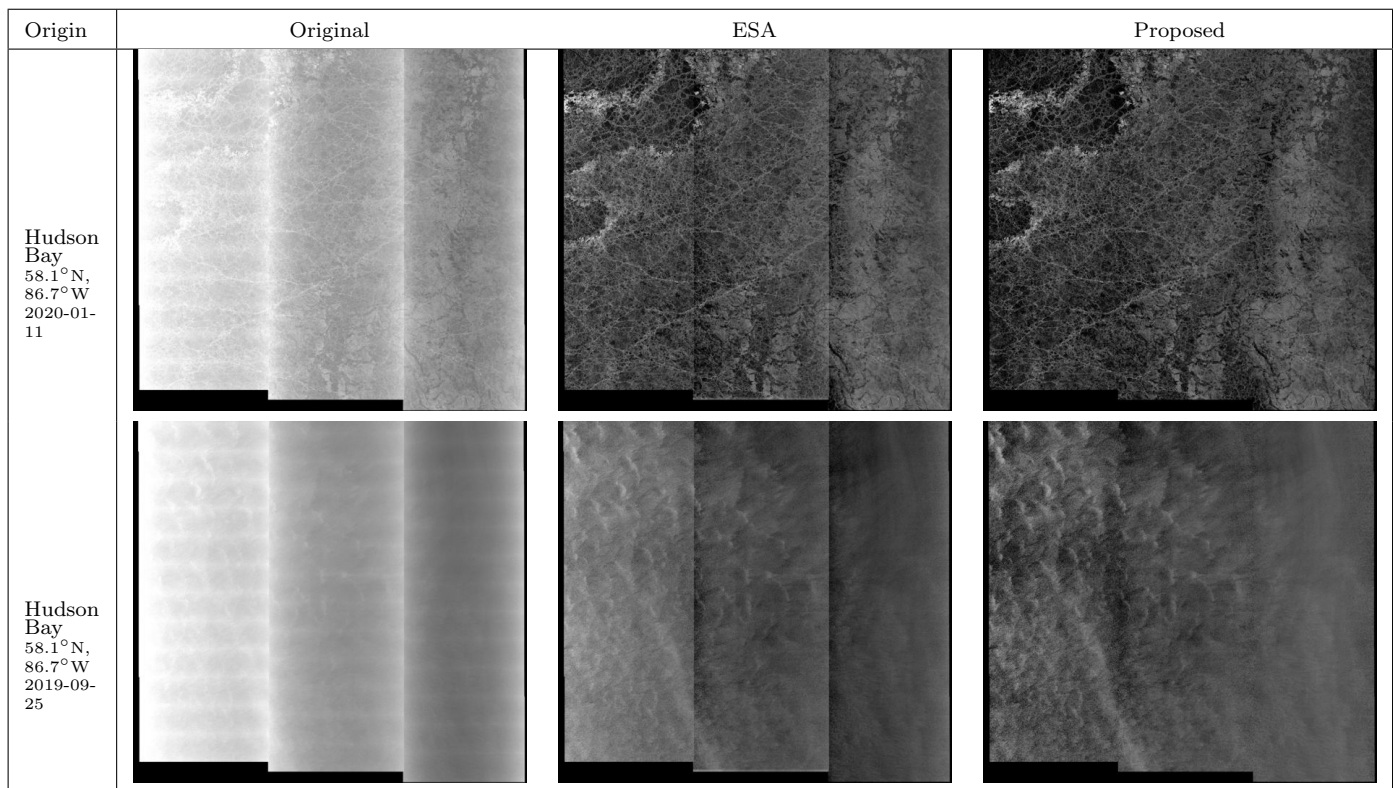


Figure 3.12: Comparison of Sentinel-1 IW images captured within the Hudson Bay.

Table 3.2: NRMSE values in experiment comparison for range regression over open water. Results are listed for both EW (N=40) and IW (N=18) images as indicated. The listed p-value is derived through a one-tailed Wilcoxon test to determine if the proposed method has a lower NRMSE than the other methods.

Method	Median NRMSE	P-value (Wilcoxon)
EW (N=40)		
Original	$2.87 \times 10^2$	$1.78 \times 10^{-8}$ ✓
ESA	$3.75 \times 10^0$	$5.92 \times 10^{-8}$ ✓
Previous [30]	$3.20 \times 10^0$	$1.88 \times 10^{-6}$ ✓
Proposed	$1.07 \times 10^0$	N/A
IW (N=18)		
Original	$2.04 \times 10^1$	$9.82 \times 10^{-5}$ ✓
ESA	$9.10 \times 10^{-1}$	$3.21 \times 10^{-2}$ ✓
Proposed	$3.83 \times 10^{-1}$	N/A

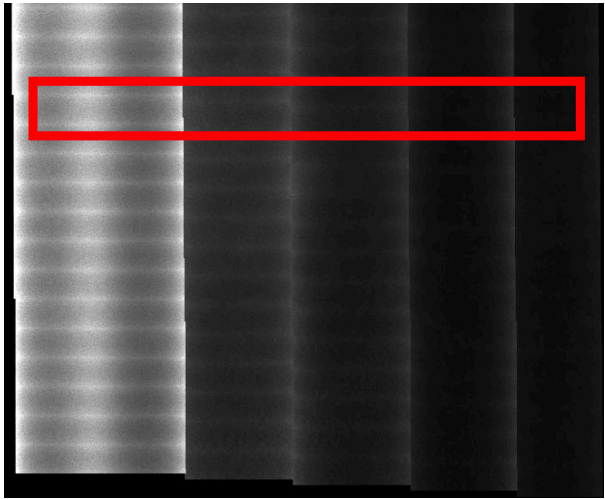
### 3.4.3 Sentinel-1: Intensity bias

One consideration to be aware of when designing noise floors is the effect of the overall intensity among subswaths after subtraction. A potential undesired outcome from modifying noise floors is raising or lowering the overall intensity of the SAR images so that the backscatter intensity does not match the expected intensity of a physical ground target, so that there is a bias of intensity away from expected radar cross section. Consequently, this experiment aims to evaluate how the total intensity varies in subswaths for between the Proposed and ESA correction methods. This is done by directly comparing the overall intensity in each subswath between the methods through paired differences.

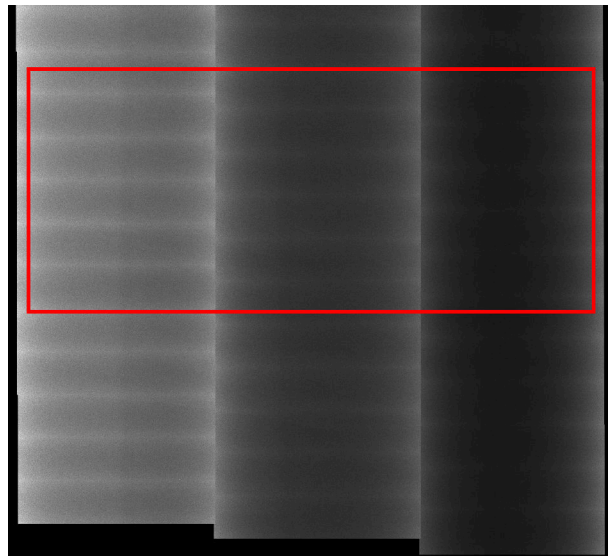
The data used in this experiment is essentially the same as the previous experiment, but instead of attempting to measure the quality of the images, we measure overall change in bias. For each corrected image, the mean intensity measurements were computed for each subswath. Thus, a vector of size 40 (EW) or 18 (IW) was made for each subswath and each of the two correction methods.

The change in bias was evaluated on a subswath-wise manner so that the paired differences were taken between the two correction method for each subswath. The significance of its difference vector was evaluated using a two-tailed paired t-test, with the implied null hypothesis being that the mean intensity for the subswath is the same for the two methods. Ultimately, all intensities showed the means were significantly different, save for

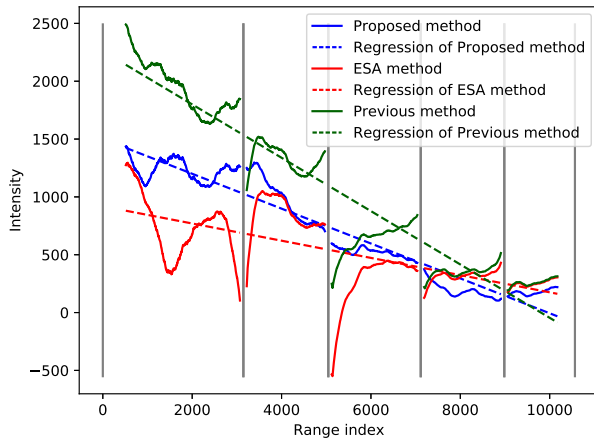




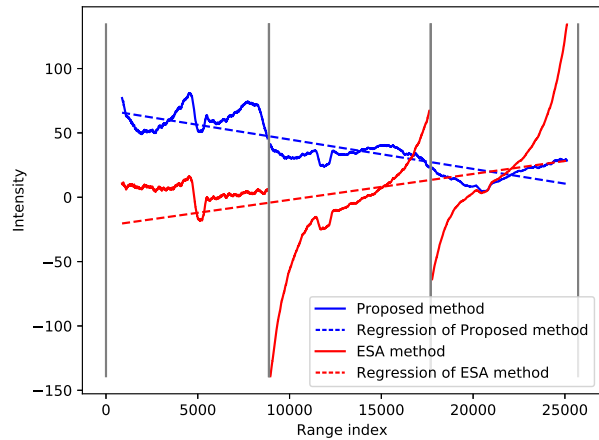
(a) EW original



(b) IW original



(c) EW regression



(d) IW regression

Figure 3.13: Top figures show zones of open water that are pre-selected in red. Bottom figures showing the regression along the range over sections of open-water. The Proposed method (blue), is compared to the ESA method (red) and the Previous method from [30] (green). In these examples, the ESA method and Previous method have noticeable discontinuities at the start and end of each subswath, something that the Proposed method is able to compensate.

Table 3.3: Average intensity values of different subswaths for ESA and Proposed. The percentage of the original measurement is also recorded below for reference. P-values from paired two-tailed t-test are recorded comparing the distribution of intensities between the ESA and Proposed. For reference, the percentage is reported under the values to indicate the average ratio of the final intensity with respect to the original unprocessed measurements (i.e. the noisy image).

Subswath	ESA	Proposed	P-value (t-test)
EW1	862 8.74%	1124 11.39%	$4.36 \times 10^{-2}$ ✓
EW2	988 27.50%	1166 32.46%	$3.69 \times 10^{-4}$ ✓
EW3	1006 34.01%	1127 38.12%	$1.32 \times 10^{-3}$ ✓
EW4	1123 50.37%	1074 48.15%	$3.72 \times 10^{-1}$ ✗
EW5	1049 52.82%	968 48.78%	$3.41 \times 10^{-1}$ ✗
IW1	455 26.36%	441 25.51%	$4.67 \times 10^{-1}$ ✗
IW2	216 24.04%	192 21.33%	$1.17 \times 10^{-2}$ ✓
IW3	297 41.15%	256 35.45%	$1.10 \times 10^{-3}$ ✓

EW4, EW5, and IW1. These results are shown in Table 3.3. Overall, this indicates that there is a significant difference in radiometric bias between the results of the two methods.

### 3.5 Discussion

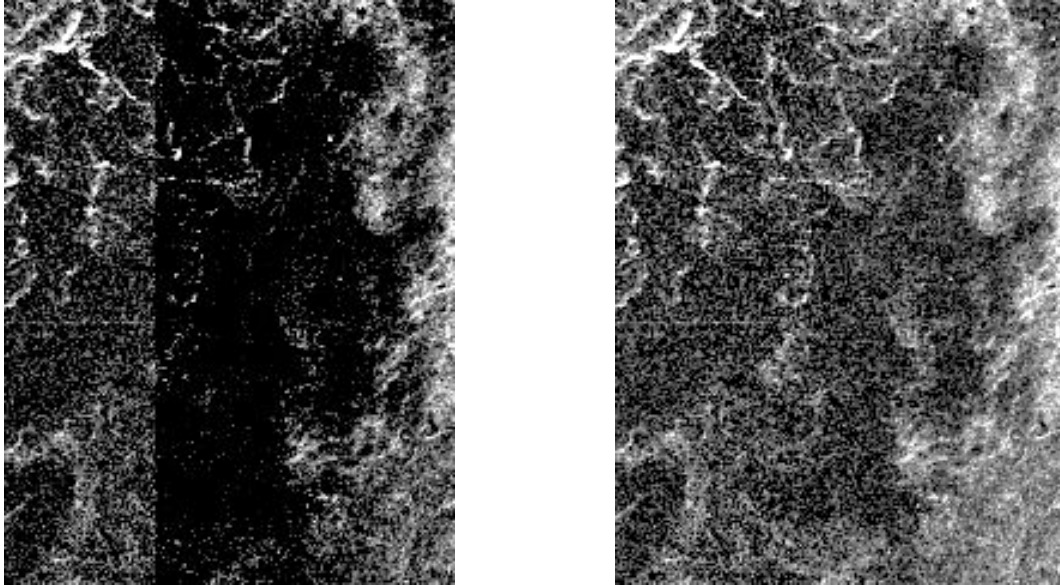
Within the experiments, there is significant evidence that the Proposed method is able to accomplish the goal for compensating for non-linear mis-shape in the noise floor. The first two experiments directly support the ability of the Proposed method to improve image quality. While the third experiment indicates that there is a significant difference in radiometric calibration, we describe the implications of this in more detail below. We also

discuss some other important details regarding parameter estimation and other factors on the observed intensity.

The results from the simulation experiment also indicate that the Proposed method is able to result in a better quality images than the alternatives under the assumptions of the simulation pipeline. The three metrics generally support the effectiveness of the Proposed method over the baseline methods. Statistically, the metrics showed significant improvement except for the PSNR metric in EW and the SSIM metric in IW. There were some examples however, as shown in Fig. 3.9, where the Proposed method was less successful. This highlights a key assumption made by the Proposed method of there being sufficient critical points along the line  $mp + b$  that best fits the true noise floor. If there are not sufficient points, then the parameters may estimate in a less successful manner, which typically occurs when  $m$  is tightly fit to the constraints of  $m \geq -0.75$  or  $m \leq -1.25$ . For example in Fig. 3.9,  $m = -1.25$  for the rightmost range split of IW1, where the result is most divergent from the ground truth.

The images generated in the second experiment such as in Figures 3.10, 3.11, and 3.12 show that the Proposed method is able to compensate for the noise floor in both EW and IW images. Visually, there was a large improvement in image quality induced by the Proposed method over the other methods, which was particularly evident by the smooth transitions between subswaths. To this end, this demonstrates visual evidence that the non-linear mis-fit is compensated effectively. Quantitatively, the range regression over open-water provides strong evidence that the Proposed method can estimate more accurate noise floors than the alternative methods. The Proposed method had significant improvement of normalized mean squared error with respect to the regression along the range. Specifically for EW images, the improvement is of high impact and is successful in normalizing the intensity changes. For IW images, there was still significant improvement, albeit with less impact due to the higher signal-to-noise floor-ratios from the sensor mode. In terms of the types of surfaces captured in IW images, noise floor compensation towards land surfaces is less necessary since the measurements are dominated by backscatter intensity. Instead, the method shows more promise towards IW images containing water or ice, and thus could be useful towards supporting remote sensing applications over inland water or ice.

The main result from the third experiment is that there is a difference in overall intensity between the Proposed method and the ESA method. This implies that there is a significant difference in radiometric bias; an important factor depending on the remote sensing application. Whether this is an adverse change in radiometric bias is not clear. For example, Fig. 3.14 shows that the ESA method results in sections of the ice formation being removed because the output results intensity values below zero. In contrast, the Proposed method produces a suitable noise floor where the ice features can be seen fully.



(a) ESA

(b) Proposed

Figure 3.14: Close up example comparing ESA and Proposed denoised examples extracted from the image in  $64.2^{\circ}\text{S}, 15.7^{\circ}\text{W}$ , 2020-01-12, as seen in Fig. 3.10. Notice that the ESA method loses ice features due to the noise floor being too high at the subswath transition, thus losing important features.

In this case, the ESA method is clearly mis-calibrated because significant features are lost, which suggests that the ESA method may not be an ideal ground truth for radiometric calibration. Consequently, depending on application one must be mindful of these changes in intensity bias. It should be noted that while the change is significant, the total change between the methods relative to the original measurements is usually only a few percentages for each subswath, so if an application is specifically adapted for ESA method, then it could probably be adapted for the Proposed method with few changes.

In terms of parameter estimation, Fig. 3.15 summarizes the parameters  $m$ ,  $b$ , and  $o$  estimated for the Sentinel-1 experiment. An interesting observation is the correlation between  $m$  and  $b$  is extremely high, with coefficients of 0.9778 for EW and 0.9777 for IW. The plot shows that each parameter estimated is not independent, with each parameter having a clear centre. However, the spread of estimates is still quite large. Fig. 3.16 likewise shows the spread of parameters for the simulation experiment. The same correlation between  $m$  and  $b$  is clear, with coefficients of 0.9925 for EW and 0.9961 for IW. Compared

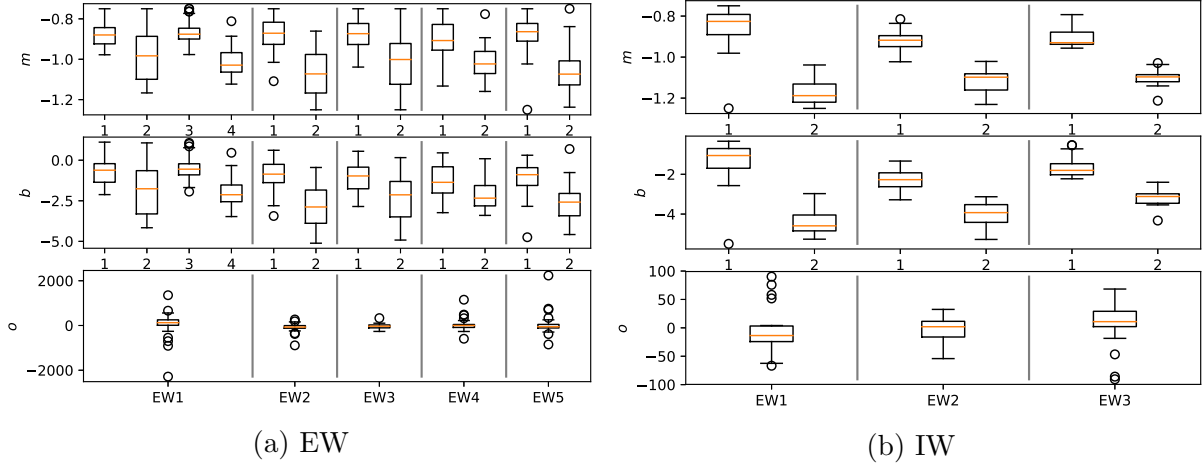


Figure 3.15: Spread of parameter estimates for the experiment on Sentinel-1 images for  $m$  (top),  $b$  (middle), and  $o$  (bottom). The boxplots are marked by their range split on the horizontal axis and divided into their respective subswaths by the gray vertical lines.

to Fig. 3.15, the spread of the estimates in the simulation experiment is much smaller. Indeed for the simulation experiment the sum of standard deviations was 0.6962 for EW and 0.2388 for IW while for the Sentinel-1 experiment it was 1.077 for EW and 0.3787 for IW. This is an important observation that supports the importance of estimating new parameters for every scene because if the ideal parameters were the same for each scene the spread of both of the experiments would be more similar. Specifically for the simulation experiment, the parameter estimates appear to be centred around the ground truth for the EW case, especially in lower SNR subswaths (e.g. EW1), with estimates becoming more divergent with later subswaths with higher SNR (e.g. EW5). The estimates also showed divergence for the IW case in later subswaths. An explanation for the divergence may be due to the over-determined nature of the model. This is especially true for subswaths with a lower magnitude relative noise floor, where the curvature of  $P$  is less severe. Depending on the magnitude and shape of  $X$  and  $P$ , different combinations of parameters can result in similar results.

Another factor to consider is that the total intensity of individual bursts in a subswath can differ due to non-local targets. Fig. 3.17 shows two examples where the intensity from high backscatter targets bleeds over into low intensity targets within the burst, thereby causing discontinuity between adjacent bursts. The cause for this likely lies in the signal processing pipeline, where the observed signal components of the backscatter radiation within the range of the subswath is transformed into the spatial intensity seen within the

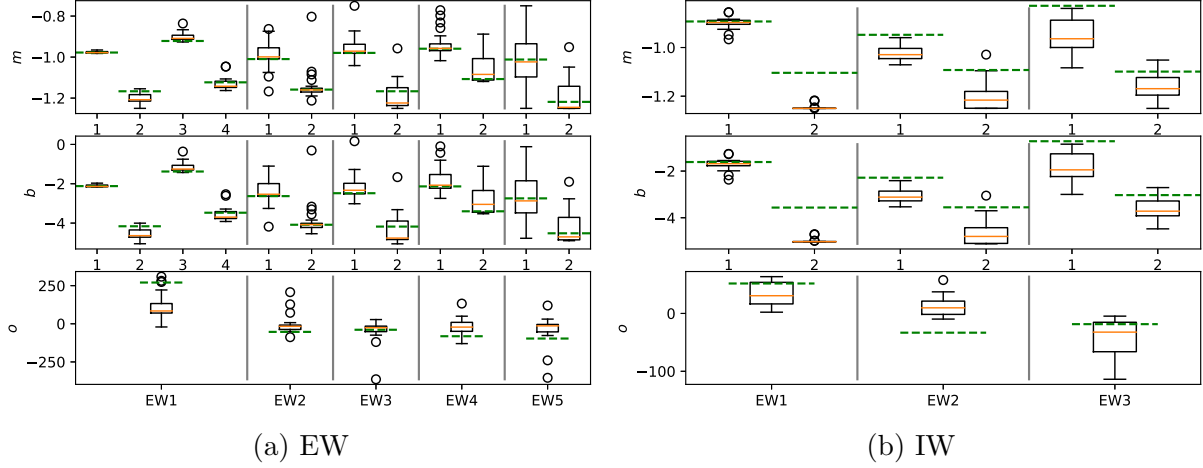


Figure 3.16: Spread of parameter estimates for the experiment on RADARSAT-2 images. The ground truth parameters used to generate the noise floor is marked by the horizontal dashed green lines. All remaining conventions are the same as Fig. 3.15.

image. This cannot be compensated by the current Proposed method because it assumes that the noise floor should be calibrated in the same way for each burst throughout the entire subswath. Correcting this on the image processing side would require estimating parameters for each specific burst. However, this would be difficult to accomplish due to the limited amount of data in a single burst needed to produce estimates.

A final consideration regarding image quality is the compensation for speckle. While directly out of scope for this manuscript, it is worth mentioning its impact on the images. Speckle in SAR is typically modelled with the Gamma distribution [7] and is described as multiplicative noise, where its variance increases with respect to the original signal. As a result, even when the noise floor is subtracted the increased variance remains in regions where the noise floor was higher. If one were to combine a despeckling approach with our method, they must bear in mind that the statistics of speckle are still linked to that of the original measurements.

### 3.6 Conclusion

In this manuscript we proposed a new model for estimating the noise floor in Sentinel-1 GRD intensity images in order to account for non-linear mis-fit of the default noise floor estimation that other methods in the literature cannot compensate for. The model con-



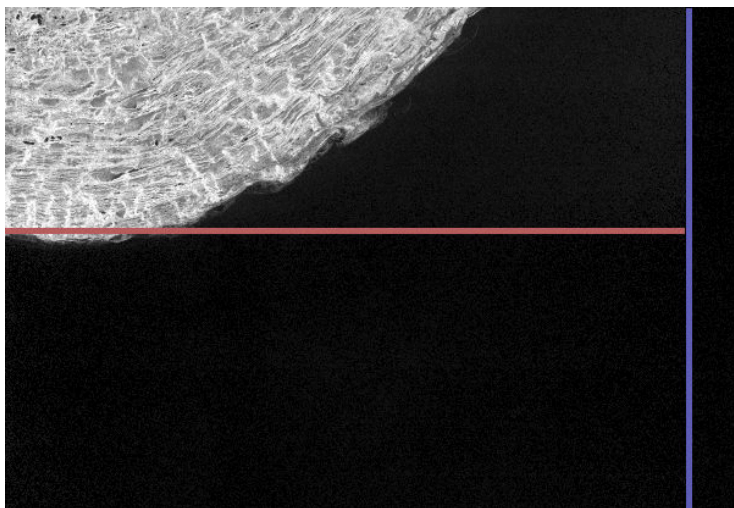


Figure 3.17: Example of an IW image where high intensity targets *bleed over* into other targets within the burst. This causes discontinuity between adjacent bursts, as indicated by the burst division (red line). The division between subswaths (blue line) is identified for reference.

siders the noise floor to be an power function of the radiation pattern power. We observed that different trends occur at different sections of each subswath and therefore estimate multiple power functions per subswath. Through log transformation the problem of estimating parameters for the power functions is relaxed to a linear programming problem. To account for affine imbalance between subswaths, subswath-wise offsets are computed using a weighted least squares approach, making the entire estimation a convex optimization problem. The method was overall successful in estimating the noise floor in both Sentinel-1 images and simulated images. While there is a change in radiometric bias, compared to the baseline method provided by the ESA, the impact of this will depend on the remote sensing application.

## Appendix

**Claim.** *Linear program (3.4), without the constraints  $m \leq -0.75$ , and  $m \geq -1.25$ , is unbounded for  $\gamma > \max(\mathbf{p})$ ,  $\gamma < \min(\mathbf{p})$ , and  $\gamma < 0$ .*

*Proof.* Assume that log antenna power vectors  $\mathbf{p} < 0$  and log measurement vectors  $\mathbf{x} > 0$ .

For the linear program to be unbounded, then for

$$\begin{aligned} \gamma m + b &\geq t, t \in \mathbb{R}^+ \\ \implies m &\leq \frac{t-b}{\gamma} \end{aligned} \quad (3.8)$$

there exists a feasible choice of  $m$  and  $b$ . Given the inequalities

$$\begin{aligned} mp_i + b &\leq x_i \\ \implies m &\geq \frac{x_i - b}{p_i} \end{aligned} \quad (3.9)$$

then there are feasible values of  $m \in [\frac{x_i-b}{p_i}, \frac{t-b}{\gamma}]$ .

Case 1:  $\gamma > \max(\mathbf{p})$

Let  $\gamma = \max(\mathbf{p}) + \epsilon, \epsilon > 0$ . Then  $m \in [\frac{x_i-b}{p_i}, \frac{t-b}{\max(\mathbf{p})+\epsilon}]$ , which is non-empty if  $\frac{x_i-b}{p_i} \leq \frac{t-b}{\max(\mathbf{p})+\epsilon}$ . For this to be true,  $b$  must be chosen to satisfy the constraints

$$\begin{aligned} (x_i - b)(\max(\mathbf{p}) + \epsilon) &\leq (t - b)p_i \\ \iff x_i(\max(\mathbf{p}) + \epsilon) - tp_i &\leq b(\max(\mathbf{p}) - p_i + \epsilon) \\ \iff -x_i(|\max(\mathbf{p}) + \epsilon|) + t|p_i| &\leq b(|\max(\mathbf{p}) - p_i + \epsilon|) \\ \iff \frac{-x_i(|\max(\mathbf{p}) + \epsilon|) + t|p_i|}{|\max(\mathbf{p}) - p_i + \epsilon|} &\leq b \quad \forall i \end{aligned} \quad (3.10)$$

because  $(\max(\mathbf{p}) - p_i + \epsilon) > 0$ . Then  $b$  has a lower bound value that will satisfy all constraints as

$$\Omega(b) = \max_i \left( \frac{-x_i(|\max(\mathbf{p}) + \epsilon|) + t|p_i|}{|\max(\mathbf{p}) - p_i + \epsilon|} \right) \quad (3.11)$$

Therefore there exists  $m, b$  for any positive  $t$  and is thus unbounded for  $\gamma > \max(\mathbf{p})$ .

Case 2:  $\gamma < \min(\mathbf{p})$ .

Let  $\gamma = \min(\mathbf{p}) - \epsilon, \epsilon < 0$ . By similar logic  $m \in [\frac{x_i-b}{p_i}, \frac{t-b}{\min(\mathbf{p})-\epsilon}]$ , which is non-empty if  $\frac{x_i-b}{p_i} \leq \frac{t-b}{\min(\mathbf{p})-\epsilon}$ . Non-emptiness is true if  $b$  is chosen to satisfy

$$\begin{aligned} (x_i - b)(\min(\mathbf{p}) - \epsilon) &\leq (t - b)p_i \\ \iff x_i(\min(\mathbf{p}) - \epsilon) - tp_i &\leq b(\min(\mathbf{p}) - p_i - \epsilon) \\ \iff -x_i(|\min(\mathbf{p}) - \epsilon|) + t|p_i| &\leq -b(|\min(\mathbf{p}) - p_i - \epsilon|) \\ \iff \frac{-x_i|\min(\mathbf{p}) - \epsilon| + t|p_i|}{-|\min(\mathbf{p}) - p_i - \epsilon|} &\geq b \quad \forall i \end{aligned} \quad (3.12)$$



because  $(\min(\mathbf{p}) - p_i - \epsilon) < 0$ . Then  $b$  has an upper bound value that will satisfy all constraints as:

$$O(b) = \max_i \left( \frac{-x_i |\min(\mathbf{p}) - \epsilon| + t|p_i|}{-|\min(\mathbf{p}) - p_i - \epsilon|} \right) \quad (3.13)$$

Therefore there exists  $m, b$  for any positive  $t$  and is thus unbounded for  $\gamma < \min(\mathbf{p})$ .  $\square$

# Chapter 4

## Conclusion

In summary, the subtraction of noise floor is a critical preprocessing step for Sentinel-1 image analysis. Uncorrected, the noise floor intensity patterns distract from the desired backscatter intensity of the ground targets and make comparisons throughout the image more difficult. In Chapter 2, it was identified that the noise floor estimations provided by the ESA were severely miscalibrated for versions of the IPF below 3.1. To compensate, a method of dynamically estimating linear scaling parameters for each subswath was developed, resulting in significant improvement in EW images. The method was validated with experiments that gauged the image quality on images with added simulated noise floors and on real Sentinel-1 EW images over open-water regions, showing significant improvement over the baseline noise floors provided by the ESA. This method, however, assumes that the noise floor is mis-fit in a linear manner, which evidently is not always true, even for IPF versions 3.1 or above. In Chapter 3 these problems are addressed by assuming a noise floor model as a power function of the antenna radiation pattern power. This method showed significant improvement at compensating for the non-linear misfit within a simulation experiment and an experiment on Sentinel-1 images. Ultimately, the method in Chapter 3 is an improvement over the method in Chapter 2 through its ability to deal with the non-linear mis-fit of the ESA noise floor estimation. Both works have limitations within the methods and the analysis that motivate the following directions for future work.

## 4.1 Future work

While the appearance of the images have been improved by the two works, there are still various avenues for future work. The first avenue is a more thorough evaluation of the impact on radiometric calibration and on specific remote sensing tasks. The second is applying the proposed methods to other SAR acquisition modes or platforms. The third, which is particularly relevant to the work in Chapter 3, is improving the model to ensure robust parameter estimation.

In terms of radiometric calibration, there are still several questions that need to be resolved. While in Chapter 3 it was established that there was a difference in radiometric bias compared to the baseline, it was not clear whether this was a negative change (see Section 3.5). Some very relevant work done by [48] produced an insightful analysis on the calibration of Sentinel-1 by performing experiments that compared the backscatter measurements in images to targets with known radar cross section values and determined scenarios where the measurements had bias. It would be interesting to extend a similar study to the images corrected by the proposed methods to determine the scenarios that have been improved upon and the scenarios that still require improvement. As the number of applicable tasks that utilize SAR are vast, the sensitivity towards radiometric calibration will vary between different tasks. Therefore, a related area for future work would be determining what actions are required, if any, in order to adapt the new intensity values to different remote sensing tasks.

Although the main datasets used in the presented works were specific modes of Sentinel-1, these methods could be conceivably adjusted to other SAR platforms. However, there are some requirements in order for this to be feasible or necessary. To be feasible, either a noise floor estimate or a radiation pattern must be known to apply either the methods in Chapter 2 or Chapter 3 respectively. To be necessary, the images must have a discernible noise floor (meaning that the signal to noise ratio must be low enough to warrant attention) and it must vary significantly throughout the acquired image. It would likely be unnecessary to apply the methods to image modes with low changes in elevation angles, like Stripmap mode, because the radiation pattern will not vary as significantly over the captured area. Thus, it would be less necessary to apply advanced noise floor estimation methods when the noise floor is stationary throughout the image. Indeed, the primary candidate of SAR images that require compensation are those that capture wide and multiple subswaths, because this inevitably causes large changes in radiation pattern strength due to the physical limitations of the antennas.

One avenue of future research that is particularly relevant to the method in Chapter 3 is finding ways to ensure that the estimation of parameters is robust. As mentioned in

Section 3.5, the model in the third chapter is over-determined, meaning that there could be multiple solutions that result in a similar final result for each individual optimization problem. The issue is that there is no communication between the individual linear programs, which can occasionally result in undesired results like those in Figure 3.9 in Chapter 3. Therefore, a possible avenue of improvement could be implementing regularization methods for the optimization problem so that the estimation of each power function parameter is cognizant of those in adjacent range splits. Of course, this comes with added complexity and it is not clear if the simple linear programming approach could be extended to accommodate. Over-determination is not so much an issue with the method in Chapter 2 because of the lower number of parameters and the fact that there are constraints built directly into the objective function to ensure compatibility between subswaths (see (2.15)). However, applying the method in Chapter 2 leaves the non-linear mis-fit problem uncompensated.

## 4.2 Final remarks

The work in this thesis has presented two methods that can substantially improve the image quality of various types of Sentinel-1 images that are degraded by non-stationary noise floors. The methods are effective and their reliance on convex optimization techniques contributes to accessibility in terms of computation. While these methods were evaluated for image quality, the work in this thesis did not evaluate for any specific remote sensing tasks due to the incredibly wide scope of applications. The level of improvement provided by the algorithms is highly relevant for remote sensing applications using cross-polarized images over maritime regions. In particular, there could be great benefits from incorporating the algorithms into applications like ice analysis and wind speed analysis. As a result, I plan to make the software of the two methods available to the remote sensing community in the hopes that they will be useful for tasks that are hindered by the noise floor problem.

# References

- [1] Extra wide swath. Technical report, European Space Agency. Retrieved June 23, 2020. <https://sentinel.esa.int/web/sentinel/user-guides/sentinel-1-sar/acquisition-modes/extra-wide-swath>.
- [2] Interferometric wide swath. Technical report, European Space Agency. Retrieved June 23, 2020. <https://sentinel.esa.int/web/sentinel/user-guides/sentinel-1-sar/acquisition-modes/interferometric-wide-swath>.
- [3] SAR instrument description. Technical report, European Space Agency. Retrieved June 23, 2020. <https://earth.esa.int/web/sentinel/technical-guides/sentinel-1-sar/sar-instrument/description>.
- [4] A. Agrawal, R. Verschueren, S. Diamond, and S. Boyd. A rewriting system for convex optimization problems. *Journal of Control and Decision*, 5(1):42–60, 2018.
- [5] N. Agrawal and K. Venugopalan. Speckle reduction in remote sensing images. In *2011 International Conference on Emerging Trends in Networks and Computer Communications (ETNCC)*, pages 195–199, April 2011.
- [6] L. Alparone, B. Aiazzi, S. Baronti, and A. Garzelli. *Remote Sensing Image Fusion*. CRC Press, Inc., Boca Raton, FL, USA, 2015.
- [7] F. Argenti, A. Lapini, T. Bianchi, and L. Alparone. A tutorial on speckle reduction in synthetic aperture radar images. *IEEE Geoscience and Remote Sensing Magazine*, 1(3):6–35, 2013.
- [8] G. B. Bailey. *Land Surface Topography*, pages 320–325. Springer New York, New York, NY, 2014.
- [9] S. Boyd and L. Vandenberghe. *Convex Optimization*. Cambridge University Press, 2004.

- [10] Sentinel-1 Quality Control. Sentinel-1 QC — IPF versions, June 2020. Retrieved June 2, 2020. <https://qc.sentinel1.eo.esa.int/ipf/>.
- [11] C. L. V. Cooke and K. A. Scott. Estimating sea ice concentration from SAR: Training convolutional neural networks with passive microwave data. *IEEE Transactions on Geoscience and Remote Sensing*, 57(7):4735–4747, 2019.
- [12] CSC Mission Management Team. Sentinel high level operations plan. 2018. Retrieved June 23, 2020. [https://earth.esa.int/documents/247904/685154/Sentinel\\_High\\_Level\\_Operations\\_Plan](https://earth.esa.int/documents/247904/685154/Sentinel_High_Level_Operations_Plan).
- [13] S. Diamond and S. Boyd. CVXPY: A Python-embedded modeling language for convex optimization. *Journal of Machine Learning Research*, 17(83):1–5, 2016.
- [14] R. J. Duffin. Linearizing geometric programs. *SIAM Review*, 12(2):211–227, 1970.
- [15] C. Elachi, T. Bicknell, R. L. Jordan, and Chialin Wu. Spaceborne synthetic-aperture imaging radars: Applications, techniques, and technology. *Proceedings of the IEEE*, 70(10):1174–1209, October 1982.
- [16] P. Fieguth. *Statistical Image Processing and Multidimensional Modeling*, pages 13–51. Springer Science & Business Media, 2010.
- [17] L. Gagnon and A. Jouan. Speckle filtering of SAR images: A comparative study between complex-wavelet-based and standard filters. In *Wavelet Applications in Signal and Image Processing V*, volume 3169, pages 80–91. International Society for Optics and Photonics, 1997.
- [18] Y. Gao, C. Guan, J. Sun, and L. Xie. A wind speed retrieval model for Sentinel-1A EW mode cross-polarization images. *Remote Sensing*, 11(2):153, January 2019.
- [19] R. Gens. Oceanographic applications of SAR remote sensing. *GIScience & Remote Sensing*, 45(3):275–305, 2008.
- [20] R. Gens and J. L. Van Genderen. Review article SAR interferometry issues, techniques, applications. *International Journal of Remote Sensing*, 17(10):1803–1835, 1996.
- [21] R. C. Gonzalez and R. E. Woods. *Digital Image Processing*, pages 595–687. Pearson Education, Inc., 4th edition, 2017.

- [22] D.-B. Hong and C.-S. Yang. Automatic discrimination approach of sea ice in the Arctic Ocean using Sentinel-1 extra wide swath dual-polarized SAR data. *International Journal of Remote Sensing*, 39(13):4469–4483, 2018.
- [23] S. V. Hum. Antenna arrays, 2018. Retrieved June 23, 2020. <http://www.waves.utoronto.ca/prof/svhum/ece422/notes/15-arrays2.pdf>.
- [24] S. V. Hum. Radio and microwave wireless systems, 2018. Retrieved June 23, 2020. <http://www.waves.utoronto.ca/prof/svhum/ece422/notes/21-noise.pdf>.
- [25] Q. Huynh-Thu and M. Ghanbari. Scope of validity of PSNR in image/video quality assessment. *Electronics Letters*, 44(13):1–2, June 2008.
- [26] M. Iqbal, J. Chen, W. Yang, P. Wang, and B. Sun. Kalman filter for removal of scalloping and inter-scan banding in ScanSAR images. *Progress In Electromagnetics Research*, 132:443–461, 2012.
- [27] J. Karvonen. Baltic Sea ice concentration estimation using Sentinel-1 SAR and AMSR2 microwave radiometer data. *IEEE Transactions on Geoscience and Remote Sensing*, 55(5):2871–2883, May 2017.
- [28] E. S. Kasischke, J. M. Melack, and M. C. Dobson. The use of imaging radars for ecological applications a review. *Remote Sensing of Environment*, 59(2):141 – 156, 1997. Spaceborne Imaging Radar Mission.
- [29] R. Kwok. Satellite remote sensing of sea-ice thickness and kinematics: A review. 56(200):11291140, 2010.
- [30] P. Q. Lee, L. Xu, and D. A. Clausi. Sentinel-1 additive noise removal from cross-polarization extra-wide TOPSAR with dynamic least-squares. *Remote Sensing of Environment*, 248:111982, October 2020.
- [31] B. Li, B. Liu, W. Guo, Z. Zhang, and W. Yu. Ship size extraction for Sentinel-1 images based on dual-polarization fusion and nonlinear regression: Push error under one pixel. *IEEE Transactions on Geoscience and Remote Sensing*, 56(8):4887–4905, August 2018.
- [32] A. Maity, A. Pattanaik, S. Sagnika, and S. Pani. A comparative study on approaches to speckle noise reduction in images. In *2015 International Conference on Computational Intelligence and Networks*, pages 148–155, January 2015.

- [33] B. Marhaba and M. Zribi. Reduction of speckle noise in SAR images using hybrid combination of bootstrap filtering and DWT. In *2018 International Conference on Computer and Applications (ICCA)*, pages 377–382, August 2018.
- [34] M. Migliaccio and M. Tranfaglia. Oil spill observation by SAR: A review. In *2004 USA-Baltic International Symposium*, pages 1–6, 2004.
- [35] F. M. Monaldo, C. Jackson, and X. Li. On the use of Sentinel-1 cross-polarization imagery for wind speed retrieval. In *2017 IEEE International Geoscience and Remote Sensing Symposium (IGARSS)*, pages 392–395, 2017.
- [36] A. Moreira, P. Prats-Iraola, M. Younis, G. Krieger, I. Hajnsek, and K. P. Papathanassiou. A tutorial on synthetic aperture radar. *IEEE Geoscience and Remote Sensing Magazine*, 1(1):6–43, 2013.
- [37] B. O’Donoghue, E. Chu, N. Parikh, and S. Boyd. Conic optimization via operator splitting and homogeneous self-dual embedding. *Journal of Optimization Theory and Applications*, 169(3):1042–1068, June 2016.
- [38] B. O’Donoghue, E. Chu, N. Parikh, and S. Boyd. SCS: Splitting conic solver, version 2.1.2. <https://github.com/cvxgrp/scs>, November 2019.
- [39] J.-W. Park, A. A. Korosov, M. Babiker, S. Sandven, and J.-S. Won. Efficient thermal noise removal for Sentinel-1 TOPSAR cross-polarization channel. *IEEE Transactions on Geoscience and Remote Sensing*, 56(3):1555–1565, 2018.
- [40] S. Parrilli, M. Poderico, C. V. Angelino, and L. Verdoliva. A nonlocal SAR image denoising algorithm based on LLMMSE wavelet shrinkage. *IEEE Transactions on Geoscience and Remote Sensing*, 50(2):606–616, 2011.
- [41] R. Pelich, N. Longp, G. Mercier, G. Hajduch, and R. Garello. Performance evaluation of Sentinel-1 data in SAR ship detection. In *2015 IEEE International Geoscience and Remote Sensing Symposium (IGARSS)*, pages 2103–2106, July 2015.
- [42] A. Pepe and F. Calò. A review of interferometric synthetic aperture RADAR (InSAR) approaches for the retrieval of Earths surface displacements. *Applied Sciences*, 7(12):1264, 2017.
- [43] R. Piantanida. Sentinel-1 Level 1 detailed algorithm definition. Technical report, 2017. Retrieved April 1, 2019. Updated document at <https://sentinels.copernicus.eu/documents/247904/1877131/Sentinel-1-Level-1-Detailed-Algorithm-Definition>.



- [44] R. Piantanida. Thermal denoising of products generated by the S-1 IPF. Technical report, 2017. Retrieved April 1, 2019. <https://sentinel.esa.int/documents/247904/2142675/Thermal-Denoising-of-Products-Generated-by-Sentinel-1-IPF>.
- [45] R. Piantanida. Sentinel-1 Level 1 detailed algorithm definition. Technical report, 2019. Retrieved June 23, 2020. <https://sentinels.copernicus.eu/documents/247904/1877131/Sentinel-1-Level-1-Detailed-Algorithm-Definition>.
- [46] F. Qiu, J. Berglund, J. R. Jensen, P. Thakkar, and D. Ren. Speckle noise reduction in SAR imagery using a local adaptive median filter. *GIScience & Remote Sensing*, 41(3):244–266, 2004.
- [47] A. W. Santoso, D. Pebrianti, L. Bayuaji, and J. M. Zain. Performance of various speckle reduction filters on synthetic aperture radar image. In *2015 4th International Conference on Software Engineering and Computer Systems (ICSECS)*, pages 11–14. IEEE, 2015.
- [48] K. Schmidt, M. Schwerdt, N. Miranda, and J. Reimann. Radiometric comparison within the Sentinel-1 SAR constellation over a wide backscatter range. *Remote Sensing*, 12(5), March 2020.
- [49] C. C. Schmullius and D. L. Evans. Review article synthetic aperture radar (SAR) frequency and polarization requirements for applications in ecology, geology, hydrology, and oceanography: A tabular status quo after SIR-C/X-SAR. *International Journal of Remote Sensing*, 18(13):2713–2722, 1997.
- [50] W. Tan, J. Li, L. Xu, and M. A. Chapman. Semiautomated segmentation of Sentinel-1 SAR imagery for mapping sea ice in Labrador Coast. *IEEE Journal of Selected Topics in Applied Earth Observations and Remote Sensing*, 11(5):1419–1432, May 2018.
- [51] K. Topouzelis. Oil spill detection by SAR images: Dark formation detection, feature extraction and classification algorithms. *Sensors*, 8(10):6642–6659, 2008.
- [52] H. J. Visser. *Antenna Theory and Applications*, pages 189–227. John Wiley & Sons Ltd., 2012.
- [53] L. Wang, K. A. Scott, D. A. Clausi, and Y. Xu. Ice concentration estimation in the Gulf of St. Lawrence using fully convolutional neural network. In *2017 IEEE International Geoscience and Remote Sensing Symposium (IGARSS)*, pages 4991–4994, 2017.

- [54] Z. Wang, A. C. Bovik, H. R. Sheikh, E. P. Simoncelli, et al. Image Quality Assessment: From Error Visibility to Structural Similarity. *IEEE Transactions on Image Processing*, 13(4):600–612, 2004.
- [55] J. Wei and H. Chen. Effect of roll angle error on spaceborne ScanSAR radiometric calibration in range. In *2007 International Symposium on Microwave, Antenna, Propagation and EMC Technologies for Wireless Communications*, pages 1471–1475. IEEE, August 2007.
- [56] L. Xu and J. Li. *Mapping Sea Ice from Satellite SAR Imagery*, pages 113–135. Springer Netherlands, Dordrecht, 2015.
- [57] L. Xu, M. J. Shafiee, A. Wong, and D. A. Clausi. Fully connected continuous conditional random field with stochastic cliques for dark-spot detection in SAR imagery. *IEEE Journal of Selected Topics in Applied Earth Observations and Remote Sensing*, 9(7):2882–2890, July 2016.
- [58] Q. Yu and D. A. Clausi. IRGS: Image segmentation using edge penalties and region growing. *IEEE Trans. Pattern Anal. Mach. Intell.*, 30(12):2126–2139, December 2008.
- [59] F. D. Zan and A. M. Guarnieri. TOPSAR: Terrain observation by progressive scans. *IEEE Transactions on Geoscience and Remote Sensing*, 44(9):2352–2360, September 2006.
- [60] D. Zwillinger. *CRC Standard Mathematical Tables and Formulae*. Chapman & Hall/CRF, 31 edition, 2003.

# Glossary

**backscatter** The radiation that is scattered off a ground target and measured by an observing antenna.

**co-polarization** Imaging mode where the polarity of the emitted radiation is the same to the polarity of the measurement.

**cross-polarization** Imaging mode where the polarity of the emitted radiation is perpendicular to the polarity of the measurement.

**EW** Extra Wide mode. A Sentinel-1 sensor mode that is designed to cover large surface areas and is typically applied to maritime regions.

**IPF** Instrument Processing Facility. The software used in the Sentinel-1 processing pipeline.

**IW** Interferometric Wide mode. A Sentinel-1 sensor mode with finer resolution but lower surface area coverage than EW mode.

**noise floor** The lower bound of signal added to a system that is the lower bound of the sum of noise sources.

**subswath** Divisions along the range that compose the image. Images acquired via the TOPSAR scanning pattern, such as EW and IW modes, divide the range into different subswaths.